Design of an Optimized Interfacing for Vanadium Redox Flow Battery (VRFB) Storage with Renewable Energy Systems (RES) and its Performance Analysis

THESIS

Submitted in partial fulfillment
of the requirements for the degree of

DOCTOR OF PHILOSOPHY

by

NAWIN RA

ID No.: 2019PHXF0430H

Under the Supervision of

Dr. Ankur Bhattacharjee

BITS Pilani
Pilani | Dubai | Goa | Hyderabad

BIRLA INSTITUTE OF TECHNOLOGY AND SCIENCE, PILANI

2023

BIRLA INSTITUTE OF TECHNOLOGY AND SCIENCE, PILANI

CERTIFICATE

This is to certify that the thesis entitled "**Design of an Optimized Interfacing for Vanadium Redox Flow Battery (VRFB) Storage with Renewable Energy Systems (RES) and its Performance Analysis"** and submitted by **Nawin Ra**, ID. No. **2019PHXF0430H** for award of **Ph.D.** of the Institute embodies original work done by him under my supervision.

Ankur Bhattacharjee

Signature of the Supervisor

Name of the Supervisor - Dr. ANKUR BHATTACHARJEE

Designation - Assistant Professor

Department of Electrical and Electronics Engineering

Birla Institute of Technology and Science-Pilani

Date: 28-Aug-2023

DECLARATION

This is to certify that the thesis titled "Design of an Optimized Interfacing for Vanadium Redox Flow Battery (VRFB) Storage with Renewable Energy Systems (RES) and its Performance Analysis" is based on my own research work and has been carried out under the guidance and supervision of Dr. Ankur Bhattacharjee, Assistant Professor, Department of Electrical and Electronics Engineering, BITS Pilani, Hyderabad Campus, Hyderabad, India.

The data and information which I have used from various sources have been duly acknowledged. I declare that this work has not been previously submitted by me to any other university / Institute for the award of any other degree or diploma.

Date: 28-Aug-2023 Name: Nawin Ra

Place: Hyderabad ID No: 2019PHXF0430H

Acknowledgments

First and foremost, I am deeply grateful to my esteemed supervisor, Dr. Ankur Bhattacharjee, for his guidance, which enlightened me on the path to my research journey. For this, I am incredibly grateful. His invaluable supervision, immense knowledge, plentiful experience, and tutelage have encouraged me throughout my academic research and daily life. I would especially like to thank him for being more patient and bestowing real encouragement through the ups and downs that inspired me to work more enthusiastically and accomplish productive outcomes. I want to thank our research collaborators Prof. Hiranmay Saha, Dr. Aritra Ghosh, and Mr. Arjun Dutta for their motivation and the informative suggestions that inspired me to extend my research from a range of perspectives.

I am genuinely grateful to my doctoral advisory committee (DAC) members Prof. Alivelu Manga Parimi, former Head of Department (HOD), Department of Electrical and Electronics Engineering, Birla Institute of Technology and Science Pilani, Hyderabad Campus, and Dr. Sudha Radhika, for their invaluable suggestions, encouraging exposition, and insightful remarks during different stages of this research work. I am deeply grateful to the members of the Doctoral Research Committee (DRC) for their unwavering moral support throughout the duration of my Ph.D. work.

I sincerely thank Prof. Subhendu Kumar Sahoo, HOD, Department of Electrical and Electronics Engineering, Birla Institute of Technology and Science Pilani, Hyderabad Campus, for allowing me to conduct my research work and equipping the facilities in the department. I thank Prof. G. Sundar, Director, Birla Institute of Technology and Science Pilani, Hyderabad Campus, for his constant support and guidance during the work. I am grateful to Prof. V. Ramgopal Rao, the present Vice Chancellor, Birla Institute of Technology and Science, Pilani, and Prof. Souvik Bhattacharyya, the former Vice Chancellor, Birla Institute of Technology and Science, Pilani, for their insightful thoughts in encouraging the entire BITS fraternity. I am grateful to Academic-Graduate Studies and Research Division (AGSRD) for their unwavering support during this doctoral study.

My sincere thanks to all faculty members, technicians, and non-teaching staff of the Department of Electrical and Electronics Engineering, Birla Institute of Technology and Science-Pilani, Hyderabad Campus, for their kind help in assistance during my Ph.D. proposal seminar, Ph.D. seminar, and symposium. Numerous recommendations and motivations made

by them for my Ph.D. work and teaching duties on assessment components prompted me to better myself.

When my journey continued to expand into a Ph.D. community, I learned several things from various individuals in different fields from different departments and strengthened myself. I want to express my appreciation to all my research scholar colleagues for their general fruitful discussions on various emerging research topics, software and application tools, future possibilities, and much more.

My deepest and heartfelt gratitude to my parents Mr. Ramasubbu and Mrs. Sujatha, relatives, friends, and well-wishers for being my pillars of strength for their absolute moral comfort and generous support.

Thank you all for the support and encouragement.

Abstract

Flow batteries are becoming increasingly popular because of the numerous advantages they offer. These systems are modular, highly efficient, and relatively low cost, making it easy to scale up. In terms of reaction mechanism, flow batteries are identical to conventional batteries. However, in flow batteries, the electrolytes are held separately in external tanks and then pumped using hydraulic pumps to flow through the stack during operation. Among the several available flow batteries, the technologically advanced and widely commercialized flow battery is Vanadium Redox Flow Battery (VRFB). VRFB storage, however, is less commercially widespread than conventional batteries such as lithium-ion or lead-acid batteries. The primary reasons include a lack of battery-specific optimization techniques and an efficient electrical interface with renewable energy sources. Therefore, this thesis focuses on the optimized electrical interface of VRFB with renewable energy sources. The significant contributions of this thesis are as follows.

In this work, a dynamic model of VRFB is developed and validated experimentally to design an efficient electrical interface for VRFB storage with renewable energy sources. The electrical characteristics of VRFB are investigated through modeling under the impact of practical parameters like flow rate, charge-discharge current, self-discharge loss, temperature etc. A comprehensive capacity fade model of the VRFB storage has been proposed to estimate the aging of VRFB storage. The experimental validation of the model performance has been carried out by a practical 1kW 6kWh VRFB system.

Prediction of battery storage system loss is necessary to improve the battery storage system's performance, reliability, and efficiency. In this work, the prediction of the overall system power loss of VRFB using different machine learning (ML) algorithms has been demonstrated for the first time. Under different operating current levels and electrolyte flow rates, the internal resistance variation and pump power consumption of the practical 1kW 6kWh VRFB system dataset have been considered for prediction. It is observed that the Ensemble learning (EL) based Adaptive Boost (AdaBoost) algorithm is superior in predicting VRFB system loss compared to that of linear regression (LR) and support vector regression (SVR) algorithms. The prediction results obtained in this work claim to be beneficial for designing optimized interfacing of VRFB storage with renewable energy sources and other power system applications.

Battery storage performance optimization is crucial in ensuring the reliable operation of renewable energy-integrated power systems and emergency backup applications. In this work, a kW scale VRFB storage system power loss optimization based on the particle swarm optimization (PSO) technique has been demonstrated for the first time. It is a multi-variable optimization considering both the VRFB pump power loss and stack power loss simultaneously. The electrolyte flow rate has been considered the control variable in optimizing the overall VRFB system power loss. Charge-discharge operations of VRFB with four sets of electrolyte flow rates at three different levels of stack terminal current have been taken to validate the proposed work.

In the countries like India, where the ambient temperature is higher during the significant span of the year, safe and efficient operation is needed for the delicate electronic panels and controllers installed in Electric Vehicle (EV) charging stations. Therefore, in this work, for the first time, solar-battery storage integrated switchable glazing topology has been applied to provide daytime passive heating ventilation and air conditioning (HVAC) in EV charging station control rooms. The EV charging station has been accompanied by a solar PV source installed on its roof-top to promote green energy and sustainable transportation. VRFB has been integrated with the system to ensure energy security as a long-life energy storage solution. An Internet of Things (IoT) based smart scheduling of solar PV, VRFB storage and the local distribution grid has been demonstrated to satisfy the building glazing load demand under real-time dynamic environmental conditions. The performance of the proposed system has been validated under four different transient scenarios; sunny, intermittent cloudy, prolonged cloudy and low solar irradiance with frequent grid outages. The proposed solution is a generalized one and thus can be very useful for scaled-up capacity.

TABLE OF CONTENTS

List of Tables

List of Figures

List of Abbreviations and Symbols

Abbreviations

AC	Alternating Current
AdaBoost	Adaptive Boost
AI/ML	Artificial Intelligence/Machine Learning
ANN	Artificial Neural Network
BESS	Battery Energy Storage System
BMS	Battery Management System
CAES	Compressed Air Energy System
CC-CV	Constant Current - Constant Voltage
CV	Cross-Validation
DC	Direct Current
EC	Electro-Chromic
ECS	Electro-Chemical Energy Storage
EL	Ensemble Learning
EV	Electric Vehicle
FC	Fuel Cells
FES	Flywheel Energy System
GA	Genetic Algorithm
GHG	Green House Gas
GSM	Grid Search Method
HVAC	Heating Ventilation and Air Conditioning

EVCS	Electric Vehicle Charging Station
IoT	Internet of Things
ISC	Internal Short Circuit
Li-ion	Lithium Ion
LR	Linear Regression
MAE	Mean Absolute Error
MC	Monte Carlo
MPPT	Maximum Power Point Tracking
MQTT	Message Queuing Telemetry Transport
Na S	Sodium Sulphur
Ni-Cd	Nickel Cadmium
PCU	Power Conditioning Unit
PEM	Proton Exchange Membrane
PHS	Pumped Hydro System
PSO	Particle Swarm Optimization
PV	Photo-Voltaic
RES	Renewable Energy Sources
RMSE	Root Mean Square Error
SC	Super Capacitors
SCADA	Supervisory Control and Data Acquisition
SMES	Superconducting Magnetic Energy Storage
SPD	Suspended Particle Device

SVR	Support Vector Regression
TES	Thermal Energy Storage
THD	Total Harmonic Distortion
UNSDG 7	United Nations Sustainable Development Goal 7
UNSW	University of New South Wales
VRFB	Vanadium Redox Flow Battery

Symbols

Symbol	Parameter	Unit
A_{pv}	Effective surface area of solar PV module	m^2
C	Capacity of VRFB storage	Ah
C_{dl}^{a}	Anolyte Double-layer capacitance	F
d	Membrane thickness	m
E_{OCV}	Open circuit voltage of the VRFB stack	V
F	Faraday's constant	96485 C/mol
I_d	Diffusion current	A
I_{pv}	Incident effective irradiance	W/m^2
I_p	Parasitic current	A
I_{ch}	Charging current	A
I_s	Stack current	A
I_{sh}	Shunt current	A
$I_{trickle}$	Trickle current	A

η_{pv}	Efficiency of solar PV module	%
P_{loss_VRFB}	Overall VRFB system power loss	W
P_{pump}	Pump power loss	W
P_{stack_loss}	VRFB stack power loss	W
P_{pv}	DC power output from a solar PV system	W
ρ	Electrolyte density	kg/m^3
Q	Electrolyte flow rate	L/min
Q_{opt}	Optimal electrolyte flow rate	L/min
q	Capacity fade	P.U.
R	Universal gas constant	8.314 J/(mol*K)
R_{int}	VRFB stack internal resistance	Ω
R_{ct}^{a}	Anolyte charge transfer resistance	Ω
R_m	Membrane resistance	Ω
R_o	Solution resistance	Ω
R_s	Series resistance element	Ω
R_{SD}	Self-discharge resistance	Ω
S	Membrane area	m^2
T	Ambient temperature	K
V_s	Stack volume	m^3

Chapter 1

Introduction

1.1 Need for Energy Storage

In the modern era, the electrical grid infrastructure is upgrading rapidly with sophisticated technological advancements in the electrical power sector. There is a promising surge in the penetration of renewable energy into the global energy scenario. Renewable energy is gaining significant attraction nowadays due to the scarcity of fossil fuel supplies and their environmental consequences. Solar energy and Wind energy are the most popular renewable energy sources (RES) due to their ease of generation and abundant availability. However, RES is intermittent; other conventional utility power plants are needed to support their widespread implementation. As a result, as penetration of RES increases, ensuring the stability of the overall system operation becomes more challenging. To achieve the full potential of renewable energy integration, a sophisticated large-scale energy storage system with long-life operation is the need of the hour [1].

Currently, the technologies that are used for large-scale energy storage include physical energy storage through the pumped hydro system (PHS), compressed air energy system (CAES) and flywheel energy system (FES), electromagnetic energy storage through superconducting magnetic energy storage (SMES) and supercapacitors (SC), chemical energy storage through fuel cells (FC) and battery energy storage system (BESS), and thermal energy storage (TES) by heating or melting materials. Considering the peak power shaving, demand response management and wide range of energy capacity, BESS exhibit faster response compared to the other conventional large-scale energy storage technologies such as; PHS, CAES, etc. [2]**. Figure 1.1** displays the statistics of large-scale energy storage distribution [2]. **Figure 1.1 (a)** gives the share of large-scale energy storage technologies by 2020. As of 2020, the cumulative installed capacity of energy storage projects worldwide reached 191.1 GW, of which the cumulative installed capacity of pumped storage was the largest, accounting for 90.3% [2]. Meanwhile, the installed capacity of electro-chemical energy storage (ECS) followed next, accounting for 7.5%, as shown in **Figure 1.1 (a)**. Although the scale of PHS is huge, it is restricted by the geographical environment and has grown slowly over the years 2016-2020, as shown in **Figure 1.1 (b)**.

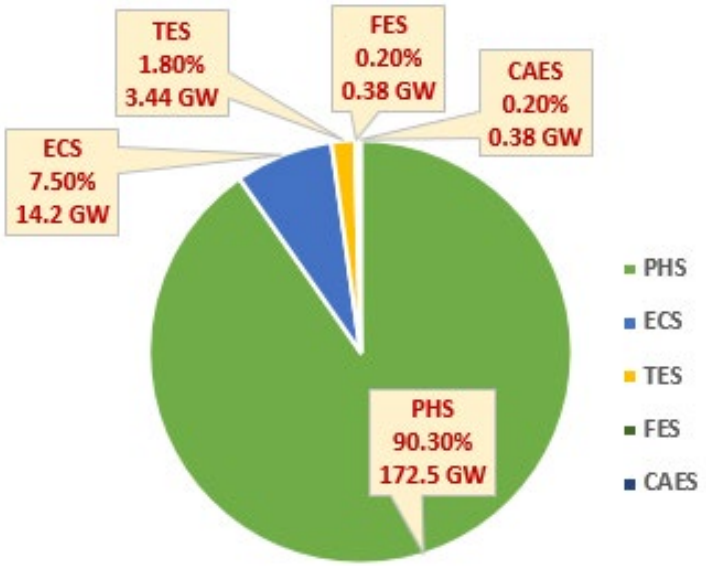
TES
1.80%
3.44 GW
FES
0.20%
0.38 GW
CAES
0.20%
0.38 GW
ECS
7.50%
14.2 GW
PHS
90.30%
172.5 GW
PHS
ECS
TES
FES
CAES

(a)

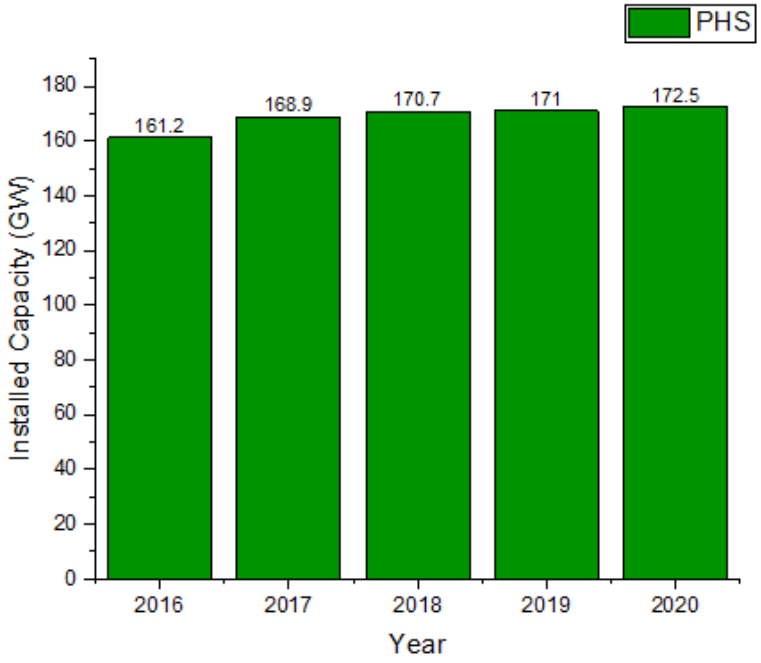
PHS
Installed Capacity (GW)
0
20
40
60
80
100
120
140
160
180
161.2
168.9
170.7
171
172.5
2016
2017
2018
2019
2020
Year

(b)

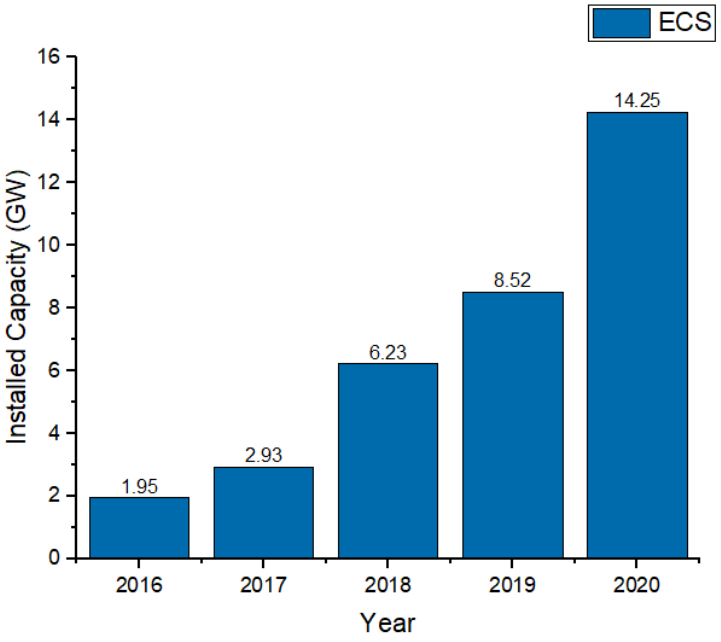

(c)

Figure 1.1: **Statistics of large-scale energy storage distribution: (a) Global share of installed large scale energy storage systems by the year 2020, (b) Installed capacity of PHS from 2016 to 2020, (c) Installed capacity of ECS from 2016 to 2020** [2]

Similarly, the scale of CAES is also large, while it is affected by the geographical environment and geological conditions, and the equipment needs strong pressure-bearing capacity. Currently, ECS has become the energy storage technology with the most significant development potential. Specifically, the cumulative installed capacity of ECS reached 14.2 GW in 2020, with a surge of 49.6% over the year 2019, as shown in **Figure 1.1 (c)**. The key conclusion can be inferred that ECS is becoming more and more critical. The widely used ECS comprises of batteries, which is one of the reasons for the surge in the research & development of various battery storage technologies [3].

1.1.1 Batteries as Energy Storage

Before Nikola Tesla demonstrated the AC power system, batteries were used to store electrical energy. Since that time, several battery technologies have been developed, and new, effective techniques to combine DC and AC power have been consistently proposed over time. Energy storage is more critical than ever due to the rising popularity of renewable energy sources, electric vehicles, and the necessity of energy independence for consumers from lengthy blackouts.

Batteries are electrochemical devices that convert the energy released during a chemical reaction into electrical energy. There are two distinct common types of batteries, designated

primary and secondary batteries. A primary battery can only be used once. This battery is commonly used in small portable devices but is of little use for large-scale applications. A secondary battery, in contrast, is reusable. Multiple charge/discharge cycles are supported using secondary batteries. When compared to primary batteries, secondary batteries offer shallow self-discharge loss, quick reaction times, and good round-trip efficiency [3]. Lead-Acid, Lithium Ion (Li-ion), Sodium Sulphur (NaS), Nickel Cadmium (Ni-Cd) and Redox Flow Batteries (RFBs) are all different types of secondary batteries. **Table 1.1** shows the comparison among the different battery storage.

Table 1.1: Comparison among different battery storage

Battery	Energy Density (Wh/kg)	Energy efficiency (%)	Power Density (W/kg)	Cycle life (cycles)	Self-Discharge (% /month)
Lead-Acid [4]	30-40	70-90	180	200-2000	3-4
Li-ion [5]	100-250	75-90	1800	500-2000	5-10
NaS	150	80-90	120-150	2500	<1
Ni-Cd	40-60	60-90	140-180	500-2000	10-15
Redox Flow Battery [6]	30-50	80-90	120-180	>20000	<1

For most applications, battery energy storage systems (BESS) are also more practical and compact due to their modularity and high power and energy densities. Nevertheless, there are still specific difficulties in connecting energy storage devices with the electrical grid. To begin with, there is no general standardization of the types of batteries integrated into the grid, which causes a slew of minor reliability concerns that disrupt the power flow [7]. Second, the batteries are poorly optimized for the entire grid since they function as isolated nodes that meet local demand. However, these challenges can be handled using smart grid technology, where each component is designed for maximum grid efficiency [8]. Some of the most prominent battery technologies for large-scale energy storage are listed below:

- Lead-acid batteries are among the oldest and most well-established rechargeable batteries. It comprises a lead anode sponge and a lead acid cathode, with sulphuric acid solution serving as the electrolyte. It offers various benefits, including a simple production method at a cheap cost and an appropriate cycle life. The battery, on the other hand, is made of heavy metal, and the cost per unit climbs in direct proportion to the scale [9].

- Due to high energy density, superior cycle efficiency, and minimal self-discharge, lithium-ion batteries are the most well-known and widely used [10]. They are primarily composed of phosphate or cobalt. Some of the disadvantages are limited lithium resources, high cost, and concerns with safety, requiring a sophisticated battery management system (BMS) [11].
- The most successful high-temperature battery is the sodium-sulphur battery. It is highly efficient, has a high energy density, a long cycle life, and a cheap material cost [12]. The necessity to maintain a high temperature, operator safety, and the need to isolate the system from the atmosphere as pure sodium causes an instant explosion on contact with air, are some of the constraints that are preventing this battery from being widely used [13].
- Ni-Cd batteries are used when long life, high discharge rate, and low price are the requirement for the desired application. The drawback of Ni-Cd batteries is the memory effect issue and the negative environmental impact caused by toxic cadmium [14].
- In terms of reaction mechanism, flow batteries are identical to conventional batteries. However, in flow batteries, the electrolytes are held separately in external tanks and then pumped using hydraulic pumps to flow through the stack during operation. Several types of flow battery chemistry are being researched. Among the prominent prospects are all vanadium, iron-chromium, zinc-bromine, zinc-ceria, and bromine-polysulphide. Flow batteries have various benefits, including individual scaling of power and energy capacity, minimal maintenance costs, the potential to be deployed on a mass scale, and low self-discharge [15]–[17]. Among the several available flow batteries, the technologically advanced and widely commercialized flow battery is Vanadium Redox Flow Battery (VRFB). **Figure 1.2** displays the timeline of the development of various aqueous redox flow batteries over the years [18], [19].

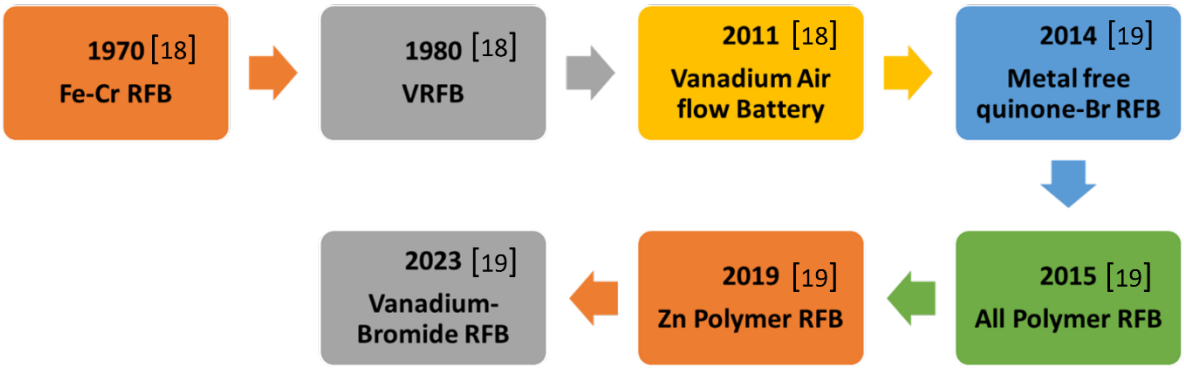

Figure 1.2: Timeline of the developments in Aqueous Redox Flow Batteries (RFBs)

Some drawbacks of RFBs include system complexity, the need for pumps, and low energy density. Technology is still evolving with improved methodologies in tackling the disadvantages, making flow batteries one of the most promising technologies for large-scale energy storage.

1.2 VRFB storage

RFBs such as Iron-Chromium RFB, metal-free quinone-bromine RFB, zinc polymer RFB, and Zinc-Bromine RFB utilize two different redox couples in each half-cell, and they suffer from electrolyte cross-contamination [20]. To overcome the cross-contamination, Professor Maria Skyllas-Kazacos and her research group from the University of New South Wales (UNSW) invented the all-vanadium redox flow battery, which utilized the same vanadium element in both half-cells. The UNSW research group filed the patent for all vanadium RFB in 1986. The significant advantage of vanadium is that it exists in four oxidation states (V^{2+}, $V^{3+,}$ $V^{4+,}$ and V^{5+}).

1.2.1 Working principle of VRFB

The components constituting VRFBs are electrodes, usually made with carbon felts, electrolytes, and bipolar plates, which avoid collision among current collectors. **Figure 1.3** shows the schematic diagram of VRFB. Two external tanks containing Vanadium ions of different oxidation states such as V^{2+}, V^{3+}, V^{4+} and V^{5+}. The tank containing anodic redox-active vanadium ions V^{2+} or V^{3+}(or anolyte) is known as negative electrolyte tank and the tank with cathodic redox-active vanadium ions V^{4+} or V^{5+} (or catholyte) are known as positive electrolyte tank as shown in **Figure 1.3 (c)**. The presence of V^{2+} or V^{3+} in the negative electrolyte tank depends on the charging or discharging process. The capacity of the VRFB is directly proportional to the volume of the electrolyte tank. VRFB employs two redox couples dissolved in the half-cell electrolytes (anolyte and catholyte) which are stored in separate external tanks and are continuously pumped into the battery stack where the electron transfer reactions occur at the inert electrodes. This is the primary difference between the other conventional batteries and redox flow batteries which gives longer cycle life because the active material in the case of RFBs is the electrolyte, not the electrode. Where, $V^{4+}$and V^{5+} are in fact vanadium oxide ions (respectively $VO^{2+}$and VO_2^+). The total power output depends on the size of the active area inside the stack. In addition, there are unique advantages offered by VRFB, as mentioned in the following subsection of this chapter.

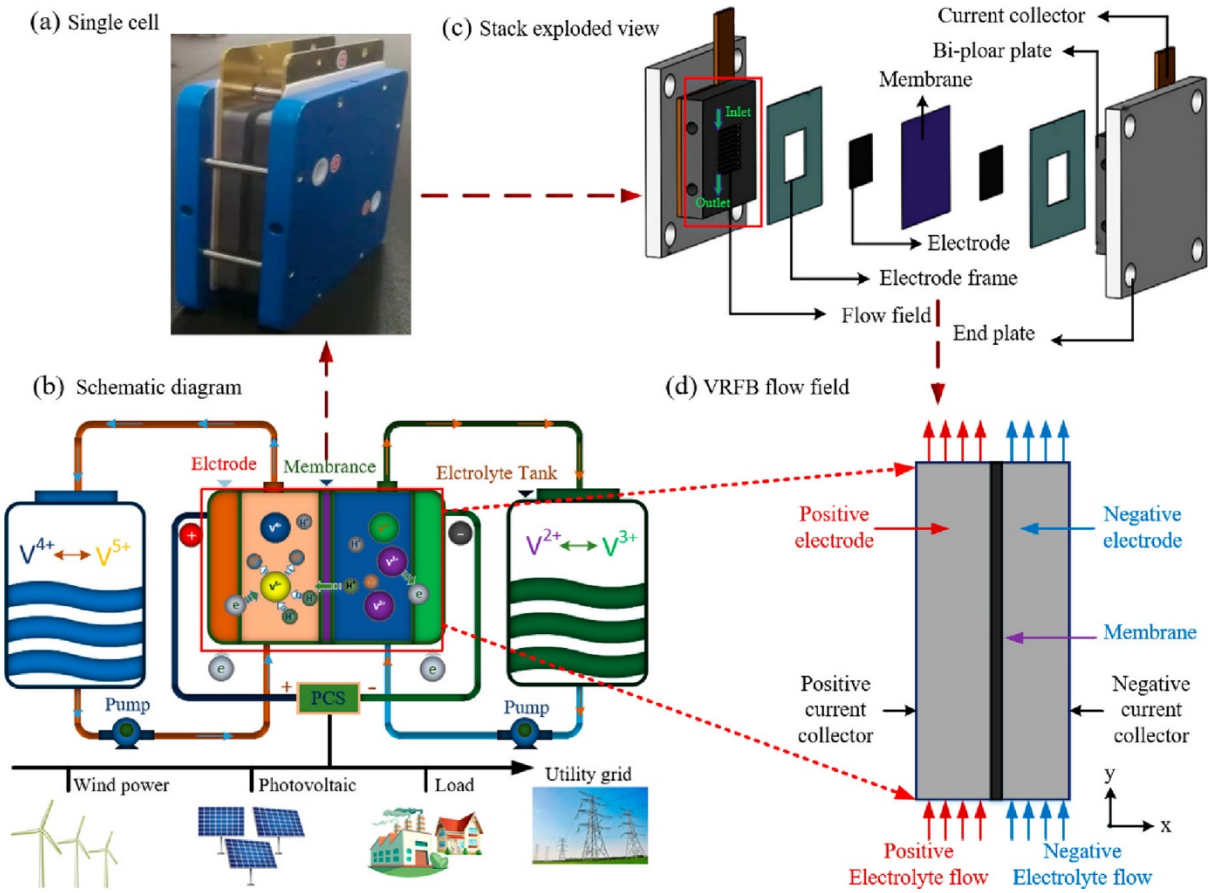

Figure 1.3: **Schematic diagram of vanadium redox flow battery: (a) single cell, (b) schematic diagram of a single cell, (c) stack exploded view, and (d) vanadium redox flow battery flow field** [2]

1.2.2 Unique features of VRFB

- **Relatively long cycle life**: Flow batteries have an exceptionally long-life cycle since the active material is a non-degradable electrolyte. Unlike conventional batteries, whose active material electrodes degrade due to mechanical and thermal stress with cycling, flow batteries offer the independent replacement of components such as electrodes. In addition, the VRFB has the unique feature of having the most extended cycle life (>20,000 cycles) of more than 20 years, which is close to the life of a solar PV plant [21].
- **Independent scalability of Energy and Power Ratings**: Due to their interdependence, conventional batteries must make a trade-off between their energy and power ratings. Whereas in a flow battery, the energy rating is determined by the size of the electrolyte tank, and the power rating is determined by the quantity of cell stacks. This is a crucial feature since it allows for independent scalability based on the requirement of the end user.

For the past three decades, researchers all over the world have emphasized their research & developmental work on all Vanadium-RFBs in comparison with other RFB technology, only because of the above-mentioned advantages, focusing on the improvement of the electrode

material, cost-effective membrane materials, electrolyte preparation, and the energy efficiency. The shortcomings of VRFB include a low, relatively poor energy-to-volume ratio compared to standard storage batteries. The aqueous electrolyte makes the battery heavy and only valid for stationary applications. Vanadium is relatively abundant, and the electrolyte solution is relatively easy to prepare. Unlike other secondary rechargeable systems, such as lead-acid and lithium-ion batteries, VRFBs have minimal environmental impact; the redox couple reactions do not generate any toxic gases, and the batteries have a low risk of explosion [22]. Even though vanadium is environmentally friendly, the balance of plant components, such as the Nafion membrane, has environmental impacts [23].

The successful field trial of VRFB was demonstrated by UNSW, through installation in a solar house in Thailand [24]–[29]. Thai Gypsum Products Ltd. of Thailand acquired the license to VRFB technology in 1993 for solar house applications. Japan-based Mitsubishi Chemicals and SEI acquired the license for VRFB technology. Japanese farms utilized VRFB storage for several applications such as Wind Energy Storage, load leveling, and power backup. After the expiry of basic UNSW patent for all-VRFB in 2006, R&D in VRFB took a giant leap [21]. **Table 1.2** lists the commercial applications of VRFB around the world during the last five years. Researchers from various parts of the world worked on sensors, design of the stack, and control systems of the VRFB.

Table 1.2: Commercial applications of VRFB around the world during the last 5 years (2017-2022)

Year	Location	Application	Power / Energy Capacity
2022 [19]	Canada	Energy Storage	10 MW / 40 MWh
2021 [19]	Australia	Grid-scale Energy Storage	20 MW / 80 MWh
2021 [30]	Germany	Microgrid Energy Storage	1.2 MW / 7.2 MWh
2021 [30]	China	Peak Shaving	10 MW / 30 MWh
2020 [31]	Japan	Renewable Energy Integration	2 MW / 8 MWh
2020 [31]	USA	Commercial & Industrial Energy Storage	1 MW / 4 MWh
2019 [31]	South Africa	Solar Energy Storage	1 MW / 4 MWh
2018 [30]	China	Microgrid Energy Storage	3 MW / 12 MWh
2018 [30]	UK	Renewable Energy Integration	1 MW / 4 MWh
2017 [30]	Japan	Solar Energy Storage	1 MW / 4 MWh

Over the years, researchers have realized the improvement of system efficiency by optimization of flow rate. Modeling and simulation of the VRFB system, with the help of commercial software, has enhanced the dynamics in the overall development of VRFB. Simulation helps in the better exploration of the system performances under various testing

conditions. The VRFB performance analysis and optimization can be done through accurate modeling and simulation studies. The equivalent models are further helpful in designing the optimized interface of VRFB storage with external power systems. Considering the need for the modeling of the VRFB energy storage, in this chapter, various relevant research reports have been discussed and analyzed in detail. The issues related to the interfacing of VRFB with renewable energy sources like solar PV and wind energy sources are discussed in this chapter. ESS, like VRFB, plays a crucial role in microgrid because it can provide them with several service capabilities, ranging from power quality to peak shaving and energy management. Integration of renewable energy sources like solar PV and wind energy into existing power grids faces technical and economic challenges due to their variable and intermittent nature.

1.2.3 Modeling of VRFB

The issues prevailing with the current trends in VRFB technology can be summarized using the top-down approach in four levels, namely market level, system level, cell level and material level [32]. The commercialization of VRFB is influenced by factors such as the battery system's manufacturing cost, battery cycle life, and the system's safety features that must consider the life of the personnel working on it. These issues sometimes affect the commercial acceptance of VRFB because of the shortfall in the control or monitoring at the VRFB system level. The system-level issues are related to the failure in the dynamic flow rate control, estimating the capacity loss, poor design of the stack, losses due to shunt current, etc. Further investigation on the VRFB operation at the cell level will result in factors associated with the VRFB system's failure. The cell-level modeling includes physicochemical processes inside a battery, such as momentum transport, mass transport, heat transfer, species crossover, etc. To improve the commercialization of VRFB, robust modeling of VRFB at the cell and material level is required. For up-gradation in battery research, the modeling at the material and cell level played a significant role. **Table 1.3** gives an overview of the factors influencing the modeling of VRFB at different levels [32].

Table 1.3: Factors influencing the modeling of VRFB at different levels

No.	Level name	Components	Prevailing issues for VRFB technology
Level 1	Market level [33], [34]	Integration of VRFB with renewable energy sources, also as a stationary storage backup in power sectors	➢ Economy of VRFB technology ➢ Safety features ➢ Cycle life

Level 2	System level [35], [36]	VRFB stack along with components such as pump, control circuit, etc.	➢ Monitoring of the stack operation ➢ Failure in the dynamic flow rate control ➢ Poor stack design ➢ Control strategies adopted for VRFB such as management system
Level 3	Cell level [37]–[39]	VRFB cell including electrodes, membrane and electrolyte	➢ Momentum transport ➢ Mass transport ➢ Heat transport ➢ Charge transport ➢ Species crossover ➢ Self-discharge ➢ Side reactions
Level 4	Material level [40], [41]	Materials utilized for VRFB cell	➢ Chemical Stability ➢ Reaction pathways ➢ Activation energy

Optimizing the VRFB operating conditions is possible by modifying and improving the performance of materials used for the VRFB cell. The electrode performance can be improved by considering parameters such as current density, over-potential, and electrolyte concentration [42]–[45]. The low energy density offered by vanadium is a factor to be considered for improvisation in VRFB modeling. In the modeling of lithium-ion batteries, researchers integrated two or more modeling approaches to assess the system in a better way [46]. The higher energy density of the Lithium-ion battery played a vital role in its rapid commercialization. Similarly, in VRFB, enhancing the electrolyte solubility and improving the chemical stability of the materials used for electrolytes will help raise the energy density of the VRFB cells. In this chapter, we have focused on the system-level modeling of VRFB in detail. The commercial market for VRFB technology in large-scale energy storage systems is growing consistently. The primary consideration for marketing VRFB storage includes safety features offered by the battery operating condition and the total cost of the system. The cost of the VRFB system plays a vital role in the marketability of the system. System-level modeling is a holistic approach, including the cell and material level modeling discussed in **Table 1.3**. Modeling of the VRFB system can be carried forward by various approaches existing in the literature. The modeling approach suitable for the VRFB can be evaluated by parameters such as the utility of past experimental data, prediction of uncertain parameters, adapting physicochemical principles, and assumption of boundary conditions. **Table 1.4** analyses the features available in the different approaches utilized in VRFB modeling.

The feasibility of VRFB technology is evaluated through cost analysis. Cost analysis is carried out using an empirical model. A cost function is formulated based on power density and energy density. Various factors, including the costs of electrolyte, membrane, and electrode, influence the total cost of the VRFB system. To measure the influence of these components individually, a term known as the relative sensitivity index is proposed. The component with the higher relative sensitivity index value profoundly influences the overall cost of the system. As per the analysis, the high costs of electrolyte and membrane contributed heavily to the system's overall cost.

Table 1.4: Features of models of VRFB utilized in macro approach

Macro approach	**Empirical model**	**Monte-Carlo model**	**Multi-physics model**	**Equivalent circuit model**
Methodology	Approach involving polynomials, exponential, trigonometric functions, etc. [47]	Statistical approach [48]	Mass and energy conservation principles are utilized in building the models [49]	Models are built using electrical components [50]
Utility of past experimental data	Yes	No	No	Yes
Adaptation of Physicochemical principles	No	No	Yes	Yes [51]
Prediction of uncertain parameters	Yes	Yes [52]	No	Yes
Time dependency	No	No	Yes	Yes
Assumptions of boundaries	Yes	No	Yes	Yes [51]

Integrating empirical model and electrochemical model, researchers developed the cost-performance model. The empirical model gave the details for the economic aspects of the VRFB system. The electrochemical model evaluated the performance of the VRFB system. The combined results were explained through a function in the form of (E/P) ratio, where E represents the VRFB system's energy, referred to electrolyte; ‘P’ represents the power of the

VRFB system, referred to electrode. To analyze which component costs the majority of the overall cost of the VRFB system, the E/P ratio is helpful. For example, a high (E/P) ratio means the electrolyte costs dominate the system's overall cost. For the scale-up of large-scale energy storage systems, these modeling results will be helpful for consumers to estimate the system's budget beforehand accurately. As seen in the **Table 1.4**, Monte Carlo (MC) method [52]–[56] was not suitable for VRFB system modeling as the physicochemical process could not be formulated in that modeling approach. VRFB models developed using other modeling approaches, such as the equivalent circuit and lumped parameter approaches, were experimentally validated. The electrical equivalent circuit modeling approach was robust; it accurately evaluated several electrical parameters of the VRFB system. Some publications on lifecycle cost [57] along with techno-economic models available already benefited the researchers to carry forward the improvement of VRFB technology [58]–[60].

1.3 Interfacing VRFB with renewable energy sources

The electrical interfacing of the VRFB system with renewable sources like solar PV and the load end was indicated through impedance matching, including three subsystems: the VRFB stack, charge controller and inverter. The necessity of a charge controller for building an efficient BMS for VRFB was emphasized in the literature [61]. Considering the discontinuity in solar PV sources, the maximum power point tracking (MPPT) strategy should be applied for improved power conversion while charging the battery storage system using a sunlight based PV source [62]. Initially, a solar PV-based battery charge controller based on a high-efficiency DC-DC boost converter was demonstrated [63], [64]. A dc-dc buck converter operation and control for stand-alone solar battery charge controller were discussed by López et al. [65]. With an accentuation on sun-oriented PV charge controller, it might be noticed that the voltage excursion/cell in VRFB is about 38% when contrasted with that of same capacity lead acid battery which is about 20%. In this manner, the role of MPPT in VRFB charging is of higher priority than charging lead acid batteries. The major challenge in the design of the charge controller for VRFB is its synchronous control of charging current and flow rate to accomplish the maximum overall VRFB system efficiency. For quick charging of VRFB, the high current reasons for unnecessary ascent in temperature inside the VRFB stack may prompt untimely thermal shut down of the charging system to keep up the safe activity of VRFB. It might be noticed that VRFB experiences thermal precipitation at a temperature above 40˚C, as revealed in the literature [61]. Subsequently, the flow rate should be dynamically optimized to overcome the issues of stack temperature ascending past safe cut-off magnitude and deficient charging.

A dynamic flow rate control-based solar PV Maximum power point tracking (MPPT) charge controller for the VRFB system has been discussed. Its performance validation is shown under dynamic solar irradiance profiles [61]. The charging power conditioning unit (PCU) discussed in [61] is the DC-DC buck converter intended for efficient interfacing of the VRFB system with the PV source, as shown in **Figure 1.4**. Three distinctive charging algorithms are actualized on the developed charging system utilizing the dsPIC (dsPIC33FJ32MC204) controller, and their performances are evaluated to obtain the practically suitable charging algorithm. Other than the MPPT based CC-CV charging algorithm for augmenting the charging efficiency, the real time control of flow rate is also included in the charging algorithm to accomplish maximum overall VRFB system efficiency and controlled temperature ascend inside the VRFB stack. The modified charging algorithm additionally forestalls the chance of the controller's untimely thermal shutdown because of temperature rise beyond the permissible threshold and thus ensures complete charging of VRFB.

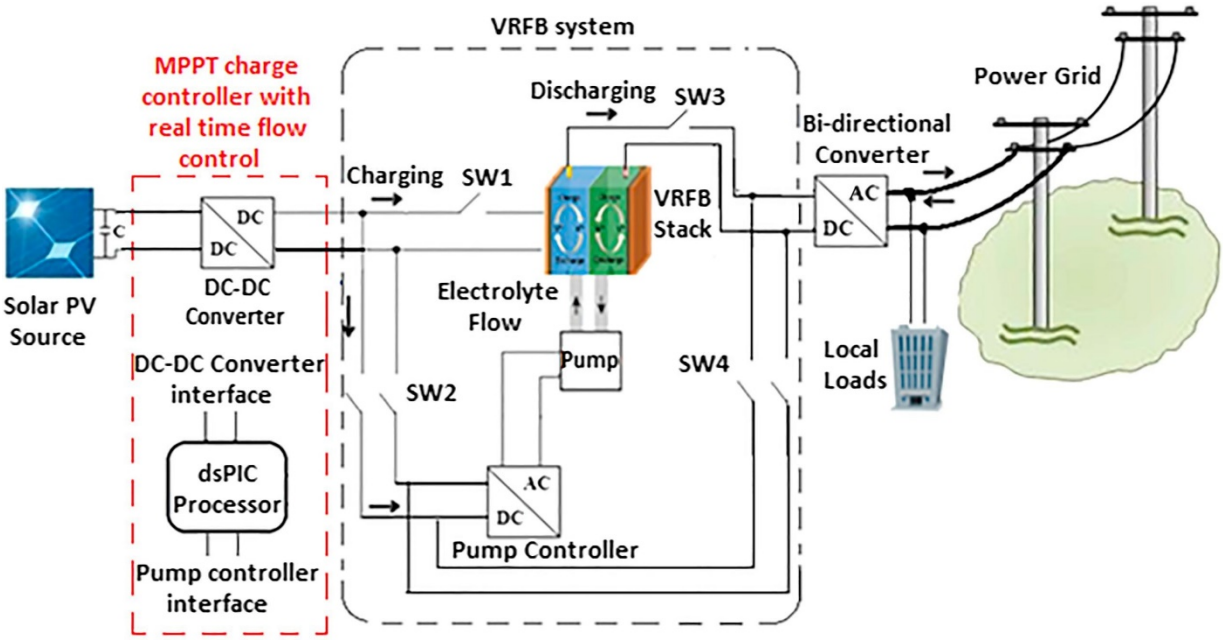

Figure 1.4: Block diagram representation of the solar PV MPPT based VRFB charge controller [61]

1.4 Gaps in the research works reported so far

- Even though equivalent circuit modeling is the widely adapted modeling approach, there are certain shortcomings in it as well. There are limitations of existing electrical equivalent models in analysing the dynamic control parameters of VRFB.
- The equivalent circuit modeling approach is limited to the investigation of electrical parameters only. Parameterising the dynamic real-time parameters, such as system losses, needs an efficient modeling tool that can address the non-linearity of VRFB. Artificial

Intelligence (AI)/Machine Learning (ML) is attractive due to its ability to handle model non-linearity and self-adaption attributes. Prediction of VRFB system losses will help estimate the overall VRFB system efficiency.

- To ensure the efficient operation of VRFB, an optimal flow rate must be maintained throughout the charge-discharge cycle. Real-time flow rate optimisation is a crucial factor in the flow battery operation. The existing literature has not addressed the real-time optimisation of the VRFB flow rate. Considering the non-linearity of VRFB, a robust global search technique in the form of a metaheuristic approach, such as Genetic algorithm (GA) or Particle Swarm Optimization (PSO) etc., is required to obtain the optimal flow rate more accurately for the nonlinear VRFB system.
- Interfacing VRFB with RES requires sophisticated power electronic circuitry. The existing literature has not investigated the optimised interfacing of VRFB storage with RES in detail. VRFB storage as a stationary energy storage solution, and RES can effectively meet the building energy demand. The optimised interfacing of VRFB storage with RES in satisfying the building energy demand is yet to be discussed.

1.5 Objectives

With the motivation to work on the existing research gap discussed in the previous section, the objectives of this research study are set as follows:

- Development of dynamic equivalent model of VRFB storage system for estimating its capacity fade.
- Prediction of VRFB storage system losses considering the dynamic operating conditions.
- Optimization of VRFB storage system losses considering the dynamic operating conditions.
- Development of a smart electrical interfacing system for long-life flow battery storage integrated Solar- EV charging stations with switchable Building Glazing.

1.6 Organization of Thesis

The research work has been conducted and reported in this thesis based on the above-mentioned objectives. The significant contributions of this thesis are as follows:

In chapter 2, a comprehensive dynamic equivalent model for estimating the capacity fade of VRFB storage has been implemented. Here, a MATLAB/Simulink based electrical equivalent model of VRFB storage considering the physical parameters has been proposed with an objective of interfacing VRFB with renewable energy sources. The impact of system

parameters like flow rate, self-discharge, pump power loss and charge-discharge profile has been considered for analyzing the VRFB storage system performance. The dynamic behavior of vanadium ion concentration in stack and tank has been considered in this work during the estimation of capacity fading of VRFB storage. The dynamic behavior of electrolyte volume in stack and tanks has been considered during the modeling. The optimization of electrolyte rebalancing has been proposed in this work to minimize the electrolyte volume loss during the operation. The proposed optimal scheduling of electrolyte rebalancing is significant for minimizing the capacity fading of VRFB storage in the long run. An optimal multi-objective flow management has been implemented for minimizing the capacity fade and voltage loss of the VRFB storage.

Prediction of battery storage system loss is necessary to improve the battery storage system's performance, reliability, and efficiency. In Chapter 3, the prediction of the overall system power loss of Vanadium Redox Flow Battery (VRFB) using different machine learning (ML) algorithms has been demonstrated for the first time. Under different operating current levels and electrolyte flow rates, the internal resistance variation and pump power consumption of the practical 1kW 6kWh VRFB system dataset have been considered for prediction. The prediction accuracy of ML algorithms has been analyzed in detail based on the regression metrics such as correlation coefficient (R^2), mean absolute error (MAE), and root mean square error (RMSE). The prediction results obtained in this work claim to be beneficial for designing optimised interfacing of VRFB storage with renewable energy sources and other power system applications.

Battery storage performance optimization is crucial in ensuring the reliable operation of renewable energy-integrated power systems and emergency backup applications. In Chapter 4, a kW scale VRFB storage system power loss optimization considering the dynamic operating conditions has been demonstrated. The multi-variable optimization considering both the VRFB pump power loss and stack power loss simultaneously has been executed in the proposed work. The electrolyte flow rate has been considered the control variable in optimizing the overall VRFB system power loss. Charge-discharge operations of VRFB with four sets of electrolyte flow rates at three different levels of stack terminal current have been taken to validate the proposed work. The optimal electrolyte flow rate obtained from Particle Swarm Optimization (PSO) algorithm has been compared with Nonlinear programming, and Genetic Algorithm (GA) techniques to propose the most suitable optimization technique for a kW scale VRFB storage.

In the countries like India, where the ambient temperature is higher during the significant span of the year, safe and efficient operation is needed for the delicate electronic panels and controllers installed in Electric Vehicle (EV) charging stations. In Chapter 5, therefore, for the first time in this work, solar-battery storage integrated switchable glazing topology has been applied for providing daytime passive heating ventilation and air conditioning (HVAC) in EV charging station control rooms. The EV charging station has been accompanied by a solar PV source installed on its roof-top to promote green energy and sustainable transportation. Vanadium redox flow battery (VRFB) has been integrated with the system to ensure energy security as a long-life energy storage solution. To satisfy the building glazing load demand under real-time dynamic environmental conditions, an Internet of Things (IoT) based smart scheduling of solar PV, VRFB storage and the local distribution grid has been demonstrated. The performance of the proposed system has been validated under four different transient scenarios; sunny, intermittent cloudy, prolonged cloudy and low solar irradiance with frequent grid outages. The proposed solution is a generalized one and thus can be very useful for scaled-up capacity. In Chapter 6, the Conclusion of the work is discussed.

Chapter 2

Comprehensive Dynamic Modeling of VRFB system

2.1 Introduction

Modeling of VRFB system is important for several reasons:

1) Predicting battery performance: An electrical equivalent model can predict the performance of a VRFB under different operating conditions, such as charge and discharge cycles, state of charge (SOC), and temperature. This information is essential for designing and optimizing the battery system.

2) Understanding internal behaviour: An electrical equivalent model can help understand the internal behavior of the VRFB, such as ion transport, and cell balancing.

3) Simulating battery behaviour: Simulation can help optimize the VRFB system performance and ensure the VRFB operates within safe and optimal parameters.

4) Validating experimental data: An electrical equivalent model can be used to validate experimental data from a VRFB, such as cell voltage, current, and impedance. This helps to ensure the accuracy of experimental data and provides confidence in the results.

So far in the existing literature, various improvements have been implemented in the modeling of VRFB storage. Bayanov et al. [34] optimized the parameters of VRFB, such as increasing the concentration of vanadium ions in the solution and usage of different redox couples to overcome the low energy density. Instead of deriving complex multi-physics equations, they designed a simple method of numerical modeling. VRFB storage models designed initially were equivalent circuit models. Those models [66], [67] can be utilized for only predicting the behavior of VRFB system parameters. However, the models were not validated experimentally. The VRFB system modeling lacked the effect of practically varying parameters like electrolyte concentration, flow rate and temperature on system operation. The capacity loss in VRFB is studied through the dynamic ion diffusion model by Rajagopalan et al. [68] Their model considered the self-discharge phenomena of VRFB and crossover of vanadium species. The drawback of the model was lack of experimental validation. Extended Kalman Filter approach [69] measured open-circuit voltage for charge-discharge experiments in a VRFB RC equivalent model. The simulation results are validated experimentally. The drawback of the approach was lack of study on the effect of dynamically varying practical

parameters. A MATLAB based model [70] gave detailed study on the validation of real time VRFB operation, but the effect of self-discharge was not discussed.

An equivalent circuit model as in reference [71] studied the self-discharge phenomenon in VRFB, but the model did not consider the cross-over of various species across the membrane. The model did not explain the effect of dynamic flow rate on energy efficiency. Zhang et al. [51] proposed a comprehensive equivalent circuit model of VRFB for extraction of internal parameters by fitting the experimental results into the model. The model considered the self-discharge phenomena and crossover of vanadium species. The model also considered the impact of flow rate on VRFB stack internal resistance. But the model lacked dynamic flow rate control. Xiong et al. [72] proposed an enhanced VRFB model with a second-order RC network to model electrochemical behavior and third-order cauer network to model heat transfer processes. The model addressed the thermal issues affecting VRFB system performance, which were not discussed in previous models. However, the model lacked dynamic flow rate control.

The application of VRFB in the RES demand realistic VRFB models [42]. Although there are some commercially available simulation software for modeling battery energy storage systems such as 'HOMER' which is mainly used for techno-commercial analysis of energy storage systems and micro-grid applications, sizing of battery and cost analysis etc., but for deeper analysis of electrical characteristics of batteries like VRFB and their interfacing with different subsystems in a hybrid micro-grid system, a dedicated electrical equivalent model of VRFB based on MATLAB or similar platform is required [73].

MATLAB/Simulink environment was utilized in designing a generalized VRFB electrical equivalent model. The robust model was designed including physical parameters such as dynamic flow rate, vanadium crossover, and internal resistance loss. Experimental validation was done with a practical 20 cell 1kW 6hr VRFB system [50]. The dynamic optimal flow rate control offered by the model was essential for consuming minimum pump power during charging. **Table 2.1** reports the analysis of the various electrical equivalent models. From **Table 2.1**, it can be inferred that the dynamic flow rate has not been considered during the modeling of VRFB system in most of the previous models. Also, most of the existing studies lacked the investigation on the impact of flow rate on internal parameters of VRFB system. In the long-term operation of VRFB storage, ion diffusions across the membrane and the depletion of active materials lead to the capacity fade in VRFB storage.

Table 2.1: Analysis on electrical equivalent models of VRFB system

Reference articles	Model Description	Experimental validation	Cross-over of vanadium species	VRFB Internal resistance under the SOC variation	Impact of flow rate on VRFB stack internal resistance	Consideration of dynamic flow rate during operation
[67]	A MATLAB based electrical equivalent model of VRFB with a control strategy for SOC Estimation	No	No	Yes	No	No
[68]	The capacity loss in VRFB is studied through dynamic ion diffusion model	No	Yes	No	No	No
[69]	RC equivalent model using kalman filter	Yes	No	No	No	No
[71]	Open circuit voltage source model	Yes	No	No	No	No
[51]	A comprehensive equivalent circuit model of VRFB for extraction of internal parameters by fitting the experimental results into the model	Yes	Yes	No	Yes	No
[73]	Precision dynamic parameter extraction methodology for VRFB stack under the variation of practical parameters (flow rate, SOC, Current)	Yes	Yes	Yes	Yes	Yes
[60]	MATLAB model for large scale application	No	No	No	No	No
[74]	A MATLAB based dynamic model characterizing the electrochemical and thermal parameters of VRFB	Yes	No	Yes	No	No
[75]	An enhanced VRFB model with second order RC network to model electrochemical behavior and third order cauer network to model heat transfer process	Yes	Yes	Yes	Yes	No

Minimizing capacity loss can significantly reduce the operation and maintenance cost in the long-term use of the VRFB system. In the existing literature, the estimation of capacity fade (aging) of VRFB storage in the long-term use has not been discussed in detail. Therefore, in this chapter, the modeling and estimation of capacity fade (aging) of VRFB storage has been implemented. The proposed model considers the migration of water molecules caused by osmotic pressure and ion crossover. In this way, the dynamic behavior of electrolyte volume and reactant concentrations has been described in this chapter. A MATLAB/Simulink based electrical equivalent model of VRFB storage has also been developed for analysing the impact of its dynamic system parameters on the system performance. The rest of the chapter is as follows: Section 2.2 details the electrical equivalent modeling of VRFB system, Section 2.3 discusses the modeling and estimation of capacity fade of VRFB system. Section 2.4 analyses the results. Section 2.5 summarizes the conclusion of this chapter.

2.2 Electrical equivalent modeling of VRFB system

VRFB storage system consists of two separate tanks containing electrolytes, a stack made up of graphite felts and two flow pumps for circulating the electrolyte between the tanks, and the stack. A Proton Exchange Membrane (PEM) is placed between the bipolar plates inside the battery stack. So far the researchers [76], [77] have reported that the widely used PEM are varieties of Nafion-based membranes. The unique feature of VRFB storage is that the electron transfer occurs at the electrodes, which is not in the case of other conventional batteries. This is one of the primary differences in the operation between conventional batteries and VRFB. In general, VRFB has a longer cycle life because the electrolyte, not the electrode, is the active material that is easily replenishable. VRFB has 4 different oxidation states; V^{2+}, V^{3+}, V^{4+} and V^{5+}. Where, V^{4+} and V^{5+} are in fact vanadium oxide ions (respectively VO^{2+} and VO_2^+). Thus, the chemical reactions that occur inside VRFB stack is,

$$VO_2^+ + 2H^+ + e^- \leftrightarrow VO^{2+} + H_2O \quad (2.1)$$

$$V^{2+} \leftrightarrow V^{3+} + e^- \quad (2.2)$$

$$V^{2+} + VO_2^+ + 2H^+ \leftrightarrow VO^{2+} + V^{3+} + H_2O \quad (2.3)$$

Equation (2.3) gives the summation of **Equation (2.1)** and **Equation (2.2)**. The Randles' equivalent circuit model can be used to depict the internal impedance parameters of a generic electrochemical cell. For batteries, the R-C equivalent circuit model can help understand the electrical characteristics. The electrical equivalent circuit of a single cell VRFB stack is

displayed in **Figure 2.1**. Here, the (R_{ct}^{c}) represents the charge transfer resistor in the electrode-electrolyte interface which always exists in the active region, double layer capacitor (C_{dl}^{c}) and solution resistor (R_{o}^{c}), which is predominant, for the catholyte side or the positive half-cell side. The anolyte or the negative half-cell side charge transfer resistance and double-layer capacitance are represented by (R_{ct}^{a}) and (C_{dl}^{a}) respectively. The electrode-electrolyte interface also offers a resistance equivalent as mass transfer resistance [78], [79] due to inadequate delivery of active vanadium species to the electrodes. Therefore, ($R_{ct}^{a\prime}$) and ($R_{ct}^{c\prime}$) shown in **Figure 2.1** represent the combination of charge transfer and mass transfer equivalent for anolyte and catholyte sides respectively. The mass-transfer resistance is dominant in low flow rate operation [80]. However, it is to be noted that VRFB storage system is preferred to be operated at moderate flow rates considering three factors; (1) overall stack internal resistance becomes comparatively low, (2) pump power consumption is also moderate, which improves VRFB system efficiency, (3) thermal management is satisfied. This eventually ensures the safe and optimized operation of VRFB system. Hence, in this work the mass transfer resistance has not been considered in the loss prediction process for moderate and high flow rate operation.

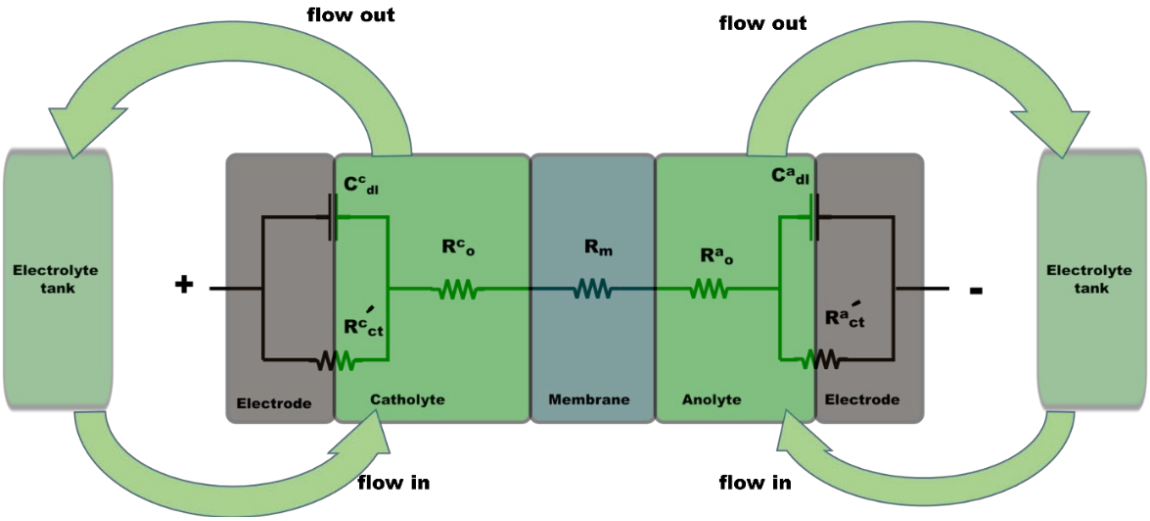

Figure 2.1: Electrical equivalent circuit of single cell VRFB stack

The series resistance element (R_s) is used in the Randles' equivalent circuit to represent a combination of solution resistance (R_o), and the membrane resistance (R_m). Further, (R_o) represents the sum of two half-cell electrolyte resistances (R_0^c) and (R_0^a) of VRFB stack. **Equation (2.4)** expresses the effective series resistance (R_s),

$$R_s = R_0^c + R_m + R_0^a \tag{2.4}$$

Figure 2.2 (a) represents a feasible VRFB stack model. Starting from the outer portion of the stack, the terminal current (I_t) can be further divided into three different current components. Three current components include stack current (I_s), shunt current (I_{sh}) and parasitic current (I_p). Among these three current components, stack current draws the maximum portion of terminal current during the charge-discharge operation of VRFB storage. Shunt current is the negligible magnitude of current which is less than 1% of the total terminal current, so it is not considered during the calculation of VRFB system power losses as reported in literature [73]. The parasitic current is the magnitude of current drawn by the control circuitry and pumps.

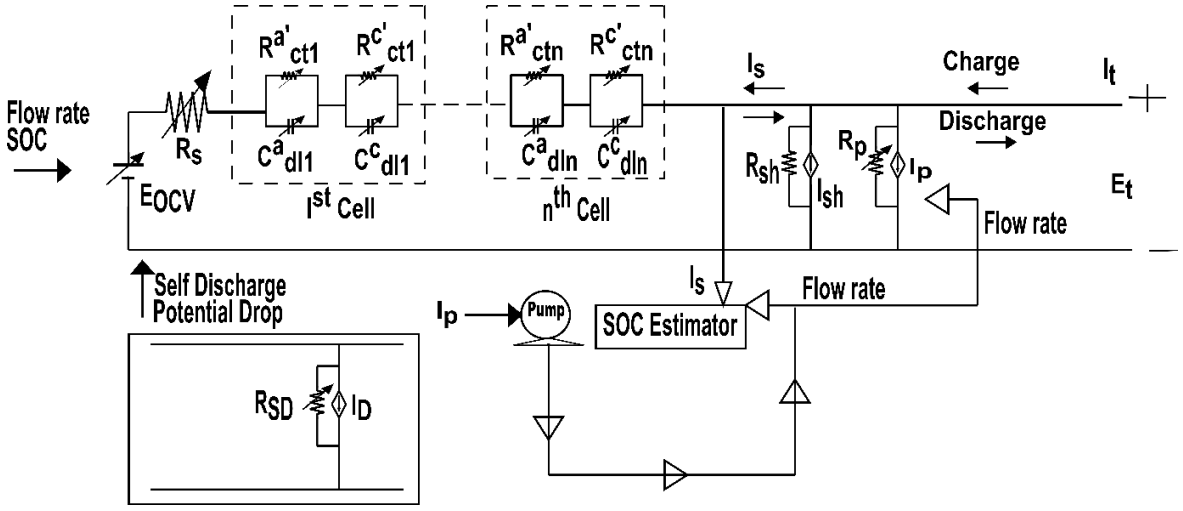

(a)

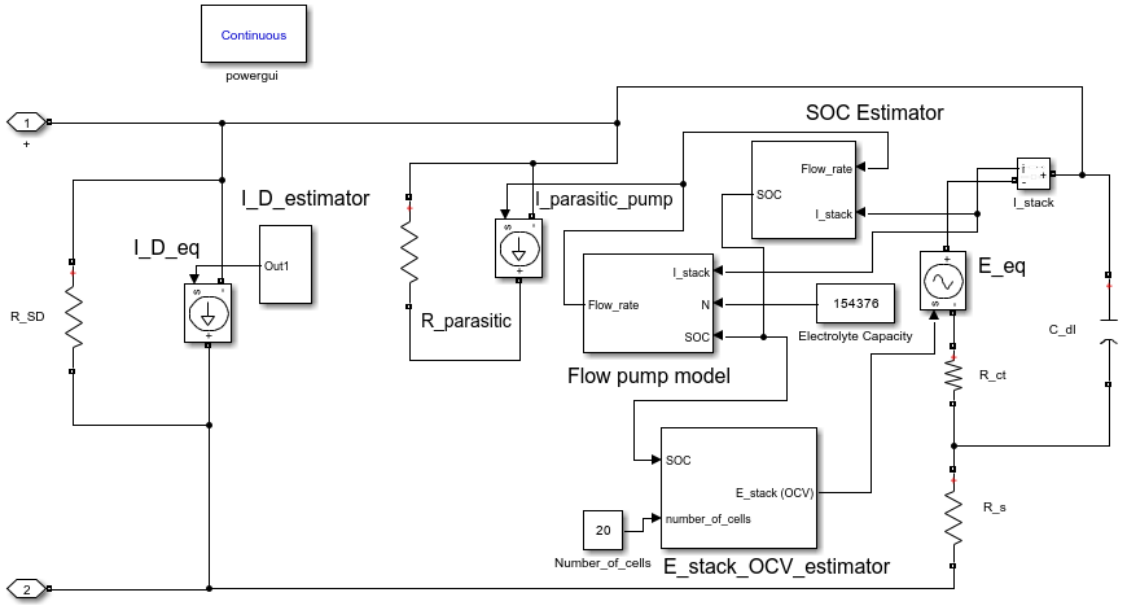

(b)

Figure 2.2: (a) Schematic of VRFB system electrical equivalent circuit; (b) MATLAB/Simulink model of VRFB system electrical equivalent circuit

Table 2.2 provides the parameter specifications of 1 kW 6 kWh VRFB system. The terminal voltage profile of 1 kW VRFB stack is displayed in **Figure 2.3**. The terminal voltage profile is obtained over the range of electrolyte flow rate from 3 L/min to 18 L/min. It can be inferred from **Figure 2.3** that there are two zones of operation: (1) Dynamic zone, till 0.1 SOC is reached; (2) Ohmic zone, from 0.1 SOC to 0.9 SOC.

Table 2.2: VRFB system parameters used for MATLAB/Simulink model

VRFB system parameters	**Rating**
Power capacity	1kW
Energy capacity	6kWh
Voltage range	(20-32) V
Rated stack current	60A
Each tank electrolyte volume	180 L
Electrolyte flow rate	(1-18) L/min
Number of series cell in stack	20
Dimension of each electrode ($L_{felt} \times W_{felt} \times D_{felt}$)	25 × 25 × 0.3 cm × cm × cm
Active electrode area	625 cm^2
Electrolyte Concentration	1.2 Mol/L
Current density	0.096 A/cm^2
Stack temperature range	15 - 35°C

It is a well-known fact that under fully charged conditions, the capacitor in a DC equivalent circuit acts as open circuit. Therefore, after 0.1 SOC, the voltage characteristic enters ohmic zone (linear), only the resistive effect remains till 0.9 SOC, as shown in **Figure 2.3** for a case study of 18L/min electrolyte flow rate.

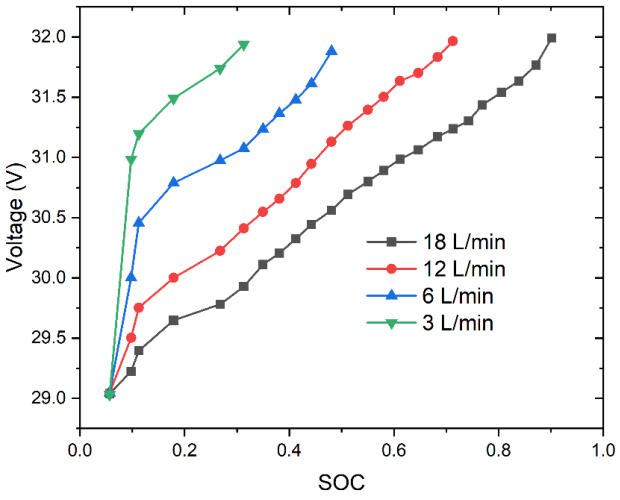

Figure 2.3: Variation of VRFB stack terminal voltage at 50 A charging current and four different flow rates (3 L/min, 6 L/min, 12 L/min and 18 L/min)

The same effect is realized in Figure 2.4 which demonstrates the characteristics of VRFB stack internal resistance (R_{int}). The VRFB stack internal resistance has been computed by feeding the charging characteristic profile as input to the electrical equivalent circuit model equations for different magnitudes of charging current over the range of electrolyte flow rate. Afterward, regression analysis is carried out. With increasing electrolyte flow rate, there is a reduction in the VRFB stack internal resistance.

Equation (2.5) represents the series combination of (R_s) and (R'_{ct}) to obtain the internal equivalent resistance for a VRFB stack as shown below,

$$R_{int} = R_s + R'_{ct} \tag{2.5}$$

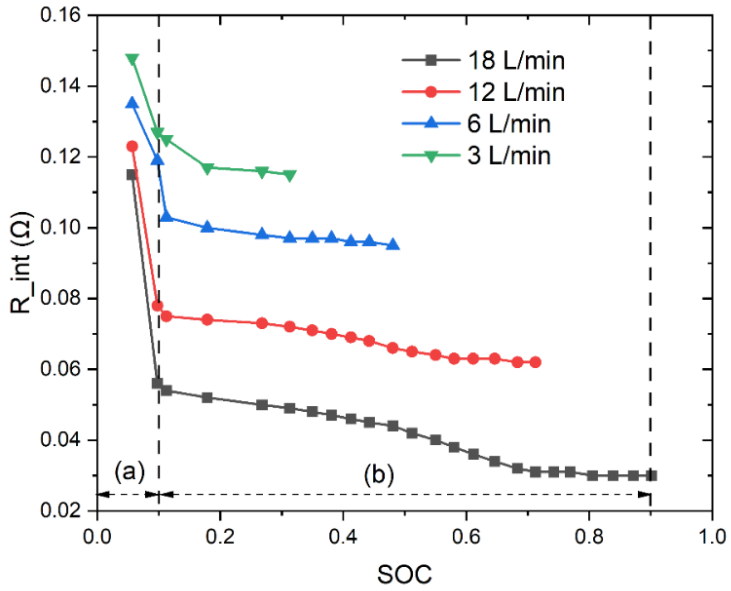

Figure 2.4: VRFB internal resistance under varying SOC and flow rate at stack current of 50 A, (a) represents the dynamic zone and (b) represents the ohmic zone

Equation (2.6) [81] denotes the terminal voltage of stack,

$$E_t = E_{OCV} + \{n \times (I_s \times R_{int})\} \tag{2.6}$$

Where (E_{OCV}) represents the open circuit voltage of the VRFB stack. (E_{OCV}) is expressed by **Equation (2.7)** [81],

$$E_{OCV} = n \times \left\{E_{Cell\_eq} + \frac{2RT}{F} ln\left(\frac{SOC}{1-SOC}\right) - I_d R_{SD}\right\} \tag{2.7}$$

Where 'n' represents the total count of series cells in the stack. 'E_{Cell_eq}' signifies the equilibrium potential of VRFB cell at 50% SOC. 'R' denotes the universal gas constant (8.314 J/(mol*K)), and the ambient temperature (K) is given by 'T'. 'F' denotes the Faraday's constant (96485 C/mol). 'I_d' represents the diffusion current (A). 'R_{SD}' denotes the self-discharge resistance. VRFB stack power loss (P_{stack_loss}) is expressed by,

$$P_{stack\_loss} = I_s^2 . R_{int} \tag{2.8}$$

The VRFB pump power consumption is expressed by **Equation (2.9)** [81],

$$P_{pump} = \frac{2(\Delta P_{stack} + \Delta P_{pipes}) Q(t)}{\eta_{pump}} \tag{2.9}$$

Where, 'ΔP_{stack}' denotes the drop in the magnitude of pressure inside the stack due to the parallel flow of electrolyte via each cell. During the flow of electrolyte through the horizontal and vertical paths, there is a drop in the magnitude of pressure inside the pipes which connects the tanks and stack. This pressure drop is denoted by 'ΔP_{pipes}'. '$Q(t)$' represents the electrolyte flow rate as function of time 't'. 'η_{pump}' signifies the pump efficiency. The overall VRFB system power loss 'P_{loss_VRFB}' is expressed by **Equation (2.10)**, where 'P_{stack_loss}' is the stack power loss obtained from **Equation (2.8)** and 'P_{pump}' is the pump power loss obtained from **Equation (2.9).**

$$P_{loss\_VRFB} = P_{stack\_loss} + P_{pump} \tag{2.10}$$

2.3 Modeling and estimation of Capacity fade (aging) of VRFB storage

The energy capacity of VRFB storage relies on the volume of electrolytes in the two tanks. Therefore, to formulate the capacity fading of 6 kWh VRFB system, it is important to estimate the electrolyte volume loss, which is a function of the electrolyte flow rate in cells. Finding the relation between the electrolyte flow rate across the membrane, and flow rate across the cells of VRFB is crucial. The workflow diagram for estimation of capacity fade in VRFB storage is shown in **Figure 2.5.** The dynamic model of VRFB storage consist of two individual models, (1) dynamic model for variation of vanadium ion concentration in stack and tank as discussed in **Section 2.3.1**, and (2) dynamic model for variation of electrolyte volume, detailed in **Section 2.3.2**. Electrolyte rebalancing is crucial in minimizing the capacity fade of VRFB storage in long run. During the continuous charge-discharge cycles, Capacity fade mainly occurs due to active species crossover in the membrane, which is reversible with electrolyte rebalancing

process. Most of the existing models have not implemented the optimal electrolyte rebalancing strategy to minimize the capacity fade. Therefore, optimal scheduling of electrolyte rebalancing is proposed in **Section 2.3.3** to minimize the capacity fade caused due to variation of electrolyte volume.

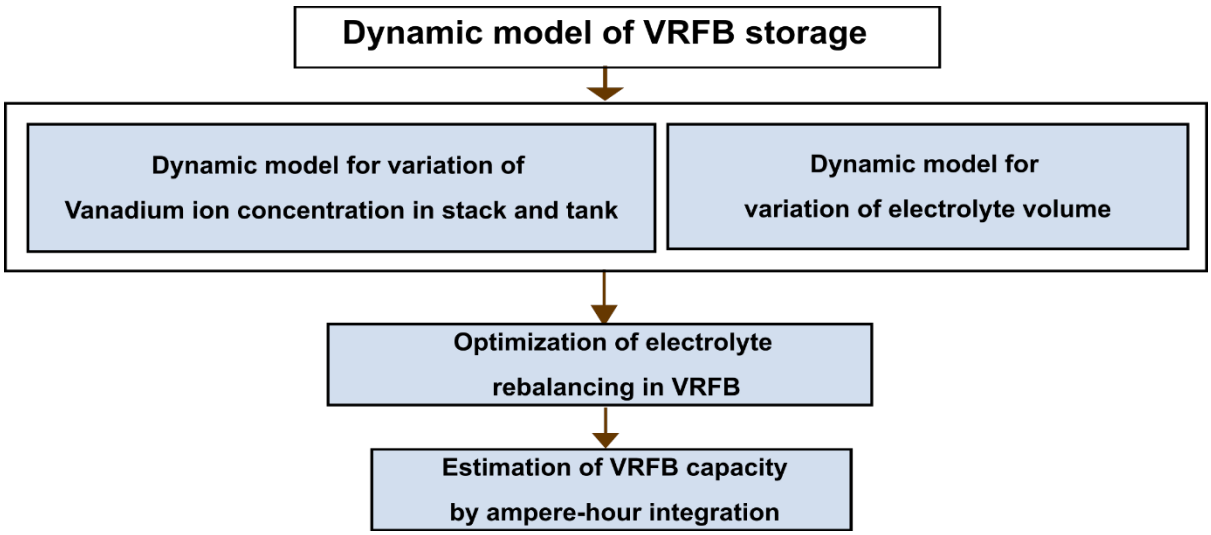

Figure 2.5: Workflow diagram for estimation of VRFB storage capacity fade

The block diagram depicting the working principle of VRFB charging and discharging cycling procedure is shown in **Figure 2.6(a).** The working principle of VRFB cycler comprises of three functional units; namely (i) Charge-Discharge Controller unit, which is used for monitoring the VRFB cell voltage and controlling the output electrical signals to VRFB cell for charging/discharging operation, (ii) Current Switching unit, for changing the direction of current from positive to negative electrode during charging as shown in red color, and negative to positive electrode during discharging as shown in blue color, and (iii) a galvanostat unit, for applying constant current through the VRFB cell. The flowchart of Constant Current – Constant Voltage (CC-CV) charge controller for VRFB storage has been displayed in **Figure 2.6(b).** In this work, three levels charging of a VRFB has been adopted. The three levels of VRFB charging include trickle charging level, bulk charging level, and float charging level. Initially, VRFB charging is commenced with the trickle charging level in which the trickle current (C/10) is applied to a VRFB, where "C" is the total ampere-hour (A-h) capacity of a VRFB. Trickle current avoids extreme heat generation in a VRFB stack. Followed by the trickle current, bulk charging current (C/3) is applied to the battery. At this instance, the battery voltage is enhanced through continuous charging until the "V_{oc}" limit is attained. The third level of charging is called the float charging level that ensures the complete charging of a VRFB. In this level of charging, constant voltage is maintained, and the magnitude of charging

current is reduced significantly to float current (C/100), until it reaches zero magnitude as shown in **Figure 2.6(b)**. Similarly, during the discharging cycle, VRFB is discharged at a constant current (CC) mode. The voltage of VRFB (V_{VRFB}) decreases until cut-off voltage is reached, then discharging cycle gets completed. In continuation, VRFB undergoes a charging cycle, thus repeating the charge-discharge cycles.

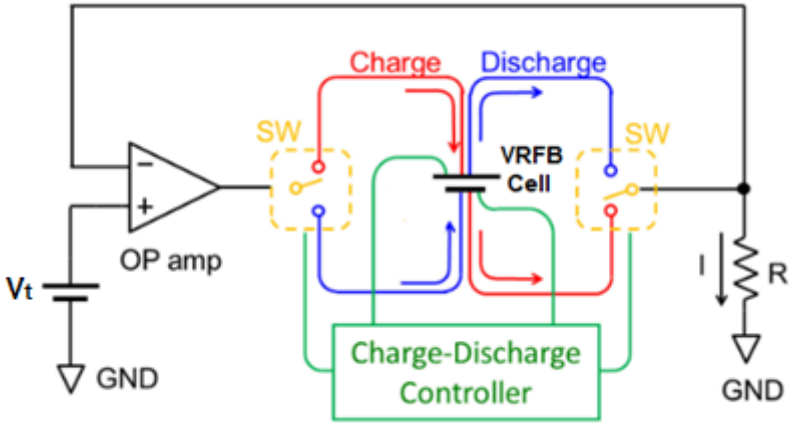

(a)

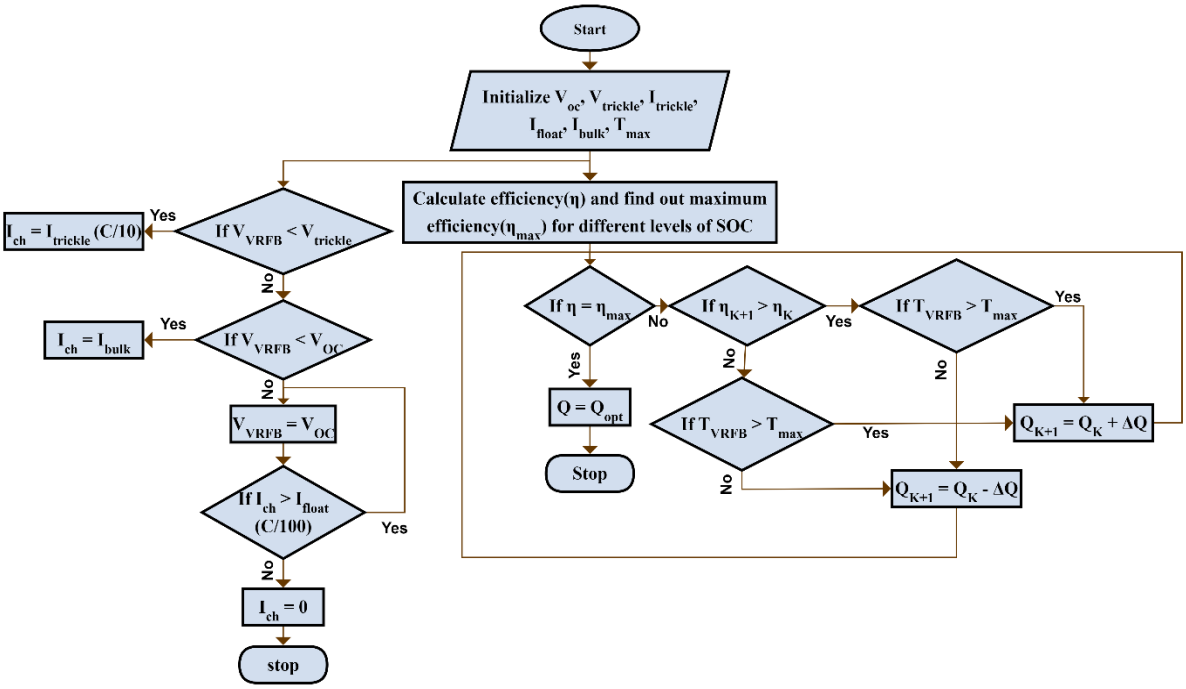

(b)

Figure 2.6: (a) Block Diagram depicting the working principle of VRFB charging and discharging cycling procedure, (b) Flowchart of the Constant Current – Constant Voltage (CC-CV) charge controller for VRFB storage

2.3.1 Dynamic behaviour of vanadium ion concentrations

According to conservation of mass and charge, the dynamic model of vanadium ions concentrations in stack can be obtained as follows [82],

$$\frac{V_s}{2}\frac{dc_2^s}{dt} = -\frac{NS_M}{d}(k_2c_2^s + k_4c_4^s + k_5c_5^s) + \frac{NJS_E}{zF} - \frac{NI_{shunt}}{zF} + 2Q_n(c_2^t - c_2^s) \quad (2.11)$$

$$\frac{V_s}{2}\frac{dc_3^s}{dt} = \frac{NS_M}{d}(-k_3c_3^s + 3k_5c_5^s + 2k_4c_4^s) - \frac{NJS_E}{zF} + \frac{NI_{shunt}}{zF} + 2Q_n(c_3^t - c_3^s) \quad (2.12)$$

$$\frac{V_s}{2}\frac{dc_4^s}{dt} = \frac{NS_M}{d}(-k_4c_4^s + 3k_2c_2^s + 2k_3c_3^s) - \frac{NJS_E}{zF} + \frac{NI_{shunt}}{zF} + 2Q_p(c_4^t - c_4^s) \quad (2.13)$$

$$\frac{V_s}{2}\frac{dc_5^s}{dt} = -\frac{NS_M}{d}(k_5c_5^s + 2k_2c_2^s + k_3c_3^s) + \frac{NJS_E}{zF} - \frac{NI_{shunt}}{zF} + 2Q_p(c_5^t - c_5^s) \quad (2.14)$$

where 'c_i' (i = 2, 3, 4, and 5) represents vanadium ions concentration at different oxidation states, and 'k_i' is the diffusion co-efficient of different vanadium ions,

'V_s' is stack volume, 'I' and 'J' are current and current density, respectively,

'Q' is flow rate, 'S' and $'d'$ represent the area and membrane thickness, respectively,

'z', 'F', and 'N' denote the number of electrons transferred in the reaction, the Faraday constant, and the cell number, respectively,

Superscript 's' and 't' represent stack and tank respectively,

Subscript $'n','p','M','E',$ and '$shunt$' represent negative, positive, membrane, electrode, and shunt current, respectively.

Equations (2.11) to (2.14) describe the variations in the concentrations of V^{2+}, V^{3+}, V^{4+}, and V^{5+} in the stack. These equations have four terms on the right side that describe different effects on concentrations. The first term accounts for ions crossover and side reactions, while the second term represents the impact of the main reactions. The third and fourth terms deal with the effects of shunt current and flow rate on concentrations, respectively.

In the tank, the dynamic behaviour of vanadium ion concentrations is determined by the convection and electrolyte volume variation as follows [82],

$$V_n^t\frac{dc_2^t}{dt} = 2Q_n(c_2^s - c_2^t) - c_2^t\frac{dV_n^t}{dt} \quad (2.15)$$

$$V_n^t \frac{dc_3^t}{dt} = 2Q_n(c_3^s - c_3^t) - c_2^t \frac{dV_n^t}{dt} \quad (2.16)$$

$$V_p^t \frac{dc_4^t}{dt} = 2Q_p(c_4^s - c_4^t) - c_4^t \frac{dV_p^t}{dt} \quad (2.17)$$

$$V_p^t \frac{dc_5^t}{dt} = 2Q_p(c_5^s - c_5^t) - c_5^t \frac{dV_p^t}{dt} \quad (2.18)$$

where V_n^t and V_p^t are electrolyte volumes in the negative and the positive tanks, respectively. After establishing the dynamic model that describes the dynamic behavior of vanadium ions concentrations, open circuit voltage of the VRFB stack (E_{OCV}) can be expressed, as shown in **Equation (2.7)**.

2.3.2 Dynamic behaviour of electrolyte volume

The dynamic behaviour of electrolyte volume can be obtained as follows,

Negative electrolyte side:

$$\frac{dV_n^t}{dt} = \frac{NM_2k_2c_2^sS_M}{d\rho} + \frac{NM_3k_3c_3^sS_M}{d\rho} + \frac{NM_4k_4c_4^sS_M}{d\rho} + \frac{NM_5k_5c_5^sS_M}{d\rho} + \frac{NM_JJS_E}{zF\rho} - \frac{NM_sI_{shunt}}{zF\rho} + \frac{N\kappa_p[(c_2^s+c_3^s+c_{H+}^{n,s})-(c_4^s+c_5^s+c_{H+}^{p,s})]RTS_M\rho_{H_2O}}{d\mu_\omega\rho} \quad (2.19)$$

where M_i (i = 2, 3, 4, 5) denotes molar mass of crossover particles,

'ρ' represents electrolyte density,

'ρ_{H_2O}' is the water density,

'κ_p' and 'μ_ω' are hydraulic permeability and viscosity of water, respectively.

'$c_{H+}^{n,s}$' and '$c_{H+}^{p,s}$' denote the proton concentrations on negative and positive sides of the stack, respectively.

Positive electrolyte side:

$$\frac{dV_p^t}{dt} = -\frac{dV_n^t}{dt} \quad (2.20)$$

After establishing the dynamic model describing the variations of reactant concentrations and electrolyte volume, the capacity of VRFB storage 'C' has been obtained by ampere-hour integration as follows,

$$C = \frac{|J|S_E t}{3600} \tag{2.21}$$

Figure 2.7 displays the MATLAB/Simulink model for the estimation of capacity fade of VRFB storage. Simulation is carried out based on the specifications of 1 kW, 6 hr VRFB storage. The value of '$\boldsymbol{N}$' is 20. The electrolyte concentration is 1.2 Mol/L. The result obtained from crossover and side reactions has been obtained in output port 1 as shown in **Figure 2.7**. The value of current density '$\boldsymbol{J}$' is 0.096 A/cm^2. The value of '$\boldsymbol{S_E}$' is 625 cm^2. Faraday's constant is 96485 C/mol. The result obtained from main reactions has been obtained in output port 2. The range of electrolyte flow rate '$\boldsymbol{Q}$' is from (1-18) L/min. The result obtained from convection has been displayed in output port 3. As shown in **Figure 2.7**, 'Add' block adds the results from each sub-model that includes main reactions, shunt reactions, crossover, and side reactions, respectively. 'Add 4' block has been utilized to add the output values obtained from output ports 1, 2, 3 and 4. The dynamic variation of vanadium ions in stack has been displayed in output port 7.

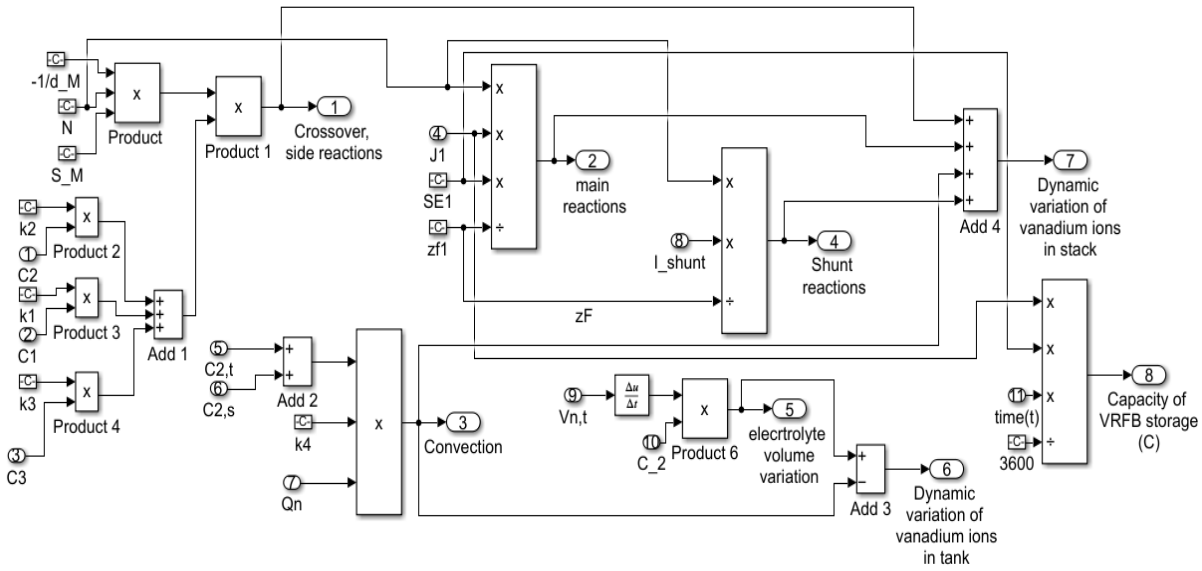

Figure 2.7: MATLAB/Simulink model of capacity fade of VRFB storage

The dynamic variation of vanadium ion concentration in tank as expressed in Equations (5) to (8) has been determined from output port 6. At the beginning of the simulation, the magnitudes of '$\boldsymbol{V_p}$' and '$\boldsymbol{V_n}$' are 180 L each. The dynamic variation of electrolyte volume has been obtained from output port 5. The input ports involved in determining the capacity of VRFB storage '$\boldsymbol{C}$' includes '$\boldsymbol{J}$' (0.096 A/cm^2), '$\boldsymbol{S_E}$' (625 cm^2) and time '$\boldsymbol{t}$'. The constant value '3600' has been included as an input variable for ampere-hour integration. The capacity of

VRFB storage has been determined using ampere-hour integration, the result has been obtained from output port 8.

2.3.3 Electrolyte Rebalancing

In flow batteries, the electrolyte does not degrade essentially, however the stack components (electrodes, membrane, etc.) degrade over time which is not reversible. Stack components must be replaced after their calendar life. Cycle capacity loss mainly happens due to active species crossover in the membrane, which is reversible with electrolyte rebalancing process. There is also a minor cycle capacity loss due to side reactions which is irreversible [83]. Both calendar and cycle degradations contribute to the total capacity fade. However, with the scheduling of electrolyte rebalancing, the reversible capacity fade can be mitigated.

2.4 Results and Discussion

A model for estimating capacity fade in VRFB storage is developed based on the following assumptions [84]:

(1) The gradient of vanadium ions concentrations is linearly distributed along the outlet direction.

(2) The density of positive and negative electrolytes remains constant, regardless of the influence of water molecule migration on electrolyte density.

(3) The inlet and outlet concentration of the stack is same as the tank outlet and inlet concentration respectively.

(4) The electrolyte temperature variation is negligibly small.

To study the effect of water molecule migration on battery capacity, the simulation results with and without water molecule migration has been shown in **Figure 2.8**. It can be observed from **Figure 2.8** that there is no such significant difference in the trends of both simulation results. Battery capacity decreases fast at the beginning of the cycles and finally reaches the steady state. However, there is a very noticeable difference between them in the final values. With the consideration of water molecule migration, the final capacity loss is 26.7 Ah and the capacity fading ratio is 22.2%. On the contrary, without the consideration of water molecule migration, the final capacity loss is 43.1 Ah and the capacity fading ratio is 36.2%. During the operation of VRFB storage, the charging current can be varied when charging VRFB storage as a load. Therefore, in order to explore the influence of asymmetric charging and discharging

currents on battery capacity, simulations has been executed under the condition that the discharging current is constant (45 A), but the charging current is variable (40 A, 45 A and 50 A).

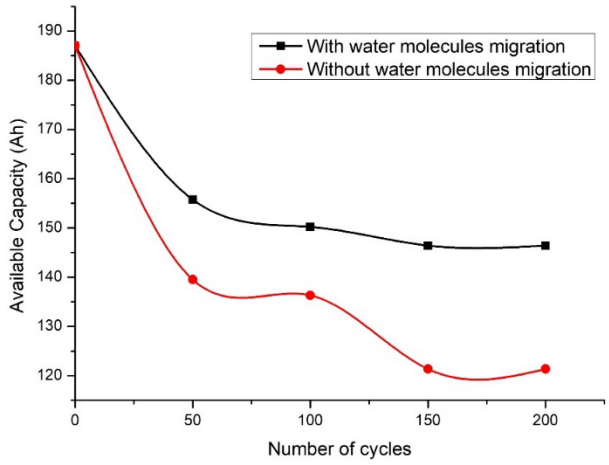

Figure 2.8: Variation of Available Capacity considering water molecules migration

The simulation results are shown in **Figure 2.9**. At the beginning of the VRFB charge-discharge cycles (0 to 100 cycles), the capacity fade is faster due to the crossover mechanism of active vanadium species, that includes convective crossover, diffusion and migration.

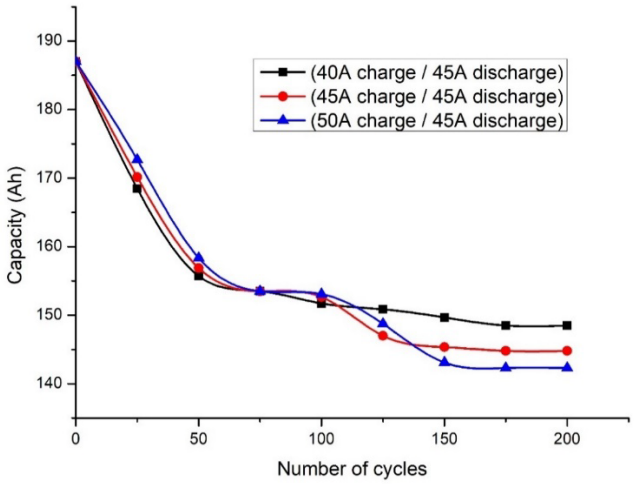

Figure 2.9: Variation of available Capacity applying asymmetric charge/discharge current

It can be observed from **Figure 2.9** at the end of charge-discharge cycles (150 cycles to 200 cycles) that, there is a stagnation in the capacity fade. The reason for the stagnation in the capacity fade is due to the decrease in the net convective crossover of the electrolyte at the end of charge-discharge cycles. The decrease in the net convective crossover leads to the reduction

in the crossover flux, which leads to the reduction in the overall capacity fade of the VRFB storage at the end of charge-discharge cycles (150 cycles to 200 cycles).

The variation of electrolyte volume during the discharge current of 40 A for 200 cycles is shown in **Figure 2.10**. Initially, the electrolyte volume in each tank is 180 L. It can be seen from the **Figure 2.10** that during the discharge, the positive electrolyte volume increases, while the negative electrolyte volume decreases. At the end of 200 cycles, the positive electrolyte volume is observed at 191.56 L. Negative electrolyte volume after 200 cycles is observed at 168.44 L.

VRFB storage experiences electrolyte imbalance during charge-discharge cycles, mainly caused by the transfer of water and vanadium ions across the ion-exchange membranes. If left unaddressed, this imbalance can lead to a gradual loss of capacity over time. Therefore, it is important to rebalance the electrolytes regularly to prevent cumulative capacity loss [85]. Before electrolyte rebalancing, the capacity fade has been observed to be around 202 mAh per cycle for 1 kW/6 kWh VRFB system from the simulation results. After 500 cycles of charge-discharge cycles, the capacity fade of 45% has been observed in the proposed work. Therefore, threshold capacity fade of 45% is considered in this work to mitigate the effect of reversible capacity fade in the long run. Therefore, for 1 kW/6 kWh VRFB storage, electrolyte rebalancing is scheduled after every 500 cycles to mitigate the capacity fade.

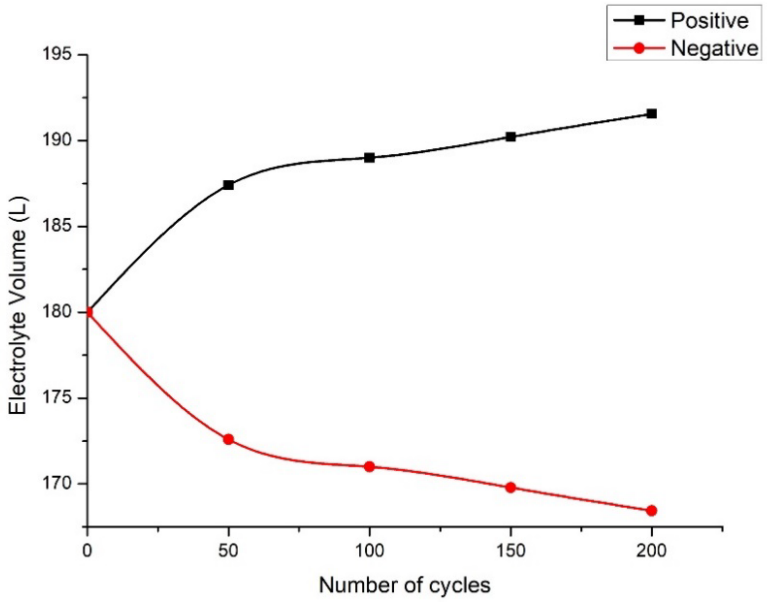

Figure 2.10: Variation of electrolyte volume in tanks over 200 cycles for 40 A discharge current

After electrolyte rebalancing, the dynamics of capacity loss in 1kW/6 kWh VRFB system has been studied for 1000 cycles of charge/discharge profiles. The capacity fade was observed to be 2.4 mAh per cycle for 1 kW/6 kWh VRFB system. The result of available capacity in VRFB storage is shown in **Figure 2.11.** As shown in **Figure 2.11**, the available capacity decreases from 187 Ah to 182.2 Ah after 1000 charge/discharge cycles with capacity fade of 2.56%. According to **Figure 2.11**, which shows the available capacity of VRFBs per cycle of charge/discharge, a mathematical relation is proposed to represent the available capacity of VRFBs in each cycle [86], as shown in **Equation (2.22).** A second-order polynomial function fitted to **Figure 2.11** curve as follows:

$$\text{Available capacity} = f(x) = ax^2 + bx + c \tag{2.22}$$

Where, x is the number of charge/discharge cycles.

The coefficients of the above polynomial function are found with 99% confidence bound. The coefficient $'c'$ is the total capacity of VRFB in the first cycle of the charge/discharge, it is equal to 187 Ah for the 20 cell, 1kW 6kWh VRFB system [73].

The coefficients $'a'$ and $'b'$ are -3e-7 and -0.018 respectively.

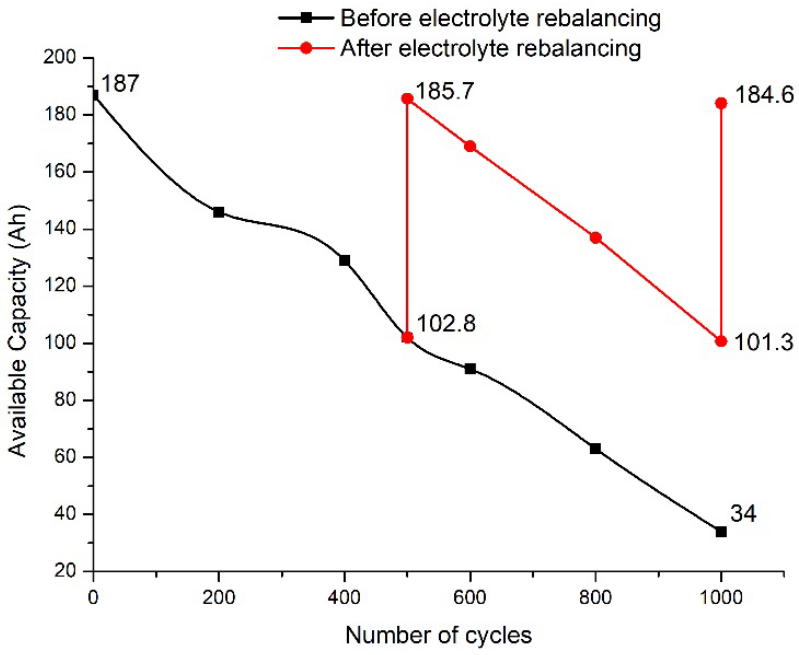

Figure 2.11: Available capacity in 1kW/6kWh VRFB system after 1000 charge/discharge cycles

Using Equation (2.22), the capacity fading of VRFB storage has been estimated for 20000 charge/discharge cycles, displayed in **Table 2.3**. After 20000 charge/discharge cycles, the

capacity fade of VRFB system is estimated to be 83.42 %. This implies that the VRFB storage is well-suited for long-life operation (more than 15000 cycles) as claimed in the literature [21], [87].

Table 2.3: Capacity fading in 1kW, 6kWh VRFB system after 20000 cycles of charge/discharge operation with systematic electrolyte rebalancing

Number of Cycles	Available Capacity (Ah)	Capacity fade (in %)
0	187	0
2000	182.2	2.56
4000	175	6.42
6000	165.4	11.55
8000	153.4	17.97
10000	139	25.66
12000	122.2	34.65
14000	103	44.92
16000	81.4	56.47
18000	57.4	69.3
20000	31	83.42

From the observation in **Table 2.3**, cycle life of VRFB system can be estimated. It can be observed that the viable cycle life comes to approximately 16000, considering the usable remaining capacity of VRFB storage. This cycle life is way greater than the other conventional battery storage solutions, thus making VRFB a viable long-life battery energy storage solution.

2.5 Conclusion

In this chapter, an electrical equivalent model has been proposed. The model can predict the performance of a VRFB system under different operating conditions, such as charge and discharge profiles, state of charge (SOC), and temperature. The overall system power loss of VRFB system has been calculated in this chapter. The results of the VRFB model proposed in this chapter are necessary for prediction and optimization of VRFB system power loss, which has been implemented in subsequent chapters 3 and 4 of this thesis. In this chapter, the modeling and estimation of capacity fade (aging) in VRFB storage has been implemented. The dynamic behavior of electrolyte volume and reactant concentrations has been considered during the estimation of capacity fade of VRFB system. The necessity of an optimal scheduling of electrolyte rebalancing has been emphasized, which is crucial for the efficient operation of VRFB storage in the long run. The capacity fading of VRFB storage has been estimated for

20000 charge/discharge cycles. After 20000 charge/discharge cycles, the capacity fade of VRFB system is estimated to be around 83.42 %. The results obtained in this chapter imply that the VRFB storage is well-suited for long-life operation (more than 15000 cycles).

Chapter 3

Machine Learning based Prediction of Vanadium Redox Flow Battery storage system power loss

3.1 Introduction

It is a fact that renewable energy sources (RES) such as solar, wind, etc. are inherently intermittent in nature. Therefore, storing the electrical energy generated from RES is essential for real-life applications to ensure energy security. In addition to ensuring energy security, the energy storage system utilized in the renewable energy systems must have the potential to provide reliable and long-term operation. Among the several available energy storage technologies, redox flow batteries (RFBs) are getting prominence for their ability to provide long-term, durable stationary energy storage applications. The flexibility offered by RFBs in scaling the energy capacity and power capacity separately is a unique feature which does not exist in the other established energy storage technologies. The stack size determines the power capacity, while the volume of the electrolyte determines the energy capacity of flow batteries. In addition to these, very long cycle life, deep discharge capacity, high columbic efficiency, safe operation due to exposed structure and quick response time are all advantages of RFBs[21], [87]. In RFBs, during charging and discharging process the electrolyte can itself be responsible for quickly transferring the generated heat from the stack to the tanks.

The aforesaid features of RFBs are the foremost reasons for its rapid growth in research and development. One among them is all-Vanadium Redox Flow Battery (VRFB) [22], [30], [88], which has been the most popular in large and medium scale renewable energy storage applications. Since the invention of VRFB in 1986, VRFB R&D has taken a tremendous leap forward. Its sensors, stack design, and control systems have been developed so far by researchers worldwide. The optimization of flow rate has been done to improve the system efficiency significantly. The use of commercial software such as COMSOL, MATLAB, etc. to model and simulate the VRFB system has improved the dynamics in the entire development of VRFB. Simulation aids in a more thorough examination of a system's performance under a variety of testing scenarios for designing efficient Battery Management System (BMS). An accurate diagnostic method for diagnosing the internal short circuit (ISC) current and current sensor fault have been proposed by Hu et al. [89], [90], which is helpful in designing the smart BMS for Li-

ion batteries. Further, Wei et al. [91] have addressed a thorough review on multi-dimensional sensing techniques for future smart BMS to ensure the optimized performance of Li-ion batteries. Similarly, accurate modeling and simulation studies can also be used to analyze and optimize the VRFB storage system performance [75], [92]–[97].

During the working of VRFB storage, electrolyte flow rate plays a vital role in controlling the system operation. Low electrolyte flowrates give inadequate electrolyte for the chemical reaction, causing formation of stagnant patches in the electrode. The VRFB performance improves as the electrolyte flowrate increases. Therefore, it is quintessential to obtain the optimal electrolyte flow rate, thereby improving the efficiency of VRFB storage system [98]–[100]. The equivalent models reported so far on VRFB system do not include prediction of its internal parameters and performance.

The estimation of the VRFB system performance under varying operating conditions (e.g. electrolyte flow rate, state of charge, charging currents, etc.) is necessary to address for on-field applications. The prediction of system parameters using ML-based models [101]–[104] is in surge now considering the accurate results offered by ML models. Their advantage lies in the fact that they do not require any complex mathematical formulation or quantitative correlation between input and output variables [105]–[107]. Large data sets of millions of data points are not mandatory for improving the accuracy of the Ensemble Learning (EL) based ML models [108], [109].

The comparison between the proposed work and the findings of the existing literature are displayed in **Table 3.1**. It can be observed from **Table 3.1** that the machine learning (ML) based prediction of VRFB performance in terms of its power loss due to battery stack resistance variation and pump power consumption has also not been reported so far in the literature. In this work, the prediction of VRFB system power loss under different charge-discharge conditions has been demonstrated for the first-time using ML-based regression models such as Linear regression, Support Vector Regression (SVR) and EL based Adaptive Boost (AdaBoost) technique. The accuracy of each technique has been analyzed and compared to recommend the best technique for VRFB system power loss prediction. A practical 1kW 6kWh VRFB system operational dataset has been utilized for performance validation of the ML-based predictive algorithms.

Table 3.1: Comparison among the existing literature and the proposed work for prediction of VRFB parameters

Literature	Methodology	Predicted parameter
Shen et al. [110]	Neural Network based model predictive control	Charge-Discharge power of VRFB for different electrolyte flow rate
Kandasamy et al.[109]	Artificial Neural Network (ANN) and Ensemble Learning	Charge/Discharge profiles of Stationary Battery Systems (VRFB, Li-ion)
Bao et al. [101]	Deep neural network	Estimation of surface reaction uniformity of VRFB electrodes
Proposed work	Machine Learning based approach (Linear Regression, Support Vector Regression (linear, cubic and quadratic) and AdaBoost)	Overall VRFB system power loss including stack power and pump power losses

The presented work is a generalized one and thus can be very useful for large scale VRFB system performance prediction while interfacing with renewable energy sources and other power system applications as well. The specific objectives of the work include:

1. To predict the overall VRFB system power loss using Machine Learning algorithms for the first time.
2. To consider the dynamic operating conditions of VRFB system for prediction of its power loss.
3. To analyse the prediction accuracy of five Machine Learning algorithms based on performance metrices and validation through practical VRFB system dataset.

The rest of the chapter is organized as follows; Section 3.2 gives a detailed description on the electrical equivalent modeling of VRFB storage system required for VRFB system power loss calculation. Section 3.3 discusses the ML-based models. Section 3.4.1 describes the experimental results; Section 3.4.2 comprises a detailed analysis and comparison of the results obtained in each ML-based model. Finally, the major contribution of the work is discussed in Section 3.5.

3.2 Electrical equivalent modeling of VRFB system

The detailed description on the electrical equivalent modeling of VRFB storage system required for VRFB system power loss calculation has been discussed in **Section 2.2** of this thesis.

3.3 ML-based models for VRFB system power loss prediction

ML is the study of computer algorithms that can automatically improvise its performance through experience and utilizing the data. ML is the subset of artificial intelligence (AI), an integral part of all modern technologies used in human life. Several ML models exist in the literature reported so far. The following are the most widely used ML and EL techniques to predict the unknown value [111]. These are Linear Regression (LR), Support Vector Regression (SVR) [112] and AdaBoost, a boosting technique based on EL [113]. Among these models, LR and SVR are individual models, whereas EL based AdaBoost model is based on the combination of several base models to produce an optimal predictive model. LR is one of the basic and most common regression models used to identify the statistical relationship among the variables. Based on the number of independent parameters, LR can be either univariate or multivariate. Multivariate LR attempts to model the relationship between two or more feature variables simultaneously by fitting it to a linear equation. In VRFB system, the univariate dataset is used to predict VRFB system loss. The objective function (J) for Linear Regression Models with one feature (VRFB system power loss) is given as follows,

$$J = \frac{1}{n} \sum_{i=1}^{n} L\,(\bar{y}_i - y_i)^2 \tag{3.1}$$

Where, 'y_i' is the actual/experimental VRFB system loss (P_{loss_VRFB}) obtained from **Equation (2.10)**, '$\bar{y}_i$' is the predicted VRFB system loss, 'n' represents number of data points and 'L' represents loss function which indicates the discrepancy between predicted and actual experimental VRFB system power loss values. The SVR model finds the best hyperplane with the help of different kernels (Linear, Cubic, and Quadratic) such that it has the best fit data points in the hyperplane. **Equation (3.2)** gives the objective function of SVR model and it is mentioned by 'M' as follows,

$$M = min \frac{1}{2} |w|^2 + C \sum_{i=1}^{n} |\xi_i| \tag{3.2}$$

subject to constraints (Z) expressed in **Equation (3.3),**

$$Z = |y_i - w_i x_i| \leq \varepsilon + |\xi_i| \quad (3.3)$$

In **Equation (3.2)**, '$|w|$' represents vector variable (VRFB system power loss), 'C' represents the hyper-parameter, '*min*' signifies minimization, 'n' represents the number of data points in the VRFB system power loss dataset. In **Equation (3.3)**, 'ε' represents the maximum error and 'ξ' denotes the deviation from the maximum error 'ε'. 'y_i' represents the predicted VRFB system power loss, 'w' represents the coefficient, 'x' signifies the experimental VRFB system power loss, 'ε' represents the maximum error and 'ξ' denotes the deviation from the maximum error 'ε'.

AdaBoost is a technique in which the weights are reassigned at each instance, where higher weights are assigned to incorrectly fitted instances. In AdaBoost, the weak learners are decision trees with a single split called "decision stumps". This method works by emphasizing more on difficult instances and less on those already handled satisfactorily [113]. The loss minimization equation of AdaBoost algorithm (*LM*) is expressed in **Equation (3.4)**,

$$LM = \frac{1}{m} \sum_{i=1}^{m} \exp\left(-y_i F(x_i)\right) \quad (3.4)$$

$$\text{Where, } F(x) = \sum_{t=1}^{T} \alpha_t h_t(x) \quad (3.5)$$

In **Equation (3.4)**, 'm' represents the number of data points in VRFB power loss dataset, 'x_i' represents the experimental power loss of VRFB system, 'y_i' represents the predicted VRFB system power loss and '$F(x)$' represents the weak learner of the AdaBoost algorithm. In **Equation (3.5)**, '$h_t(x)$' represents output hypothesis of weak learner '$F(x)$' and in each iteration 't', a weak learner is selected and assigned a coefficient (α).

Figure 3.1 describes the workflow of the proposed ML-based VRFB system power loss prediction. The performance metrics to measure the performance efficiency of the ML technique are Correlation coefficient (R^2), Mean Absolute Error (MAE), and Root Mean Square Error (RMSE). R^2 measures the relationship between the experimental data to the predicted value. The 'R' value range is in between [-1, 1], where '+1' represents the strong relation and '-1' represents the weak relation between the actual and predicted data. In this work, Pearson correlation coefficient has been used to measure the relation between the actual and predicted data. The over-fit of ML models is prevented by considering the Pearson correlation coefficient while analyzing the results. MAE is the average error (Experimental - Predicted) obtained for the data samples used in our experiment. The best value is '0', i.e., there

is no difference between the experimental and predicted value. In practical scenarios, the MAE should be near zero. RMSE measures the deviation between the experimental and predicted values. In most of the works, it is used to measure the quality of the predictions made by the ML models. The prediction results are said to be of high quality if the RMSE value is lower. Section 3.4.1 describes the experimental results and discusses the results obtained from ML/EL models.

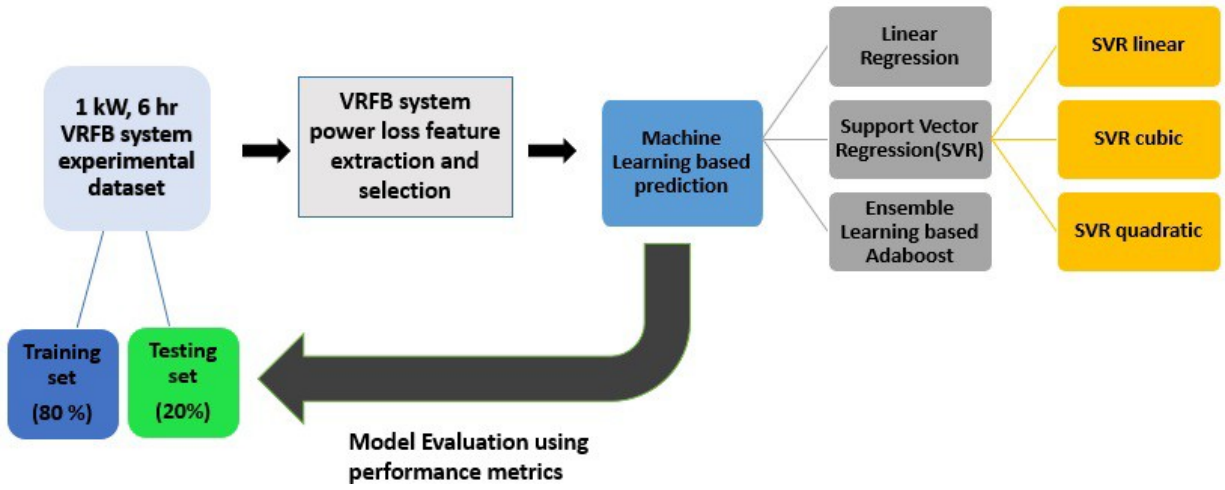

Figure 3.1: Flow diagram of the proposed ML-based VRFB system power loss prediction

3.4 Results and discussion

3.4.1 Experimental results

The experiment has been performed with a 1 kW 6 kWh VRFB system. The experimental setup and its block diagram representation has been shown in **Figure 3.2**. Programmable Logic controller (PLC) has been utilized during the experimentation to control the electrolyte flow rate pumped from the external tanks. PLC acts as the primary controller in tuning the variation of stack current.

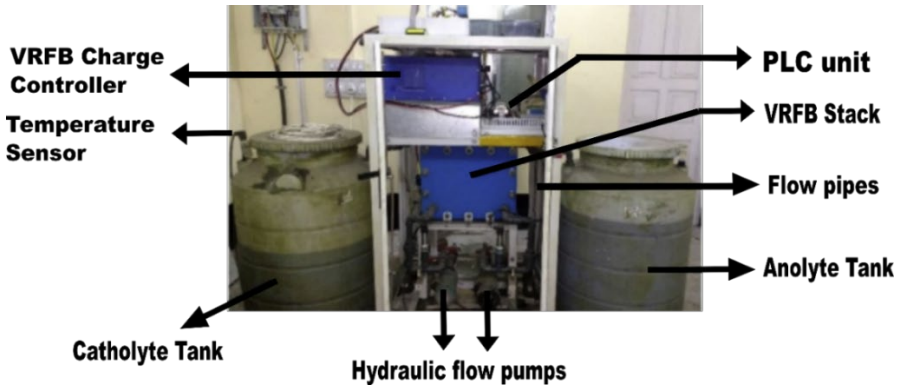

(a)

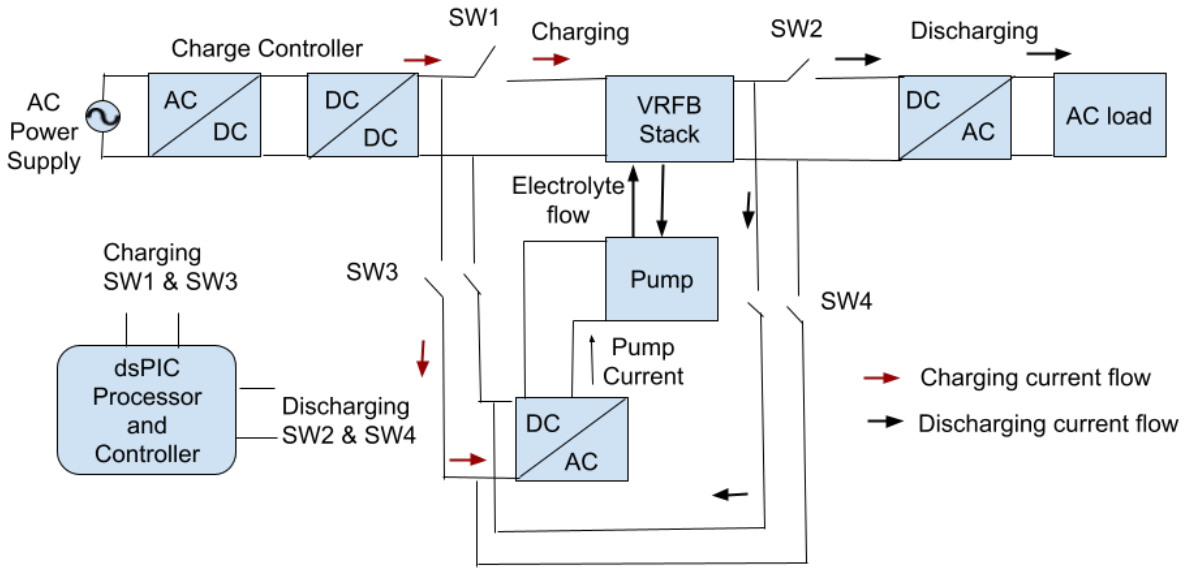

Figure 3.2: (a) Experimental set up of 1 kW, 6 kWh VRFB system; (b) Block diagram representation of the experimental set-up

The experiment has been performed for three sets of stack currents (40 A, 45 A and 50 A) under different electrolyte flow rates ranging from 3 L/min to 18 L/min. The magnitudes of stack current selected for the experiment are 40 A, 45 A, and 50 A, respectively, to assure the safe operation of the VRFB storage given that the highest permissible stack current rating of the VRFB storage is 60 A. A variable frequency drive (VFD) has been utilized to regulate the operation of pump during the varying operating range of electrolyte flow rate. During the experimentation, the electrolytes flow rates have been tuned at the magnitudes of 3 L/min, 6 L/min, 12 L/min, and 18 L/min, respectively for the 1 kW 6 kWh VRFB system. A power meter with an accuracy of around ± 1% has been used for measuring the pump power. The efficiency of the pump increases with an increase in flow rate. In this work, the pump efficiencies are 12%, 30 %, 35 %, and 40 % for 3 L/min, 6 L/min, 12 L/min and 18 L/min respectively. Considering the lower pump efficiency of hydraulic flow pump at low flow rate, it is advisable to operate the VRFB system at least at moderate flow rates.

Table 3.2 demonstrates the experimentally measured data in terms of the mean power loss of the VRFB system obtained from 0.1 SOC to 0.9 SOC. The total power loss of VRFB system is the sum of VRFB pump power loss for each flow rate and the VRFB stack power loss as expressed in **Equation (2.10)**. Therefore, the hydraulic pump power consumed during the operation of VRFB storage system must be optimized to achieve higher system efficiency. From the experimental results in **Table 3.2**, it has been observed that the increase in flow rate has significantly increased the VRFB pump power loss, whereas the mean VRFB stack power loss

has decreased. Therefore, a trade-off is needed between electrolyte flow rate and VRFB stack power loss. As a case study, for stack current of 40A, with increase in electrolyte flow rate from 6 L/min to 12 L/min, the VRFB pump power loss has increased by 8.19 W. Furthermore, the mean total VRFB system power loss has decreased by 25.48 W, obtained from **Table 3.2**.

The trend in the experimental results observed in this work offers further scope of performing the prediction of VRFB system power loss under different operating conditions. Accurate prediction of VRFB system loss will lead to its optimized interfacing with renewable energy sources and other power system applications. Section 2.4.2 discusses the prediction results of VRFB system using ML-based models under different operating scenarios.

Table 3.2: Total VRFB system power loss for different stack currents (40 A, 45 A and 50A) of 1 kW, 6 kWh VRFB system

Stack Current (A)	Electrolyte flow rate (L/min)	Mean VRFB Stack power loss (W)	VRFB Pump power loss (W)	Mean Total power loss of VRFB system (W)
40	3	343.43	0.6	344.03
	6	304.47	1.05	305.52
	12	270.8	9.24	280.04
	18	240.04	22.83	262.87
45	3	389.29	0.603	389.893
	6	343.12	1.054	344.174
	12	304.42	9.28	313.7
	18	269.06	22.91	291.97
50	3	432.78	0.605	433.385
	6	382.03	1.059	383.089
	12	338.25	9.31	347.56
	18	294.09	22.97	317.06

3.4.2 Simulation results and model validation

The stack current profiles of 1 kW, 6 kWh VRFB system have been utilized to predict the VRFB system power loss. Google Colab platform has been used in this work to execute ML algorithms on a practical dataset of 17100 samples in PC with a 16 GB RAM, Intel I7 processor (2.9 GHz). Google Colab offers a faster execution time (less than 10 seconds approximately). The real-time charging profile experimental data of three stack currents (40 A, 45 A, and 50 A) has been used to predict VRFB system power losses. The dynamics of VRFB system operation have been incorporated in this work by analyzing the performance of ML models in predicting the power loss of the VRFB for four different flow rates (3 L/min, 6 L/min, 12 L/min, and 18 L/min). To achieve the generalization capability of the ML/EL models, dataset of 17100 samples is randomly split into 80% training data (13680 samples) and 20% testing data (3420 samples). VRFB system power loss prediction is carried out using 5 ML techniques, namely LR, SVR linear, SVR quadratic, SVR cubic and EL based AdaBoost technique as mentioned in section 3.3. The ML/EL models proposed in this work are trained with Scikit-Learn python module [114]. Hyperparameter tuning is an important step in any machine learning model training that directly influences the model performance. The Grid Search Method (GSM) [115]–[117] with tenfold cross-validation has been implemented in this work for hyperparameters tuning. The utility of GSM for cross-validation has effectively improved the accuracy of ML/EL models over an iterative process. The prediction results with the best accuracy are obtained after comparing the cross-validation results to select the best-fit model. The ease of implementation, reliability and low dimensionality are the primary reasons for selecting GSM in hyperparameter tuning. The optimal hyperparameters tuning is achieved by using 'GridsearchCV' object (where CV refers to cross-validation) in Scikit-Learn. During the tuning process, the best results of the proposed ML/EL models were obtained at the learning rate of 0.2 (over the range of learning rates from 0.1 to 0.5), and the number of estimators at 100 (over the range of estimators from 10 to 150) after applying the ten-fold cross-validation[116], [117]. The performance metrics (Root Mean Square Error (RMSE), Mean Absolute Error (MAE), and Correlation Coefficient (R^2) values were obtained to analyze the results of the proposed ML techniques after tuning of hyperparameters as shown in **Table 3.3**. R^2 value indicates the correlation between the actual experimental response and the predicted response of the model. R^2 value signifies the goodness of a fit of a model. R^2 value close to 1 signifies that the model performs with good accuracy. Among the 5 different ML techniques, the AdaBoost algorithm-based results are found to be the most suitable with the best R^2 values closer to '1' for different

stack current profiles in VRFB system loss prediction. Considering the prediction results of ML techniques for the flow rate of 3 L/min in stack current of 40 A, R^2 value is the highest for AdaBoost technique (R^2 = 0.983) in comparison with LR (R^2 = 0.919), SVR linear (R^2 = 0.921), SVR cubic (R^2 = 0.827) and SVR quadratic (R^2 = 0.831). The trend is similar for all the remaining three flow rates varying in terms of stack currents. In addition to R^2 value, MAE and RMSE values as shown in **Table 3.2** also signifies AdaBoost technique performs with the best accuracy among the 5 ML techniques used in this work. MAE and RMSE values must be lower for the model to be more accurate. RMSE values for flow rate of 3 L/min of stack current 40A shows that the RMSE value of AdaBoost technique (RMSE = 5.321) is the lowest in comparison with LR (RMSE = 11.325), SVR linear (RMSE = 9.123), SVR cubic (RMSE = 19.832) and SVR quadratic (RMSE = 19.152). The graphical results of ML-based model are shown in **Figure 3.3** for a stack current of 50 A and flow rate of 18 L/min. A superior performance is observed for the VRFB system power loss prediction with high accuracy. In **Figure 3.3**, Actual power loss is displayed in straight line and the predicted power loss of VRFB system is displayed in dotted lines. The performance of EL based AdaBoost technique is better than LR and SVR techniques. The predicted VRFB power loss plot of AdaBoost technique has minimal deviation from the actual VRFB power loss plot.

Table 3.3: Comparison of prediction accuracy of ML/EL models for different stack currents and flow rates

Stack Current (A)	Electrolyte flow rate (L/min)	Error Parameters														
		Linear Regression			SVR Linear			SVR Cubic			SVR Quadratic			AdaBoost		
		R^2	MAE	RMSE	R^2	MAE	RMSE	R^2	MAE	RMSE	R^2	MAE	RMSE	R^2	MAE	RMSE
40	3	0.919	9.752	11.325	0.921	6.546	9.123	0.827	12.362	19.832	0.831	13.685	19.152	0.983	2.963	5.321
	6	0.915	10.998	14.366	0.923	5.384	8.698	0.847	13	18.645	0.836	12.323	17.98	0.989	4.254	4.636
	12	0.937	10.232	17.358	0.956	6.874	10.684	0.869	11.851	16.656	0.881	10.546	12.784	0.987	3.963	4.121
	18	0.923	8.465	15.987	0.946	4.684	11.654	0.849	13.875	19.785	0.847	11.545	13.634	0.991	3.457	3.971
45	3	0.952	9.212	19.639	0.961	5.337	10.365	0.857	12.969	20.215	0.841	12.423	15.634	0.994	4.875	4.231
	6	0.961	9.011	11.323	0.978	8.265	8.754	0.866	11.025	21.363	0.859	11.121	18.542	0.996	3.858	3.212
	12	0.968	8.966	12.356	0.975	7.365	7.695	0.877	12.664	18.412	0.894	10.754	16.695	0.995	5.632	3.587
	18	0.955	9.877	11.036	0.948	9.661	8.662	0.899	13.852	19.362	0.867	11.423	18.362	0.983	4.828	4.213
50	3	0.928	9.996	12.365	0.903	5.036	10.633	0.861	14.745	18.546	0.853	14.363	20.674	0.988	3.548	3.745
	6	0.931	10.312	10.578	0.945	6.224	9.641	0.859	10.561	17.365	0.849	12.213	16.475	0.981	4.478	4.213
	12	0.959	9.632	11.002	0.935	5.736	7.456	0.858	11.574	16.332	0.846	12.748	13.874	0.979	3.141	4.458
	18	0.945	8.465	10.062	0.965	3.281	7.999	0.839	11.898	17.168	0.839	11.898	17.168	0.99	3.242	4.073

It is observed from **Figure 3.3 (a, b, c & d)** that there is an increase in the deviation between the actual and predicted plot at the end of charging profile in LR and SVR techniques. Furthermore, EL based AdaBoost technique performs better at the end of charging profile as well as shown in **Figure 3.3 e**.

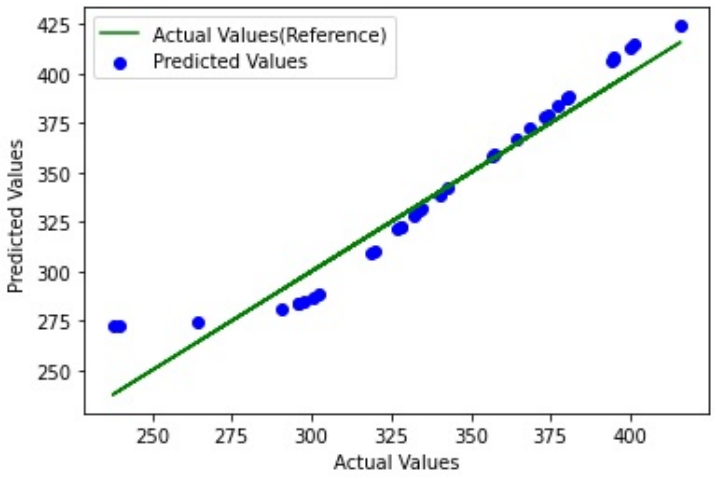

(a)

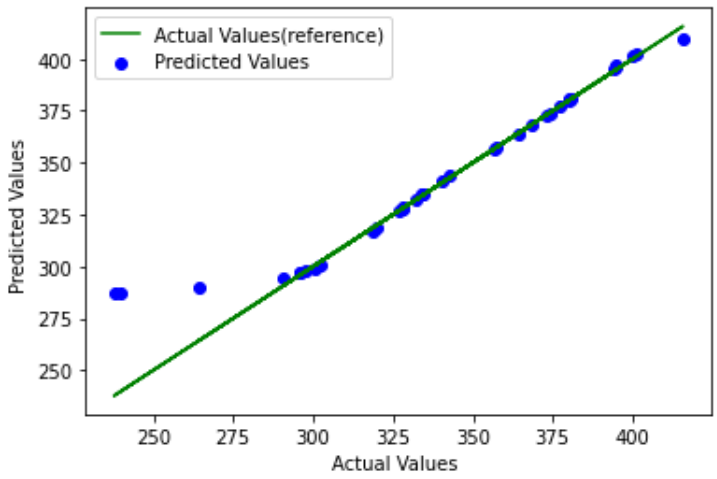

(b)

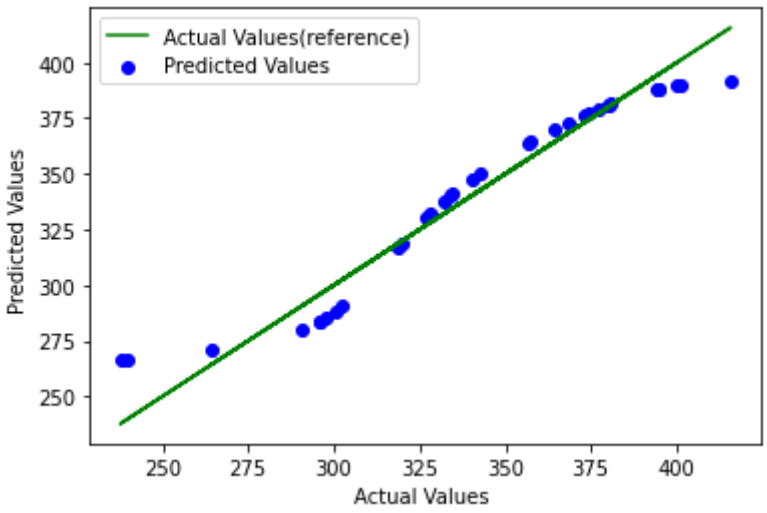
Actual Values(reference)
Predicted Values
Predicted Values
Actual Values
250
275
300
325
350
375
400

(c)

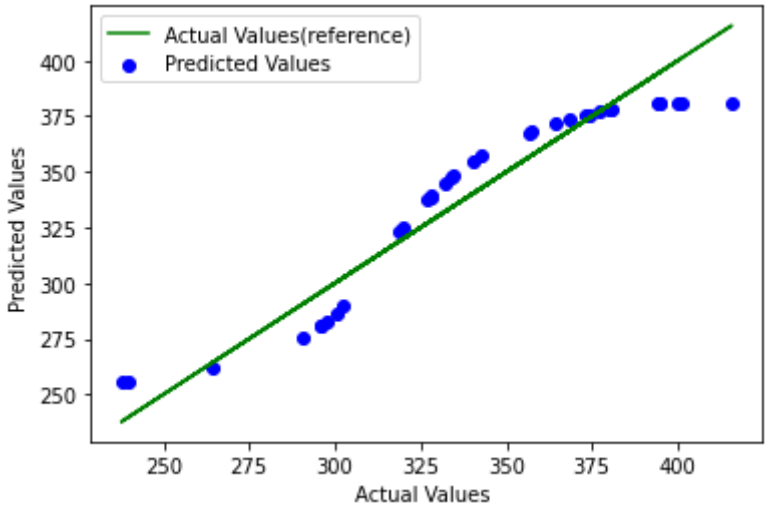
Actual Values(reference)
Predicted Values
Predicted Values
Actual Values
250
275
300
325
350
375
400

(d)

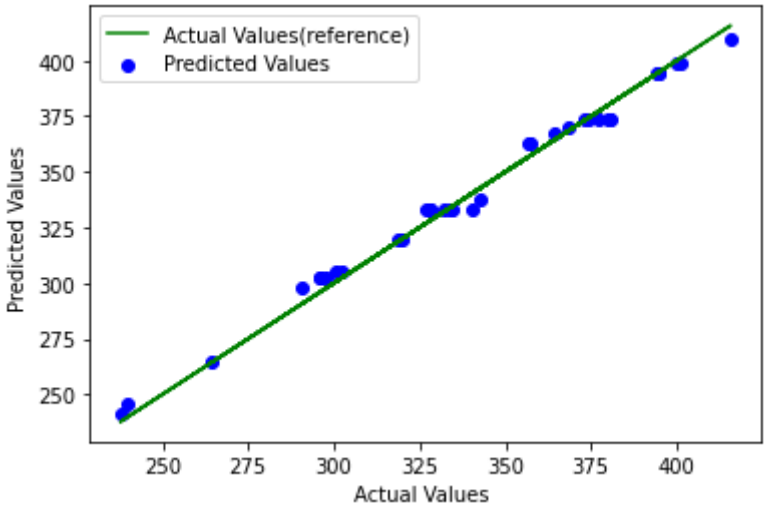

(e)

Figure 3.3: Actual VRFB system power loss vs Predicted VRFB system power loss in 1kW 6h VRFB system for 50 A stack current profile with a flow rate of 18 L/min. Prediction results of ML techniques namely, (a) Linear Regression; (b) SVR Linear; (c) SVR Quadratic; (d) SVR Cubic; (e) AdaBoost

The prediction results obtained from the AdaBoost algorithm have been further compared with the experimental data in **Table 3.4.** The relative percentage error between the experimental results and AdaBoost based prediction results has been obtained within the range of 0.4 % to 2.1 %. The lower magnitudes of relative percentage error signify that the prediction results obtained from AdaBoost algorithm is of higher accuracy. AdaBoost technique converts a set of weak predictors (features) into a single strong predictor over the iterations. Initially, equal weights are given to all the predictors. During the iteration, the AdaBoost algorithm emphasizes updating the predictors that show weak learning capability. By training and updating the weak predictors, the lower error is achieved during the prediction. It is to be noted from the results that EL based AdaBoost technique does not exhibit the overfitting of data during both training and testing, thereby ensuring a stable prediction performance. These advantages make the AdaBoost technique the best choice for achieving better prediction performance in comparison to the other individual ML models utilized in this work.

The prediction results obtained at different flow rates and stack current is very helpful in further optimizing the electrolyte flow rate thereby significantly enhancing the efficiency of the VRFB storage during operation. The results obtained in this work is helpful for engineers and researchers working on the redox flow battery ESS to utilize the ML techniques in further investigation and optimization of the VRFB storage system performance.

Table 3.4: Comparison between experimental and AdaBoost based prediction results

Stack Current (A)	Electrolyte flow rate (L/min)	Mean Total Power loss of VRFB system (W)		$Relative\ percentage\ error = \frac{ER - PR}{ER} * 100$ (%)
		Experimental result (ER)	AdaBoost based Prediction result (PR)	
40	3	344.03	338.18	1.70
	6	305.52	302.16	1.10
	12	280.04	276.39	1.30
	18	262.87	260.5	0.90
45	3	389.89	386.95	0.75
	6	344.17	342.79	0.40
	12	313.66	312.09	0.50
	18	291.89	286.93	1.70
50	3	433.38	428.18	1.20
	6	383.08	375.8	1.90
	12	347.49	340.19	2.10
	18	316.92	313.75	1.00

3.5 Conclusion

The major findings of this chapter are mentioned in this section. The overall system power loss of Vanadium Redox Flow Battery (VRFB) has been predicted using five ML algorithms. The prediction accuracy of ML algorithms has been analyzed in detail based on the regression metrics such as correlation coefficient (R^2), mean absolute error (MAE) and root mean square error (RMSE). The ML-based predictive models have been trained and validated by experimental dataset of a 1kW 6h VRFB storage system under different stack terminal currents and electrolyte flow rates. The simultaneous consideration of VRFB stack power loss and pump power loss in predicting the overall VRFB system loss leads to accurate performance analysis. It is observed that EL based AdaBoost algorithm exhibits superiority in predicting VRFB system loss compared to that of linear regression (LR), support vector regression (SVR) algorithms. The AdaBoost algorithm statistically presents the best prediction accuracy with prediction error parameters obtained as R^2, MAE and RMSE of around 0.99, 3.242 and 4.073 respectively for 50 A stack current profile with a flow rate of 18 L/min, as a sample case. Similarly, for the other

current levels and flow rates, the performance of the ML algorithms has been analyzed as mentioned earlier in **Table 3.3**. The prediction results obtained from the AdaBoost algorithm has been further compared with the experimental data in **Table 3.4** and the relative percentage error has been found in the range of 0.4 % to 2.1 %. The lower magnitudes of relative percentage error signify that the prediction results obtained from AdaBoost algorithm is of higher accuracy. The proposed ML-based prediction results of VRFB system power loss further claims to be very useful during the optimization of VRFB system loss. The prediction and optimization of VRFB system losses will influence the development of efficient electrical interfacing of VRFB with renewable energy systems.

Chapter 4

Optimizing Vanadium Redox Flow Battery system power loss under different operating conditions

4.1 Introduction

The modern electricity demands are being catered with the surge in the utility of renewable energy sources (RES) that comprises of solar, wind, biogas, etc. Considering the global perspective, the United Nations Sustainable Development Goal 7 (UNSDG 7) has set a target to "ensure access to affordable, reliable, sustainable and modern energy for all". The UN in its recent global roadmap, "Transforming our world: The 2030 Agenda for sustainable development", have proposed to gradually raise the availability of renewable energy resources to meet the global energy demand by 2030 [118]. The associated technologies and/or solutions contributing to the extensive utilization of RES need to be reliable and optimized. Due to the intermittency of the RES, the energy storage systems (ESS) are considered as a promising option in improving the performance reliability. The use of ESS to store the energy generated by the intermittent renewable energy sources has drawn deep interest in the stationary and mobile applications over last few decades. For RES applications, battery energy storage systems (BESS) have become one of the most acceptable storage solutions for several advantages, such as faster response, relatively higher energy density, etc., compared to the other conventional storage solutions. For large and medium scale stationary renewable energy storage applications, Vanadium Redox Flow Battery (VRFB) is found to be a potential energy storage solution. VRFB exhibits several advantages over other traditional batteries such as Sodium-Sulphide (Na-S), Lead-Acid, Lithium-ion (Li-ion), Nickel-Cadmium (Ni-Cd), etc. The power and energy capacity of VRFB is scalable separately. The VRFB stack size determines its power capacity, while the electrolyte volume determines the energy capacity. The high columbic efficiency, the longest cycle life (>20000) [21], deep discharge capacity, and fast response time are all advantages of VRFB [30], [99], [119]–[123] storage over the other conventional battery storage solutions.

These advancements have made VRFB as the promising choice of BESS for the large-scale energy storage. VRFB has shown promising BESS performance in achieving efficient and reliable operations of renewable energy based microgrids, ranging from peak shaving to

demand response management [94], [122], [124]–[128]. Kerdphol et al. [129] proposed Particle Swarm Optimization (PSO) method based frequency control of the standalone microgrid to obtain optimum sizing of VRFB based BESS at a minimum total BESS cost. Further investigation by Kerdphol et al. [130] proposed an optimum sizing of VRFB-based BESS using PSO incorporating dynamic demand response to mitigate the instability of microgrid during an emergency. Huang and Mu [30] have systematically analysed the challenges of VRFB in microgrid. In their review article, the urgency to operate the VRFB in the best operating state by reducing the VRFB system loss is emphasized, in order to eventually improve the overall performance of the VRFB in microgrid. Xiong et al. [75] predicted the VRFB performance under variable temperature conditions using PSO for parameter identification of their proposed equivalent circuit model. In most of the related works reported so far, VRFB has been used as stationary storage solution, but the system level loss optimization of VRFB has not been addressed. Therefore, it is the need of the hour to look into the VRFB system loss optimization to ensure its reliable operation as a long-term storage facility.

In the operation of a VRFB system, the electrolyte flowrate is a key control variable. It is a fact that VRFB internal loss parameters are majorly controlled by electrolyte flow rate. Low electrolyte flow rate causes less pump power consumption but gives inadequate electrolyte through the channels of stack for the required chemical reaction. However, if the electrolyte flowrate is too high, leakage is possible, and the pump's consumption rises, lowering overall efficiency of VRFB system [96], [98], [110], [131]–[134]. In addition, it is also significant that the VRFB stack internal resistance decreases at higher electrolyte flow rate but increases at low flow rate, thus leading to more power loss inside the battery stack. Therefore, an optimal electrolyte flow rate should be determined in order to minimize the total system loss and/or to maximize the overall VRFB system efficiency. Besides this, the electrolyte in VRFB acts as a coolant also and therefore it needs to be optimized during operation to ensure safe limit of VRFB stack temperature[135] rise due to high charge-discharge currents. Thermal management for VRFB system can be done in this way. Although various electrolyte flow rate optimization (constant flow rate optimization, variable flow rate optimization and dynamic flow rate optimization) has been addressed and demonstrated in the existing literature [100], [136]–[141], the majority of the existing work is limited to the cell-level approach of VRFB. Tossaporn et al. [142] proposed an optimal operational strategy for VRFB to ensure high system efficiency by determining the electrolyte flow rate during the charge-discharge operation. Their model predicted operating battery voltage and pump power consumption for electrochemical model of VRFB to minimize the total charging energy and maximise the total

discharging energy. The validation of model was limited to the experimental data of a single VRFB cell and the work, lacked the investigation of overall VRFB system power losses involved in determining the overall VRFB system efficiency. **Table 4.1** displays the comparison among the methodologies for optimizing the VRFB performance in different aspects adopted in the existing literature and the proposed work. It highly signifies that the proposed work has not yet been addressed by any of the previously reported works.

Table 4.1: Comparison among the methodologies adopted for optimizing VRFB system performances in the existing literature and the proposed work

Literature	**Methodology**	**Optimizing parameter**	**Application**
Ma et al. [136]	Entirely Experimental approach, no optimization algorithm	Electrolyte flow rate of VRFB	Electrolyte flow rate optimization during the charge-discharge process to improve the VRFB system efficiency.
Kim et al.[137]	Empirical equation-based approach	Energy efficiency of VRFB system	An operating strategy in the form of empirical equation proposed for maximizing the energy efficiency of VRFB.
Bhattacharjee et al.[73]	Entirely Experimental approach, no optimization tools	Electrolyte flow rate of VRFB	VRFB internal circuit parameter extraction and recommendation of optimal flow rate
Xiong et al.[75]	Particle Swarm Optimization (PSO)	Error in identifying RC parameters of VRFB equivalent circuit	An Enhanced Equivalent Circuit (RC) Model of VRFB considering thermal Effects
Bhattacharjee et al.[135]	Entirely Experimental approach, no optimization tools	Electrolyte flow rate of VRFB	An efficient VRFB thermal management solution for various charge-discharge scenario.
Li et al.[126]	Power –Efficiency coupling based Mathematical model, no optimization tools	Efficiency of VRFB	An optimal control strategy proposed to improve the efficiency of VRFB in peak shaving

Jirabovornwisut et al. [142]	Non-linear programming	Charging and Discharging energy	An optimal electrolyte flow rate to maximize the discharging energy efficiency.
Kerdphol et al.[130]	Particle Swarm Optimization (PSO)	Sizing of Battery Energy Storage System (BESS)	Dynamic demand response for microgrids considering an optimal sizing of BESS
Proposed work	Particle Swarm Optimization (PSO) and Genetic Algorithm (GA)	VRFB system power loss including stack and pump power losses	Optimization of the VRFB system power loss considering stack power loss and pump power simultaneously, for efficient integration of VRFB storage with renewable energy applications

Considering the above-mentioned scenario and necessity of optimizing the system level VRFB power loss, this chapter proposes a multi-variable optimization strategy that can help the VRFB system to operate with minimum power loss. In this work, a combined optimization of pump power and stack power has been done based on PSO technique under different charge-discharge conditions. Simplicity in execution and fast convergence are some of the major reasons for selecting PSO in this work[143]–[145]. This optimization of VRFB parameters is important in minimizing the overall VRFB system power loss. In this work, a practical 1kW 6h VRFB system operating specifications has been used to validate the proposed optimization. The results obtained in this work claims to be very useful in ensuring efficient operation of VRFB system while interfacing with renewable energy sources, microgrids etc. The rest of the chapter is divided as; Section 4.2, deals with the overall block diagram of the proposed scheme, Section 4.3 represents the mathematical representation of PSO. Section 4.4 describes the results and analysis. Section 4.5 describes the conclusion of the chapter.

4.2 Overall workflow and VRFB System Operation

The overall workflow of this chapter and the operation of VRFB system are depicted in Section 4.2. This Section consists of two subsections. In Subsection 4.2.1, the overall block diagram of the proposed scheme is discussed and Subsection 4.2.2 details the VRFB System operation.

4.2.1 Overall block diagram of the proposed scheme

In this section, the workflow of the proposed VRFB system power loss optimization scheme is discussed; and the section also expresses the criteria involved in the VRFB system power

loss optimization. **Figure 4.1** describes the overall block diagram of the proposed optimization scheme using PSO in which the input variables, control variable and the boundary conditions involved in the PSO optimization is mentioned. Stack current, Terminal voltage, Pump power, VRFB internal resistance and stack temperature are the input variables fed into the optimization of VRFB system loss.

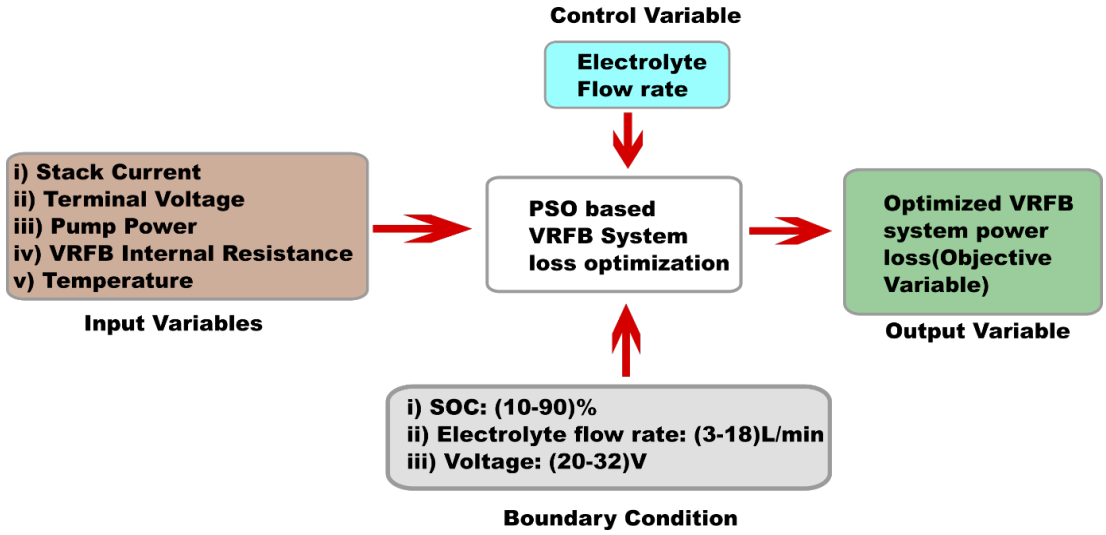

Figure 4.1: Overall block diagram of the proposed scheme

Electrolyte flow rate is utilized as the control variable. PSO based optimization is carried out to optimize the VRFB system loss. The boundary conditions considered in this work includes SOC with the range of 10% to 90%; the electrolyte flow rate is maintained between 3 L/min to 18 L/min; and the operating voltage is maintained between (20-32) V. The performance of input variables in different operating conditions is taken into consideration while designing the boundary conditions of the PSO optimization technique. The optimized VRFB system power loss is the output variable in this work. The optimization of VRFB system power loss is very crucial to improve the overall VRFB system efficiency.

4.2.2 VRFB storage system operation

For the large-scale stationary energy storage applications, VRFB is one of the widely preferred battery storage technologies because of the longevity of the system performance. Realization of the working principle of VRFB system is necessary to further incorporate all the associated parameters involved in the optimization of VRFB system. Therefore, the working principle of VRFB system has been discussed in **Section 2.2** of this thesis. The detailed description on the electrical equivalent modeling of VRFB storage system required for VRFB system power loss calculation has been discussed in **Section 2.2** of this thesis.

4.3 PSO based VRFB system power loss optimization

PSO is a nature inspired optimization technique developed from 'bird flocking' or 'fish schooling' by Kennedy and Eberhart [146], based on the social sharing of information among the conspecifics. In PSO, the concept of social interaction among the conspecifics is used for solving a problem. PSO consists of a number of particles (agents) that constitutes a swarm, moving around in the search space with an objective to obtain the best solution. A particle, x_i, in the population, N, is denoted as, $x_i = (x_{i1}, x_{i2}, \ldots, x_{iD})$, i = 1, 2, …, N. Each particle moves in the search space with the velocity, v_i. The initial population S = $\{x_1, x_2, \ldots, x_N\}$, is randomly generated by a uniform distribution. Each particle in the swarm searches for its positional coordinates in the search space, which are associated by the best solution achieved by that particle so far, known as personal best (P_{best}) and the best possible solution achieved by any particle in the search space, known as global best (G_{best}). **Figure 4.2** displays the generic flow diagram of PSO. The first step in the PSO algorithm is the initialization of the position and velocities of the particles. Once initialization is done, the fitness values of the particles are calculated. From the results of the calculation, the individual optimal solution of the particles is obtained, which eventually helps in obtaining the global optimal solution of the group. From these optimal results, the velocity and position of the particles are updated as given by **Equation (4.1)** and **(4.2)**,

$$v_{i+1} = v_i + c_1 r_1 (P_{best} - x_i) + c_2 r_2 (G_{best} - x_i) \quad (4.1)$$

$$x_{i+1} = v_{i+1} + x_i \quad (4.2)$$

In **Equation (4.1)**, 'c_1' and 'c_2' represents the learning factors. 'r_1' and 'r_2' signifies the random numbers within (0,1]. The selection of the particle number and learning factors are done empirically as per the literatures [75], [147], [148]. The values of the self-learning factor 'c_1', the social learning factor 'c_2' are set between 1 and 2, respectively. It is to be noted that the learning factors have significant effects on the algorithm convergence rate. In this optimization, the learning factors are selected as c_1 = 1.5 and c_2 = 1.6. The inertia weight of the iteration is set at w = 0.5.

In the optimization of VRFB system power loss, the electrolyte flow rate is a critical parameter that influences the VRFB system's efficiency. The electrolyte flow rate is the control variable in the proposed optimization scheme. It is dependent upon the factors such as stack

current 'I_{stack}', state of charge 'SOC', and electrolyte capacity 'N'. The theoretical flow rate 'Q', used in the hydraulic pump model is given by the mathematical expression in **Equation (4.3)** [50], [122],

$$Q = \frac{I_{stack}}{N \times SOC} (m^3/sec.) \quad (4.3)$$

The electrolyte capacity 'N' is expressed by

$$N = n_e \times c \times F \ (A.sec./m^3) \quad (4.4)$$

where, 'n_e' stands for the number of electron transferred per mol, 'c' signifies the Vanadium concentration in the electrolyte (mol/ L) and '*F'* represents Faraday's constant (96485 C/mol).

It is inferred from **Equation (4.3)** that the theoretical flow rate 'Q' varies inversely proportional to the SOC for a constant charging/discharging current 'I_{stack}'. This is the minimum flow rate requirement at which the VRFB charge-discharge operation begins. In the operation of VRFB system, neither the maximum nor the minimum electrolyte flow rate is suitable for maximizing the overall VRFB system efficiency. Therefore, the optimal electrolyte flow rate must lie somewhere between the maximum and minimum flow rates. To find the optimal flow rate, PSO based multi-variable optimization is executed in this chapter with electrolyte flow rate as the control variable. To maximise the VRFB system efficiency, the overall VRFB system power loss needs to be minimized as low as possible. Therefore, in this chapter, the optimization of electrolyte flow rate is performed during the VRFB system operation to minimise the overall VRFB system loss. The objective function for obtaining the overall VFRB system loss is given by **Equation (4.5)** as shown below. The total VRFB system power loss is expressed effectively in terms of electrolyte flow rate (Q) as the flow rate is the control variable in this optimization.

$$P_{loss\,VRFB} = I_s^2 . R_{int}(Q) + P_{pump}(Q) \quad (4.5)$$

subject to the constraints: $min\ P_{loss\,VRFB}(Q) <= P_{loss\,VRFB}(Q) <= \max P_{loss\,VRFB}(Q)$;

$$(Q_{min}) <= (Q) <= (Q_{max})$$

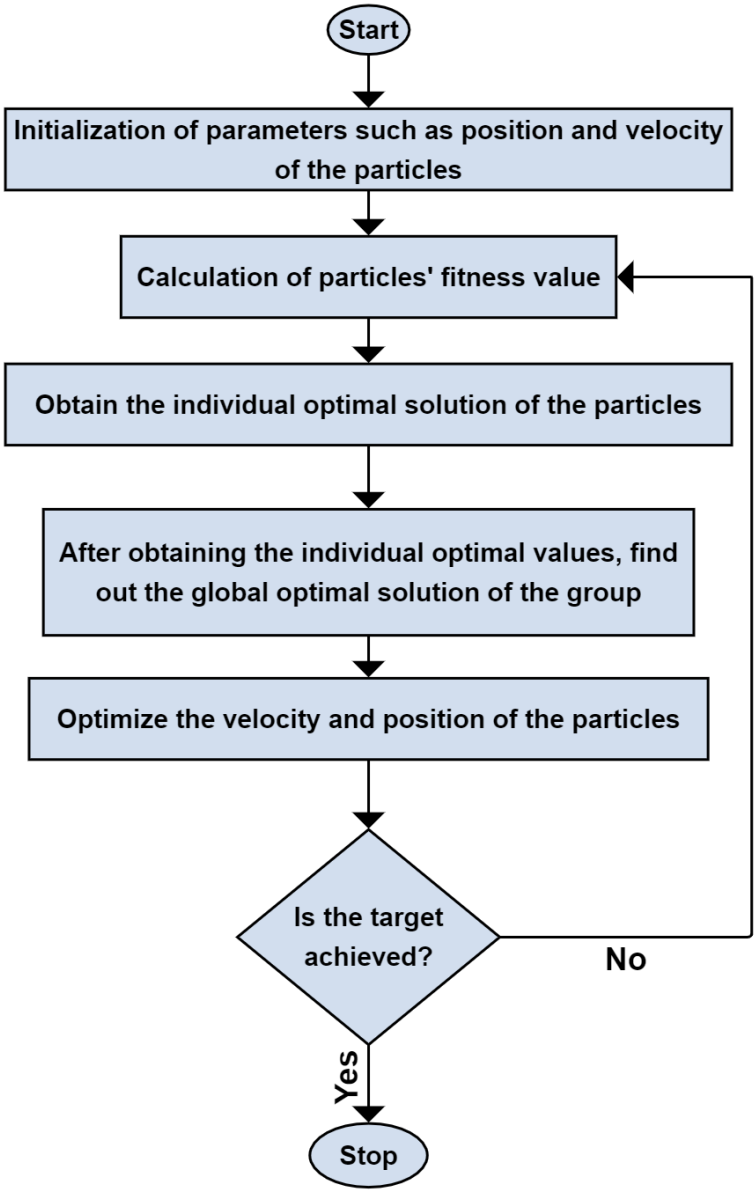

Figure 4.2: Generic flow diagram of PSO algorithm

To solve the objective function expressed in **Equation (4.5),** a framework is proposed based on PSO algorithm in this work**.** The workflow of PSO based optimization is depicted in **Figure 4.3** and the steps involved in the workflow is detailed as follows,

Step 1: Initialization of VRFB system parameters: stack current (I_s), pump power (P_{pump}), internal resistance (R_{int}) and electrolyte flow rate (Q). Assign number of iterations (i) by 'N'. Assign w = 0.5, C_1 = 0.8, C_2 = 0.9.

Step 2: Calculation of VRFB system power loss ($P_{(loss\ VRFB)}$) is expressed by the fitness function, which is a modified version of **Equation (4.6)** with iteration count 'i',

$$P_{(loss\ VRFB),i} = I_{s,i}^2 \times R_{int,i}(Q_i) + P_{pump,i}(Q_i) \quad (4.6)$$

$P_{(loss\ VRFB),i}$ is the power loss value for i[th] particle.

Step 3: Evaluate the fitness function over the electrolyte flow rate range from 3 L/min to 18 L/min. Determine the minimum VRFB system loss at an electrolyte flow rate by obtaining the particles' personal best position.

Step 4: Update the particle's velocities and position to obtain the electrolyte flow rate (Q_{opt}) that gives the minimum VRFB system power loss by finding the global best position and velocity of particles.

Step 5: Check if $P_{(loss\ VRFB),min} <= P_{(loss\ VRFB),i}$. If the result is 'yes', go to step 6. Otherwise, go to step 2.

Step 6: Minimum power loss ($P_{(loss\ VRFB),\ min}$) is obtained at an optimal flow rate (Q_{opt}).

The mathematical equation for obtaining the minimum overall VRFB system power loss using PSO algorithm is given by **Equation (4.7)** as follows,

$$min\ P_{loss\ VRFB}(Q_{opt}) = I_s^2 . R_{int}(Q_{opt}) + P_{pump}(Q_{opt}) \quad (4.7)$$

In **Equation (4.7)**, the VRFB internal resistance (R_{int}) and pump power (P_{pump}) are variable parameters and functions of electrolyte flow rate (Q). The VRFB system power loss optimization is achieved by operating the system at optimal electrolyte flow rate (Q_{opt}). PSO based multi-variable optimization is executed to obtain the optimal electrolyte flow rate (Q_{opt}) by feeding the experimental data of the VRFB system as shown in **Figure 4.3** over the electrolyte flow rate ranging from 3 L/min to 18 L/min.

Further, the overall VRFB system efficiency (η) has a direct relationship with electrolyte flow rate and represented as follows,

$$\eta = \frac{\int_0^{t_d} P_{Discharge}(t)dt}{\int_0^{t_c} P_{Charge}(t)dt} = \frac{\int_0^{t_d} (P_{stack}(Q) - P_{loss\ VRFB}(Q))dt}{\int_0^{t_c} (P_{stack}(Q) + P_{loss\ VRFB}(Q))dt} \quad (4.8)$$

And, the maximum efficiency can be obtained by,

$$\eta_{max} = \frac{\int_0^{t_d}(P_{stack}(Q_{opt}) - P_{loss\,VRFB}(Q_{opt}))dt}{\int_0^{t_c}(P_{stack}(Q_{opt}) + P_{loss\,VRFB}(Q_{opt}))dt} \quad (4.9)$$

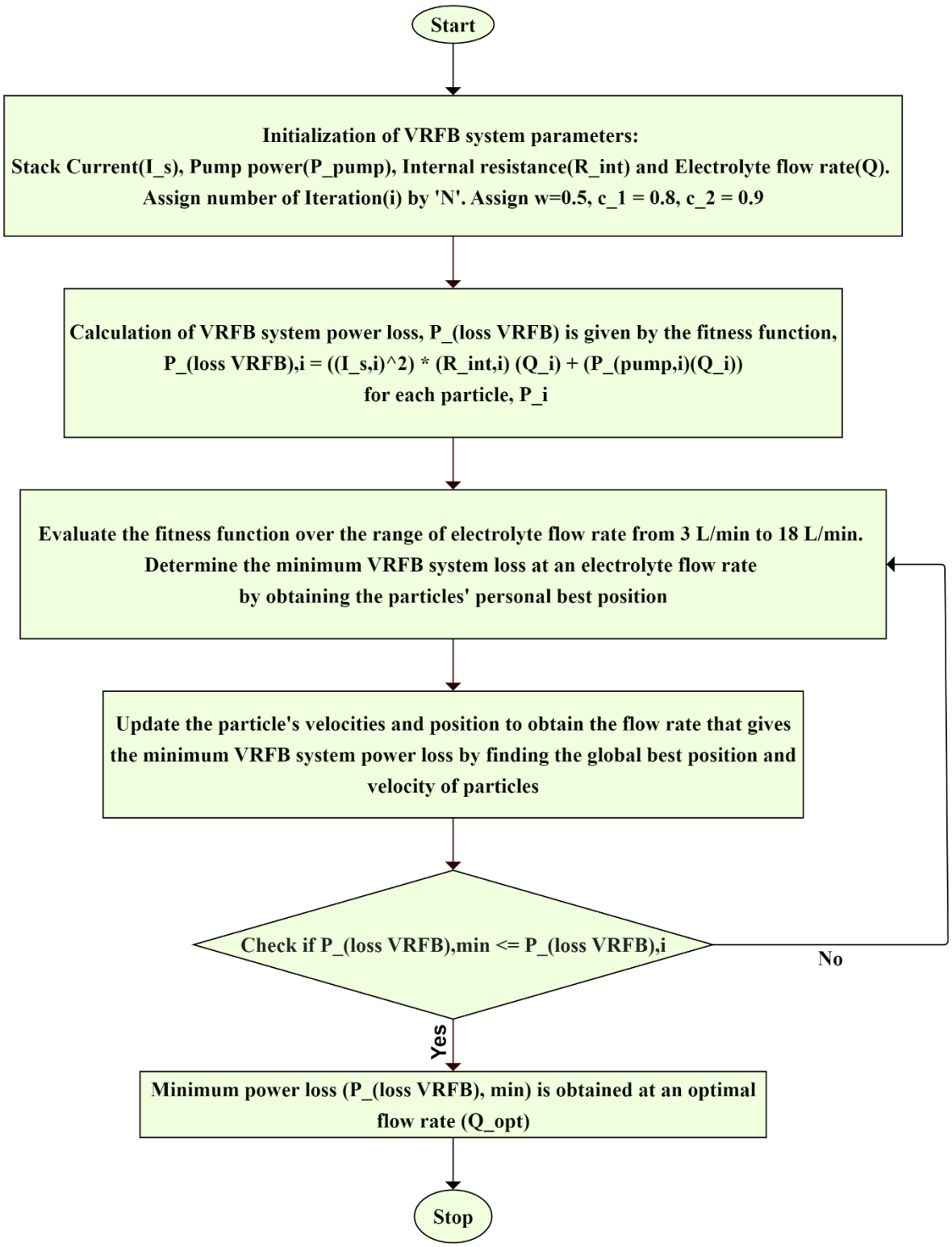

Figure 4.3: Workflow diagram for PSO based optimization of VRFB system power loss

In **Equation (4.8),** 'P_{Charge}' signifies the VRFB system's overall charging power consumption. '$P_{Discharge}$' represents the power delivered by the VRFB system during discharging (W). 'P_{stack}' represents the power consumed and/or delivered by the VRFB stack. 't_d' and 't_c' represent the total discharging and total charging time respectively. '$P_{loss\,VRFB}$' is the VRFB system power loss including both the stack loss and pump power consumption. All these power loss components are function of electrolyte flow rate (Q). It can be inferred from **Equation (4.9)** that the optimal flow rate (Q_{opt}) will ensure the minimum VRFB system loss which means the maximum system efficiency.

4.4 Results and Discussion

For experimental study, data acquisition and computing VRFB system loss, a practical 1kW 6h capacity has been chosen and the system specification is provided in **Table 4.2**.

Table 4.2: VRFB system parameter specifications

VRFB system parameters used for PSO based power loss optimization	**Rating**
Number of series cells (n) in stack	20
Power Capacity	1 kW
Energy Capacity	6 kWh
Dimension of each electrode ($L_{felt} \times W_{felt} \times D_{felt}$)	25 × 25 × 0.3 cm × cm × cm
Volume of tanks	180 L
Electrolyte Concentration	1.2 Mol/L
Voltage Range	(20-32) V
Upper permissible limit of Stack current	60 A
Current density	0.096 A/cm^2
Stack temperature range	15 - 35°C
Electrolyte flow rate safe operating range	(1-18) L/Min

The optimization of overall VRFB system power loss using PSO algorithm has been performed in MATLAB simulation platform. The overall VRFB system power losses are

obtained for four different electrolyte flow rates (3 L/min, 6 L/min, 12 L/min and 18 L/min) within the range specified by the manufacturer. The lower and upper bound limits of VRFB internal resistance and pump power consumption of each electrolyte flow rate for a particular stack current, obtained from the results of 1 kW, 6 kWh VRFB charge-discharge experiments, are set during the initialization of the PSO algorithm. The number of particles, number of iterations and social factors (C_1, C_2) of the PSO algorithm are set for three different values of stack currents (40 A, 45 A and 50 A) and the optimization results from each run are investigated. The simulation is implemented starting with the minimum number of iterations (10 iterations), and the number of iterations is gradually increased to investigate the convergence rate of PSO algorithm. The PSO results obtained for the different iterations (100 iterations, 200 iterations and 300 iterations) for each of the three different stack currents (40 A, 45 A and 50 A) are shown in **Figures 4.4, 4.5 and 4.6**. The convergence rate of PSO algorithm during 100 iterations are observed for different stack currents. The variation in the VRFB system power loss values was observed during the different instances of iterations. It can be observed from **Figure 4.4 (a)** that the overall VRFB system power loss values for the stack current of 40 A converge at the different instances of the iterations. For the electrolyte flow rate of 3 L/min, the overall VRFB system power loss values converge after 30 iterations, whereas for the electrolyte flow rate of 6L/min, 12 L/min and 18 L/min, the overall VRFB system power loss values converge at 40 iterations, 70 iterations and 50 iterations respectively. A similar trend can be observed in **Figures 4.5 and 4.6** for the stack currents of 45 A and 50 A respectively. Furthermore, the number of iterations is increased to 200 and 300 respectively and the convergence rate of the PSO algorithm is observed. It has been found from the PSO algorithm results that the values of overall VRFB system power loss for a stack current of 40 A are converged to its final value after 120 iterations and there is no more variation in the values till 300 iterations as seen in **Figure 4.4 (c)**.

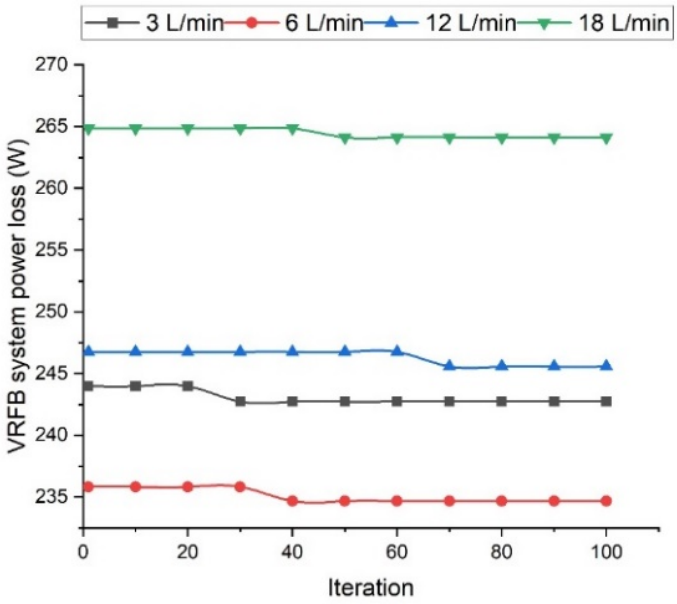
3 L/min
6 L/min
12 L/min
18 L/min
VRFB system power loss (W)
270
265
260
255
250
245
240
235
0
20
40
60
80
100
Iteration

(a)

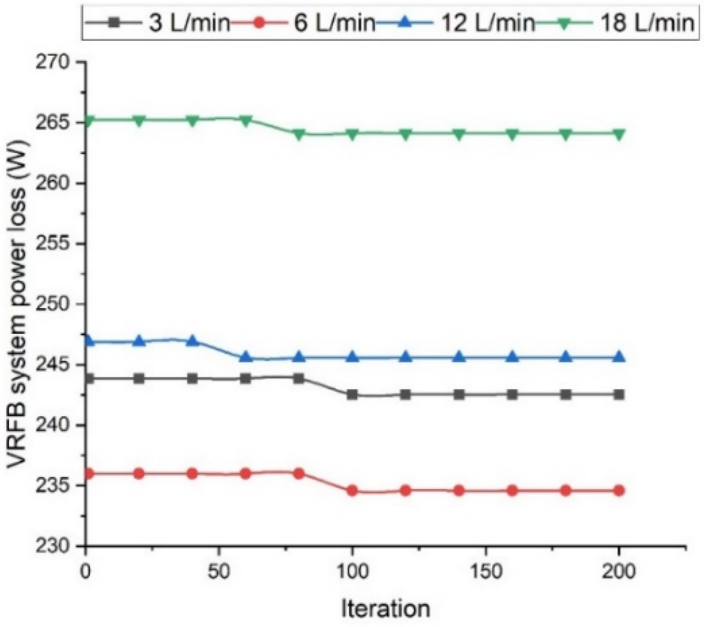
3 L/min
6 L/min
12 L/min
18 L/min
VRFB system power loss (W)
270
265
260
255
250
245
240
235
230
0
50
100
150
200
Iteration

(b)

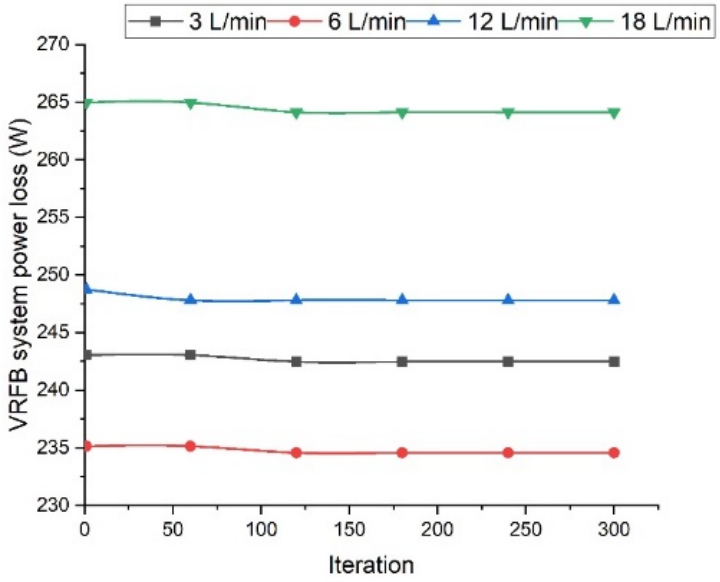

(c)

Figure 4.4: Overall VRFB system power loss for stack current of 40 A obtained from PSO optimization in terms of different iterations; (a) 100 iterations; (b) 200 iterations; (c) 300 iterations

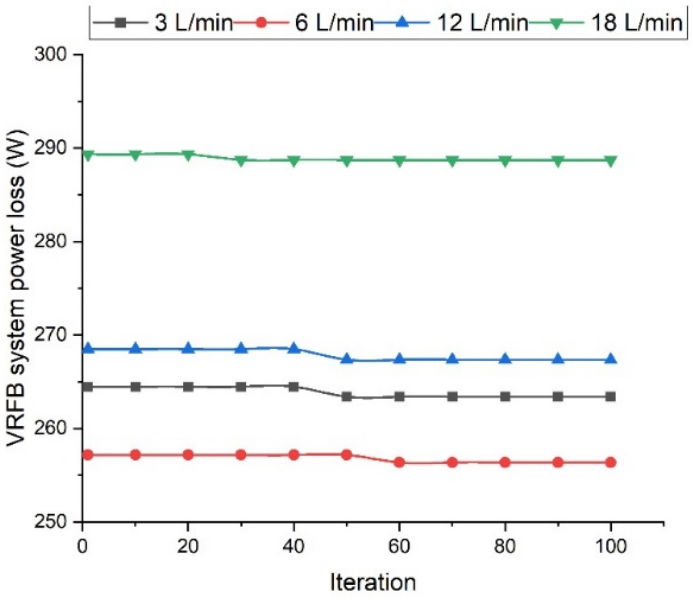

(a)

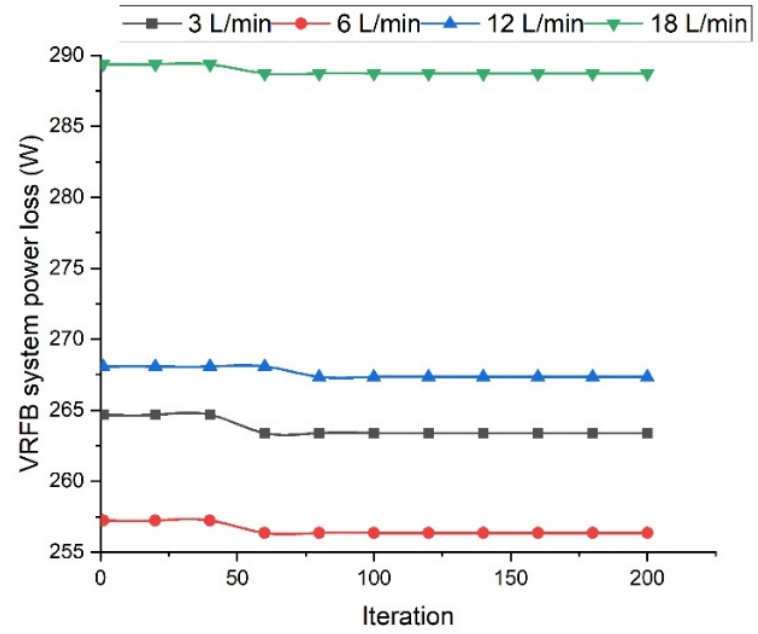

(b)

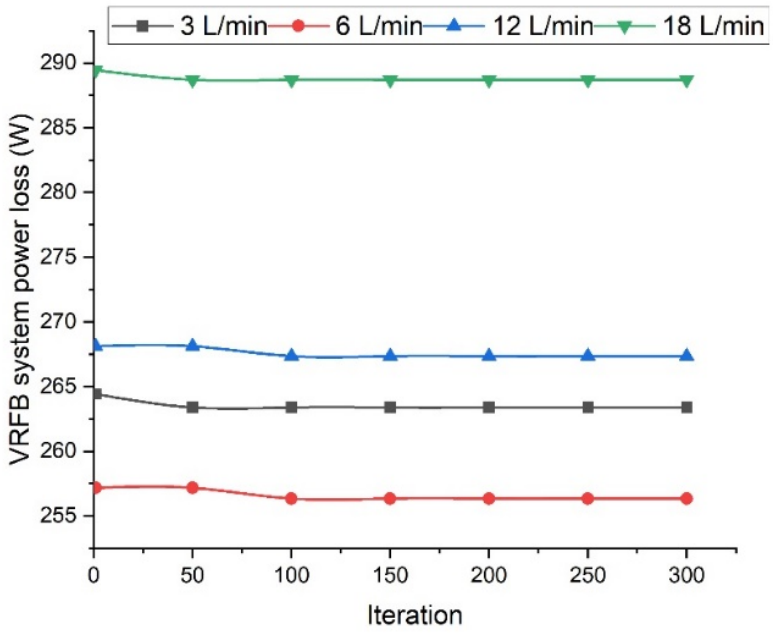

(c)

Figure 4.5: Overall VRFB system power loss for stack current of 45 A obtained from PSO optimization in terms of different iterations; (a) 100 iterations; (b) 200 iterations; (c) 300 iterations

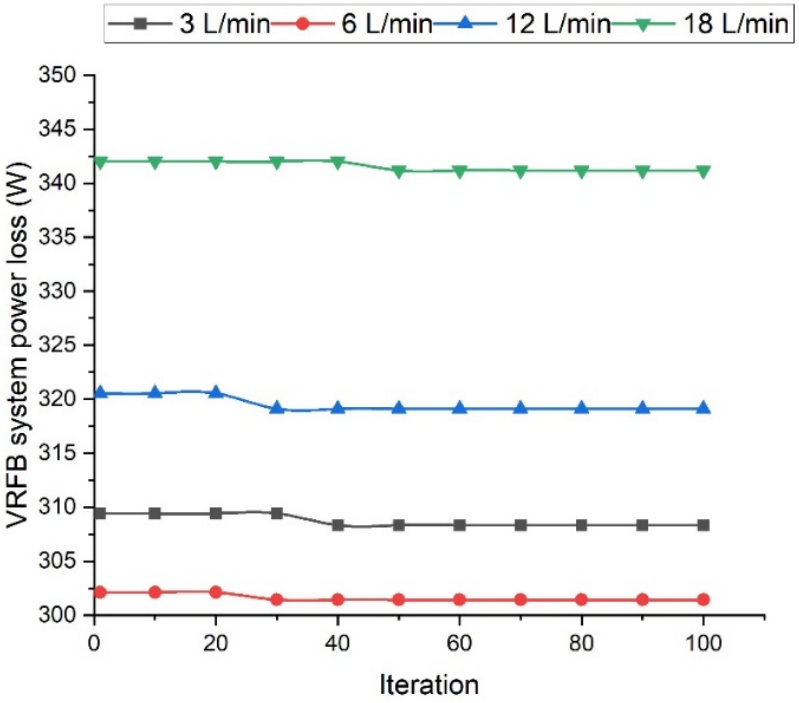
3 L/min
6 L/min
12 L/min
18 L/min
VRFB system power loss (W)
350
345
340
335
330
325
320
315
310
305
300
0
20
40
60
80
100
Iteration

(a)

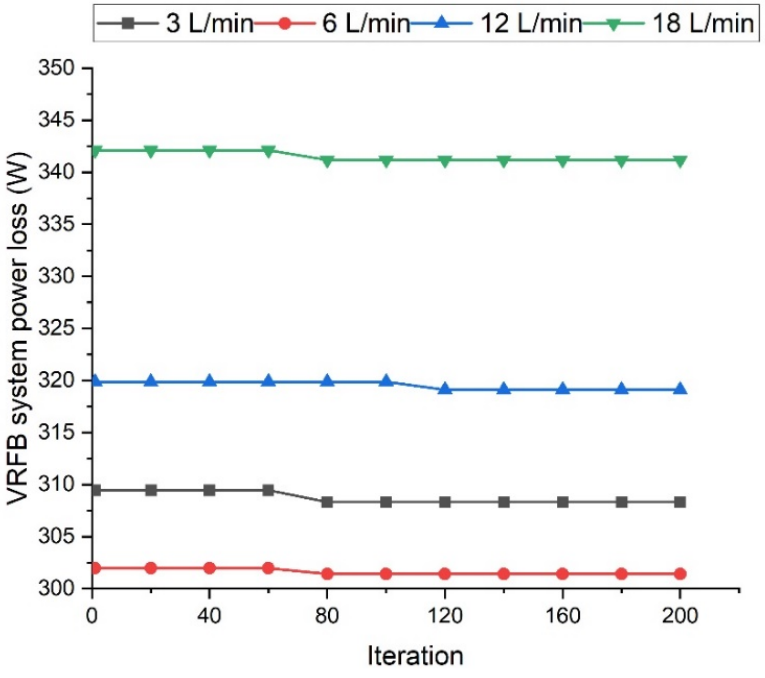
3 L/min
6 L/min
12 L/min
18 L/min
VRFB system power loss (W)
350
345
340
335
330
325
320
315
310
305
300
0
40
80
120
160
200
Iteration

(b)

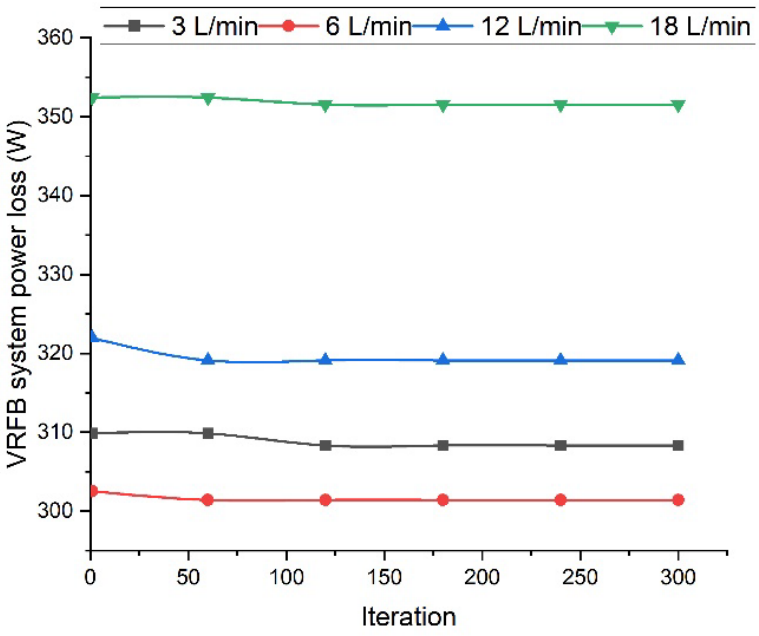

(c)

Figure 4.6: Overall VRFB system power loss for stack current of 50 A obtained from PSO optimization in terms of different iterations; (a) 100 iterations; (b) 200 iterations; (c) 300 iterations

Table 4.3 displays the minimum VRFB system power loss obtained among the four different electrolyte flow rates (3 L/min, 6 L/min, 12 L/min and 18 L/min) for each stack current.

Table 4.3: Optimal electrolyte flow rate and Minimum VRFB system power loss at different stack currents in terms of iteration

Stack current (I_s) in (A)	Number of Particles	Number of Iterations	Electrolyte flow rate(L/min)	Minimum VRFB system power loss(W)	Optimal electrolyte flow rate(L/min)
40	50	100	3	242.725	6
			6	240.080	
			12	247.697	
			18	263.775	
	100	200	3	242.813	6
			6	240.726	
			12	247.807	
			18	264.243	

	150	300	3	243.511	6
			6	240.824	
			12	247.803	
			18	264.348	
45	50	100	3	274.978	6
			6	272.582	
			12	285.714	
			18	299.035	
	100	200	3	276.202	6
			6	272.614	
			12	284.554	
			18	299.201	
	150	300	3	275.557	6
			6	273.402	
			12	285.389	
			18	298.470	
50	50	100	3	308.331	6
			6	301.419	
			12	319.112	
			18	341.183	
	100	200	3	308.241	6
			6	301.397	
			12	319.032	
			18	341.139	
	150	300	3	308.191	6
			6	301.384	
			12	319.011	
			18	341.121	

It is evident from **Table 4.3** that operating the VRFB system at neither the lowest electrolyte flow rate (3L/min) nor the highest electrolyte flow rate (18 L/min) gives the minimum VRFB

system power loss. In order to operate the VRFB system with minimum loss, the operating point is bound to lie in between the range of 3 L/min to 18 L/min. The results obtained from PSO algorithm reveals that the VRFB system power loss is the lowest at the optimal electrolyte flow rate of 6 L/min (in between the range of minimum and maximum electrolyte flow rates) for 1 kW, 6 kWh VRFB system. The PSO results obtained for the different values of stack currents (40 A, 45 A and 50 A) also validates that the optimal electrolyte flow rate for 1 kW, 6 kWh VRFB system is found to be 6 L/min. **Table 4.4** displays the PSO based overall VRFB system power loss results obtained over the SOC ranging from 0.1 to 0.9.

Table 4.4: Overall VRFB system power loss obtained over the range of SOC from 0.1 to 0.9 for different stack currents

Stack Current (I_s)	**SOC**	**Overall VRFB system power loss (W)**				**Optimal electrolyte flow rate**
		3 L/min	**6 L/min**	**12 L/min**	**18 L/min**	
40 A	0.1	339.384	331.236	341.908	360.324	6 L/min
	0.2	320.976	313.169	320.487	338.984	6 L/min
	0.3	308.257	301.993	310.429	329.785	6 L/min
	0.4	296.127	289.043	299.863	318.684	6 L/min
	0.5	284.206	277.874	288.635	309.254	6 L/min
	0.6	273.126	267.053	277.607	296.369	6 L/min
	0.7	263.517	256.145	267.636	286.521	6 L/min
	0.8	254.999	246.705	258.569	277.854	6 L/min
	0.9	242.474	234.569	245.537	264.124	6 L/min
45 A	0.1	384.568	378.625	387.534	404.684	6 L/min
	0.2	365.361	359.841	366.921	385.645	6 L/min
	0.3	348.362	341.861	348.557	366.775	6 L/min

	0.4	338.697	333.631	342.579	361.367	6 L/min
	0.5	321.582	316.112	325.683	342.964	6 L/min
	0.6	311.361	306.573	316.816	334.297	6 L/min
	0.7	296.315	291.574	300.412	318.672	6 L/min
	0.8	292.578	286.624	295.498	311.051	6 L/min
	0.9	263.384	256.352	267.347	288.711	6 L/min
50 A	0.1	429.331	421.418	432.397	454.224	6 L/min
	0.2	405.456	398.293	415.847	436.965	6 L/min
	0.3	390.581	384.168	401.297	421.962	6 L/min
	0.4	375.706	369.043	388.747	411.06	6 L/min
	0.5	362.831	355.918	373.197	392.886	6 L/min
	0.6	347.956	341.793	358.647	381.878	6 L/min
	0.7	337.081	328.668	345.097	368.263	6 L/min
	0.8	322.206	315.543	338.001	358.009	6 L/min
	0.9	308.331	301.418	319.112	341.183	6 L/min

The optimal electrolyte flow rate obtained in this chapter over the range of SOC is helpful in operating the VRFB system with minimum loss. **Table 4.4** displays the overall system power loss obtained for four different electrolyte flow rates over three different stack currents. As a case study, it can be noticed from **Table 4.4** that for the stack current of 50 A, at 0.6 SOC, the minimum VRFB system power loss is found at 6 L/min, with a magnitude of 341.793 W, whereas at the same 0.6 SOC, for 3 L/min flow rate the VRFB system power loss is found to be 347.956 W. Therefore, operating the VRFB system at an optimal electrolyte flow rate of 6 L/min results in reduction of system power loss by 6.163 W. This will lead to significant energy

loss reduction over a period of VRFB operation. Though the pump power consumption for 3 L/min is the least among all the four flow rates, the overall VRFB system loss becomes higher for 3L/min compared to that of 6 L/min flow rate. In addition to the pump power loss, the variation of VRFB stack internal resistance is a crucial parameter to be considered during the minimization of VRFB system power loss. Thus, the trade-off is needed between the VRFB internal resistance and pump power consumption to optimize the VRFB system operation with minimum power loss. The significance of PSO based multi-variable optimization lies in obtaining the optimal operating point of VRFB system under different operating conditions.

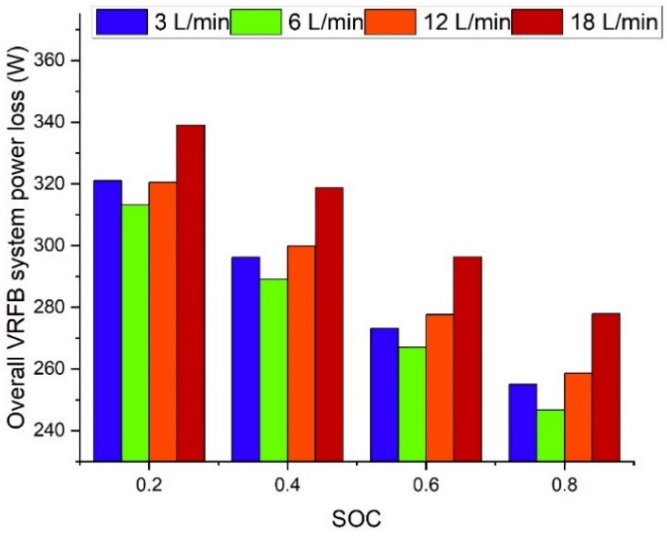

(a)

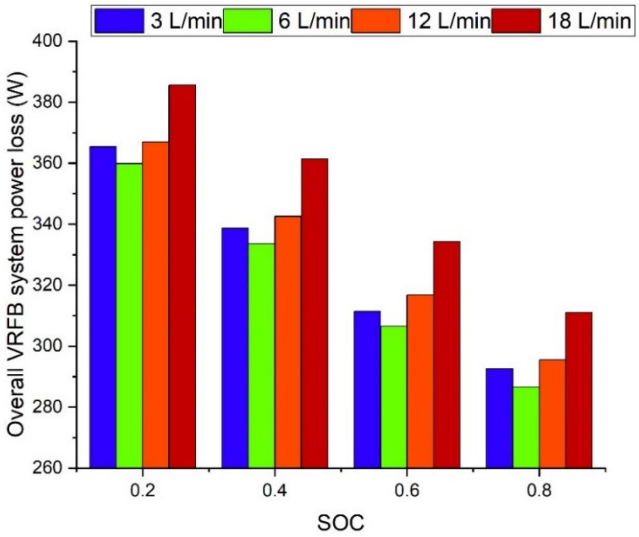

(b)

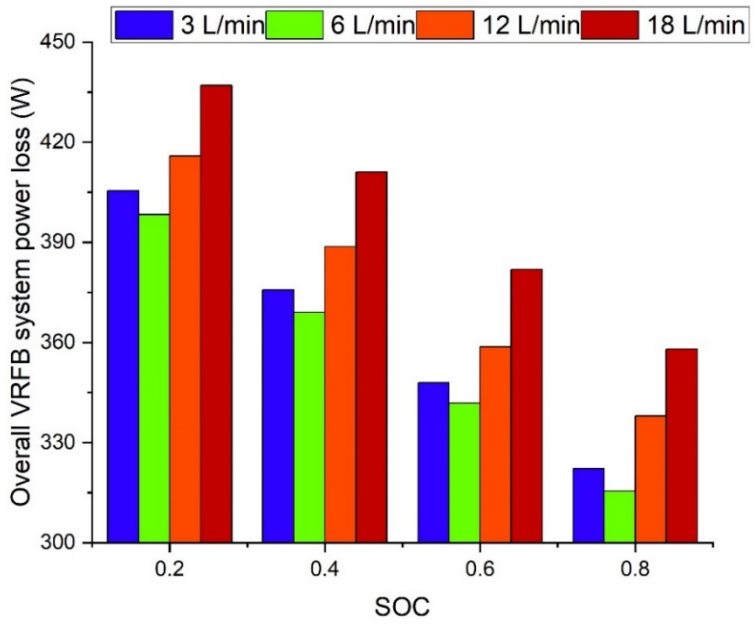

(c)

Figure 4.7: Overall VRFB system loss obtained over the SOC range of 0.1 to 0.9 for different stack currents, (a) 40 A; (b) 45 A; (c) 50 A

The reason for choosing PSO among several other optimization algorithms is analyzed in section 4.5.

4.5 Comparison between different optimization techniques

The comparison between the optimization results obtained from PSO, Genetic Algorithm (GA) and Nonlinear programming is shown in **Table 4.5**. The performance of different optimization techniques while obtaining optimal flow rate for a stack current of 50 A in 1 kW, 6 hr VRFB system over 300 iterations has been compared in **Table 4.5**. It can be observed that GA has lower number of iterations (170 iterations) for convergence in comparison with Nonlinear programming whose convergence is attained after 238 iterations. Eventually GA has a faster computational time of 77 seconds in comparison with traditional Nonlinear programming. Whereas results obtained from PSO optimization technique were better than GA with the faster convergence of 130 iterations and computational time of 43s. Faster convergence and faster execution were the reasons for selecting PSO technique in this work. In addition to faster convergence and time, the superiority of Particle Swarm Optimization (PSO) as compared to Genetic Algorithm (GA) for the 1 kW, 6 kWh VRFB system power loss optimization based on the following reasons,

- Continuous Search Space Efficiency: PSO tends to perform well on continuous optimization problems where the search space is smooth and lacks discrete regions. Its ability to quickly converge towards optimal solutions can be advantageous in such scenario [149].
- Fewer Parameters to Tune: PSO typically has fewer parameters to tune compared to GA. This can simplify the optimization process and reduce the risk of suboptimal performance due to parameter setting [150].
- Simple Implementation: PSO is relatively easy to implement and understand. It doesn't require intricate genetic operators like crossover and mutation, which can sometimes be challenging to fine-tune in GA [151].
- Global Convergence: PSO can have a stronger capability for global convergence in some cases. Due to its swarm-based nature, particles can effectively explore the solution space and find global optima [152].

Therefore, the global optimal solution obtained from PSO technique is better in comparison to optimization results obtained from Nonlinear programming approach and GA.

Table 4.5: Comparison between average convergence and computational time of Nonlinear programming, GA and PSO

Comparison parameters	**Nonlinear Programming**	**GA**	**PSO**
Convergence (Number of Iterations)	238	170	130
Computational time (seconds)	109	77	43

4.6 Conclusion

The key research findings and contributions of this chapter are detailed in this section. The optimization of a kW scale VRFB storage system power loss based on PSO technique has been demonstrated. It is a multi-variable optimization that considers both the VRFB pump power loss and stack power loss simultaneously to determine the optimal flow rate at which the VRFB system power loss becomes the minimum. It has been observed that for 1kW 6kWh VRFB storage system, the overall system power loss becomes the minimum at an optimal flow rate of 6 L/min for a range of 3-18 L/min of flow rate at 40A, 45A and 50A charge-discharge operations. The VRFB system power loss has been reduced by around 2% for each SOC level while operating at the optimal flow rate. The optimization results obtained from PSO technique

have been compared with Nonlinear programming, and GA. The global optimal solution obtained from PSO technique is better in comparison to optimization results obtained from Nonlinear programming approach and GA. For large scale VRFB storage applications, this loss reduction will have a significant contribution to the improvement of its overall system efficiency during operation. The proposed work formulation demonstrated in this chapter is a generalized one and can be very useful for achieving the maximum overall system efficiency of scalable VRFB storage and thus ensuring improved performance of VRFB while integrated with renewable and other power system applications. The requirement for grid-scale battery energy storage systems is increasing rapidly due to the factors such as the inherent demand for power quality, unstable grid frequency etc. because of the growing penetration of renewable energy sources into the grid, and energy security. Therefore, this work indicates the future scope of implementing other efficient optimization algorithms for improving further accuracy in optimizing the system performance, thereby promoting the utility scale VRFB storage integration with renewable energy applications.

Chapter 5

IoT-based smart energy management for solar – VRFB powered switchable building glazing satisfying the HVAC system of EVCS

5.1 Introduction

The electrical interfacing of long-life energy storage with renewable energy sources has become a promising solution to address the energy security and demand response management. VRFB claims to be one of the most suitable energy storage technologies for stationary solar PV applications because of its unique feature of scalability and the longest cycle life compared to other conventional batteries. In the present era, with a focus on sustainable development, clean energy source integrated solutions are getting deep interest. The sustainable transportation and zero-energy building are one of the prime focus areas towards the UN sustainable development goal 7 (UNSDG 7). The building and transportation sectors are the key consumers of electrical energy worldwide, resulting in significant emissions of greenhouse gases (GHG), with carbon dioxide (CO_2) being the primary contributor. Lamb et al.[153] tracked the global GHG emissions from these sectors from 1990 to 2018. In 2018, the building sector and the transportation sector accounted for 6% and 14% of total GHG emissions respectively. The building consumes energy due to the use of Heating Ventilation and Air Conditioning (HVAC) loads as building envelopes which includes wall, door, floor, roof and window are not energy efficient. Among them, building windows play a significant role as it maintains the relation between external and internal ambient. However, traditional windows are not able to limit the solar heat entering into the room and also not capable of stopping the stored heat flow towards external ambient. Replacement of these conventional windows with an advanced window; named as glazing window [154], can reduce the net energy demand.

Current research on advanced building glazing window systems mainly emphasizes two objectives: control of solar heat gain in tropical regions [155]–[157]; control of low heat loss in cold-dominated climates [158]–[160]. In tropical regions, where the climate is warm most of the year, it is necessary to utilize windows that can switch from transparent to opaque. This changeover process reduces solar heat gain and helps to control glare. These building glazing window systems provide daylight and effective control of solar heat gain. An electrically activated smart switching window, also known as an electrochromic window, operates based

on the principle of electrochromism. The electrochromism refers to the phenomenon where a material changes its color or opacity when voltage is applied across it. The primary working principle of an electrically activated smart switching window involves the use of electrochromic materials. A small power supply is required to activate the electrochromic materials used in the smart glazing windows. The electrically activated smart switching window operates by controlling the movement of ions within an electrochromic material through the application of an electric voltage. This enables the window to change its opacity or color, offering control over light and heat transmission in a dynamic and energy-efficient manner. Electrically activated smart switchable building glazing helps to achieve low or less energy-hungry buildings [161]–[164]. However, as this window consumes some electrical power, its large-scale deployment may enhance the building switching load.

Besides, Electric Vehicles (EVs) are becoming one of the rapidly growing technologies towards the drive to attain sustainable energy goals. Despite an increase in the number of EVs on the road, there is still a lack of sophisticated charging infrastructure, and often-lengthy charging times restrict EV utility to short-distance journeys [165], [166]. For the successful implementation of EV expansion, it is indispensable to deploy a large number optimized of EV charging stations. The first step in promoting electric vehicle charging station installation is through the faster allocation of a suitable location for setting up the EV charging station. The EV charging station infrastructure needs much improvement in developing countries where the grid is unstable in semi-urban and/or rural areas. Solar PV powered EV charging stations are becoming one of the viable solutions towards promotion of clean and sustainable transportation infrastructure. For the EV charging station control rooms, the passive HVAC system can be satisfied with the help of glazing windows during daytime. To ensure reliable power supply for the electrically activated glazing windows, along-with the solar power, a long-life energy storge solution is necessary.

In this context, Vanadium Redox Flow Battery (VRFB) is getting prominence nowadays over the traditional batteries such as Lead-Acid, Lithium-Ion (Li-ion), etc. [119], [167]–[170]. The longest cycle life (>20000) [21], [87] among other batteries, scalability of power and energy capacity, deep discharge capacity, safe operation due to exposed structure and quick response time are all advantages of VRFB storage [97], [171]. Because of the utilization of electrolytes as a built-in coolant, the need for a separate heat dissipation chamber is avoided. This reduces the auxiliary thermal management cost compared to that of the Li-ion batteries [135], [169], [172]–[175]. These features of VRFB make it a promising choice for utilization

in EV charging stations as a long-life energy storage. Zhang et al. [176] proposed the optimal sizing of VRFB storage for residential applications, thereby enhancing the penetration of solar PV sources and renewable energy to meet the building energy demand. Innovative energy storage approaches such as gravity energy storage systems driven by solar PV and VRFB storage were proposed recently by Mondal et al. [177] for an energy-efficient multi-storied building. This increasing trend of utilizing long-life VRFB storage for an energy-efficient building improves the reliability of renewable energy penetration in satisfying the building energy demand.

EV charging station infrastructure needs supervisory control and data acquisition (SCADA) and delicate electronic panels. In the countries like India, where the ambient temperature is towards the higher side most of the year, the delicate electronic panels and sensor systems in the control room of EV charging stations require HVAC system to ensure the proper functioning of the equipment [178]. This in return leads to additional consumption of electrical power. According to ASHRAE standard 55-2017 [179], the recommended temperature range for electronic panels in control rooms is between 68°F and 77°F (20°C and 25°C), with a maximum deviation of ±3°F (±1.7°C).

In this regard, Moya et al. [180] proposed an optimal energy management strategy in a smart building with energy storage systems and an electric vehicle charging station, whereas the strategy to save energy consumption and thermal comfort of control rooms of EV charging stations was not addressed in the work. Mazzeo [181] proposed solar and wind-assisted heat pumps to meet the building air conditioning and electric energy demand in the presence of an EV charging station and battery storage. However, the authors did not emphasize the strategy to save the electrical energy demand of EV charging stations. Bianco et al. [182] proposed a building management system for optimal temperature control in the control room of EV charging station. The results obtained in the aforesaid said work emphasized the further scope of minimizing the energy consumption of control rooms of EV charging stations.

To reduce the additional grid-electricity consumption of the HVAC system, a suitable energy-saving solution is required. Considering the necessity, in this work, a smart switchable glazing window powered by solar-VRFB storage for the control room of EV charging station building has been proposed. This technology serves the purpose of temperature compensation inside the control room, by controlling the solar heat gain during the daytime. The switchable glazing window automatically adjusts the amount of light entering the control room and

improves the overall thermal comfort and productivity of the control room by providing natural light and reducing glare. This is also applicable to any large-scale building where traditional windows will be replaced by smart switchable windows. To ensure the uninterrupted operation of glazing windows, an optimized interfacing of solar-VRFB with intelligent demand management system has been proposed. **Figure 5.1** displays the overall schematic representation of the proposed work.

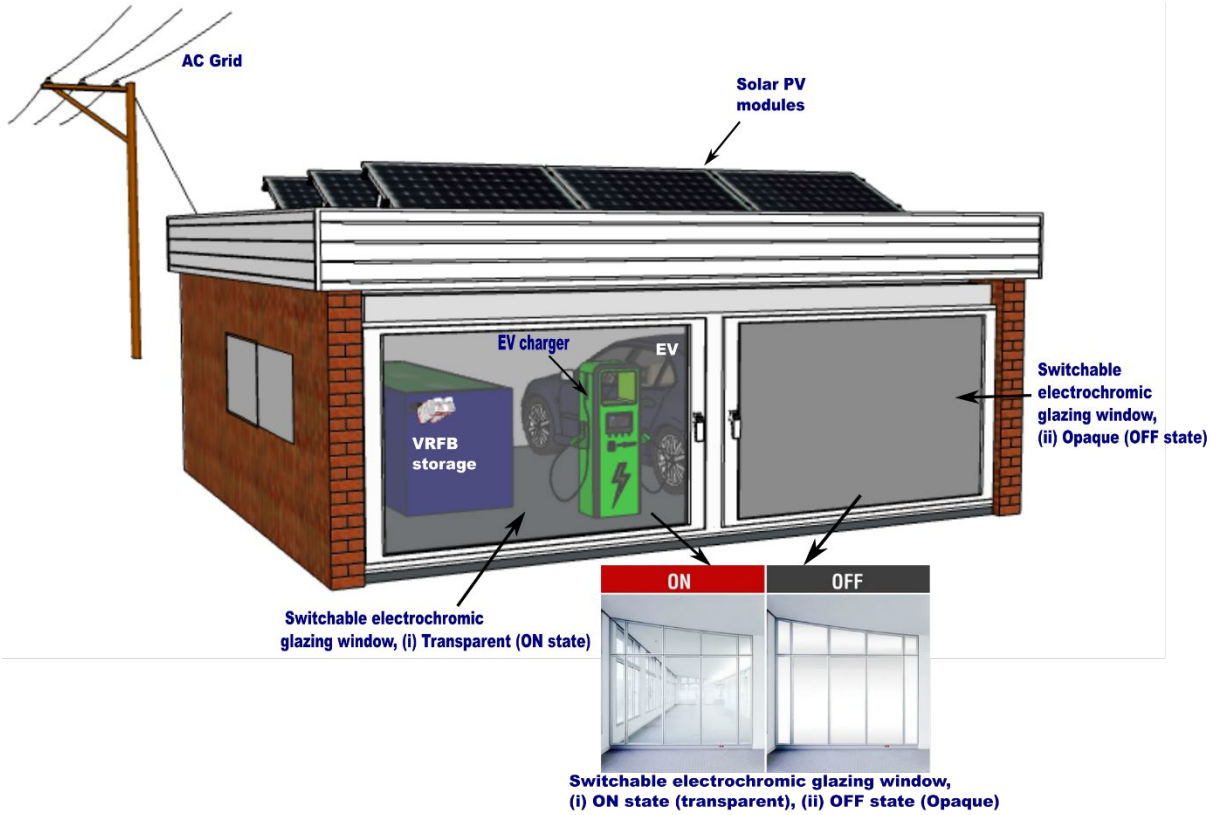

Figure 5.1: Overall schematic representation of the proposed work

The electrically activated switchable electrochromic glazing window has been utilized in the control room of EV charging station. The advantage of the electrically activated switchable electrochromic glazing window lies in its ability to switch from a transparent state (OFF) to an opaque state (ON). The EV charging station with a solar PV source installed on its roof-top to promote green energy and sustainable transportation. Vanadium redox flow battery (VRFB) has been integrated with the system to ensure energy security as a long-life energy storage solution. The integrated system is connected to the distribution grid with a provision of power import/export. A smart energy management system is required to satisfy the building glazing load power demand under real-time dynamic environmental conditions. Therefore, an Internet of Things (IoT) based smart scheduling of solar PV, VRFB storage and the local distribution

grid has been demonstrated for supplying the smart building glazing power demand. For this purpose, in this chapter, a kW scale VRFB storage system is integrated with a smart building glazing energy management system in an EV charging station for efficient operation and low running cost. The performance of the proposed system has been validated under four different transient scenarios; sunny, intermittent cloudy, prolonged cloudy and low solar irradiance with frequent grid outages.

The rest of the chapter is divided as follows: Section 5.2 deals with the representation of the proposed system; Section 5.3 describes the realization of the proposed system; Section 5.4 represents the workflow of the proposed smart building glazing energy management; Section 5.5 details the results and analysis which also discusses the practical case studies, and Section 5.6 summarizes the conclusion of the chapter.

5.2 Representation of the proposed system

In this section, the flow diagram representation of the proposed system is discussed. The proposed system consists of three power sources: solar PV source, VRFB storage, and distribution grid. These power sources supply the building glazing load demand of EV charging stations through smart energy management algorithms. All three input power sources are connected to an intelligent central controller, which controls and executes the power scheduling of the proposed system depending on the availability of the resources, considering the different operating weather conditions. All these power sources are connected to the central controller through communication lines. These power sources receive triggering pulses from the central controller, which communicates the power source to supply power to allocate the building glazing load demand in accordance with the varying weather conditions. In addition to the communication lines, all three power sources are connected to the building glazing load via the power line, as shown in **Figure 5.2**.

The building glazing load and central controller are connected by a bidirectional communication line which is essential in scheduling the supply of power available from different power sources to satisfy the building glazing load demand. Section 5.2 is further divided into subsections 5.2.1, 5.2.2 and 5.2.3. Subsection 5.2.1 discusses the solar PV source which is the predominant source of input power supply in the proposed system topology; subsection 5.2.2 details the switchable building glazing load in EV charging stations; subsection 5.2.3 discusses the VRFB storage, which is a reliable storage option and also

improvises the longevity of energy efficient power supply to fulfil the switchable building glazing window load demand of EV charging station.

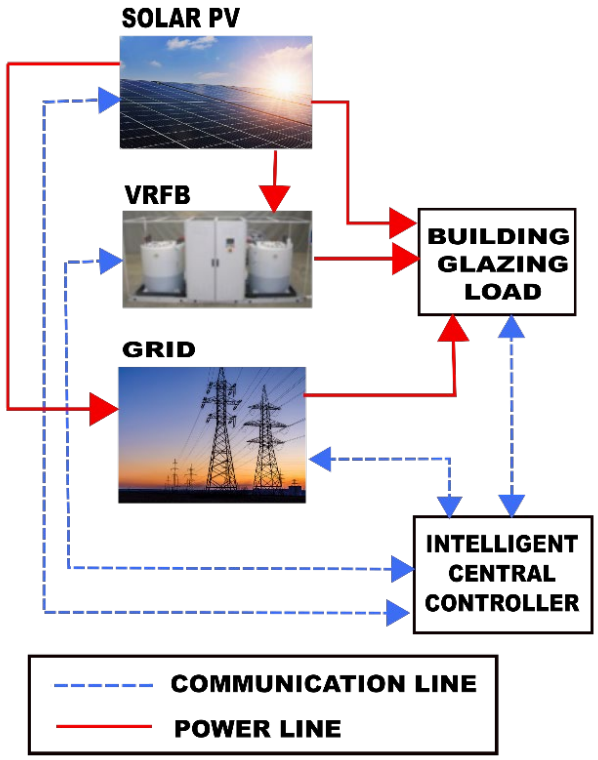

Figure 5.2: Pictorial representation of the flow of the proposed system

5.2.1 Solar PV source

A solar PV power source is a DC power generating array or set of arrays of PV cells. Several PV cells are arranged in series or parallel connection to form a PV system comprising interconnected modules. In order to supply the load, modules are connected to form arrays because a single module cannot produce enough power for all practical uses. PV electricity is a relatively steady renewable energy source that has the highest priority of all renewable energy sources.

DC power output from a solar PV system 'P_{pv}' is expressed by **Equation (5.1)** as follows,

$$P_{pv} = I_{\text{pv}} * \eta_{pv} * A_{pv} \tag{5.1}$$

Where, 'I_{pv}' = Incident effective irradiance (W/m^2),

'η_{pv}' = Efficiency of solar PV module,

'A_{pv}' = Effective surface area of solar PV module (m^2).

5.2.2 Switchable glazing based smart window

The switchable smart windows can be categorized into two types majorly: electrically and non-electrically actuated smart windows. The electrically actuated switchable building glazing windows consist of electrochromic (EC), liquid crystal (PDLC) and suspended particle device (SPD) switchable building glazing systems [183], [184]. The non-electrically actuated switchable building glazing windows comprised of thermochromic, thermotropic and gasochromic building glazing systems [185]–[187]. The building glazing systems need to emit low heat loss for cold-dominated climatic regions. This can be realized in two ways: (i) using aerogels or multiple glass panes to subdue the convection in the air between the exterior panes; (ii) to vanquish the convective heat transfer by introducing an inert gas or vacuum between the panes. Non-electrically actuated glazing windows possess no control over transmission state changes, whereas electrically activated building glazing has the potential to maintain any intermediate state between opaque and transparent state. For this study, an electrically activated smart switchable window has been selected. EC has been considered among the three EC, SPD, and PDLC because of its matching property with PV. The EC needs the power to become opaque and stop the solar heat. Also, at high operating temperatures, its voltage retirement is low. On the other hand, PV also works with lower efficiency at higher temperatures. **Figure 5.3 (a)** shows the switching state of switchable building glazing. **Figure 5.3 (b)** represents the electrical equivalent circuit of glazing, where the R_{eg} represents the equivalent series resistance, C_{dlg} represents the double layer capacitance, R_{ctg} represents the charge transfer resistance and W_o is the Warburg impedance.

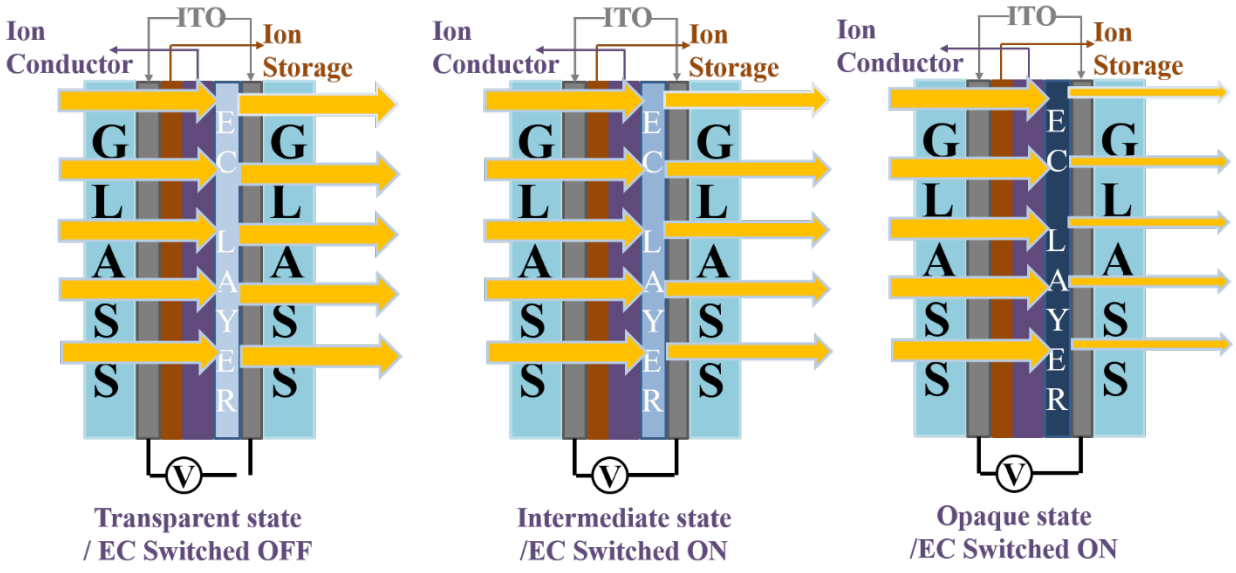

(a)

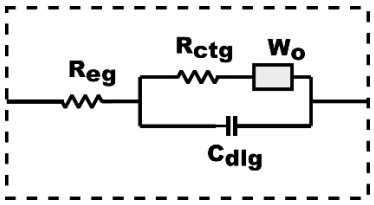

(b)

Figure 5.3: (a) Different switching states of switchable building glazing, (b) Electrical equivalent circuit of glazing

These equivalent internal circuit parameters vary with switching transients and glazing actions. This equivalent circuit is useful for designing the electrical interface system with the external source. Typically, 1 m^2 surface area of glazing glass consumes 5W of electrical power for activation.

5.2.3 VRFB storage

One of the primary reasons for choosing VRFB as the battery energy storage system (BESS) in the proposed system is the versatility offered by VRFB during the designing of the overall storage system. There is flexibility in utilizing VRFB, which offers the variation of the VRFB system scale in the future through the modification of power capacity and energy capacity separately. In VRFBs, the power rating (kW) of the storage system can be modified by varying the stack size, and the energy capacity (kWh) of the storage system can be tuned by varying the volume of electrolyte. Referring to **Figure 2.2 (a)** provided in chapter 2, the dynamic electrical equivalent circuit of VRFB storage is represented. The charge-discharge characteristics of the VRFB stack can be expressed mathematically by stack terminal voltage 'E_t' [50], [73]. In order to compute 'E_t', it is important to determine the open circuit voltage of the VRFB stack. 'E_{OCV}' is the stack open circuit voltage and it is expressed by the modified Nernst potential equation considering the self-discharge drop due to diffusion of vanadium ions through the membrane even under ideal or open circuit condition.

The VRFB stack open circuit voltage 'E_{OCV}' is expressed by **Equation (5.2)**,

$$E_{OCV} = n \times \left\{ E_{Cell\_eq} + \frac{2RT}{F} ln\left(\frac{SOC}{1-SOC}\right) - I_d R_{SD} \right\} \quad (5.2)$$

Where 'n' = Number of series cells in the stack,

'E_{Cell_eq}' = Equilibrium potential of VRFB cell at 50% State of Charge (SOC),

'R' = Universal gas constant (8.314 J),

'T' = Ambient temperature (K),

'F' = Faraday's constant (96485 C/mol),

'I_d' = Diffusion current (A),

'R_{SD}' = Equivalent resistance representing self-discharge potential drop under the idle/open circuit condition of VRFB when the pump is also not operational. The stack terminal voltage 'E_t' is represented by **Equation (5.3)**,

$$E_t = E_{OCV} \pm \{n \times (I_s \times R_{int}(Q, I_s, T))\} \quad (5.3)$$

Where 'E_{OCV}' = Stack open circuit voltage (V),

'I_s' = VRFB Stack terminal current (A),

'R_{int}' = Internal Resistance of VRFB stack (mΩ),

'Q' = Electrolyte flow rate (L/min),

'T' = Operating Temperature (K).

In **Equation (5.3),** the '+' sign signifies the charging and '−' sign signifies discharging condition. 'R_{int}' is a function of electrolyte flow rate (Q), stack current (I_s) and operating temperature (T).

The models of sub-systems described in subsections 5.2.1, 5.2.2 and 5.2.3 of this chapter have been validated by the field results reported by the authors in their previous works [44, 46] and [6, 45]. The development and validation of real time electrolyte flow control integrated solar PV-VRFB charge controller has been reported by A Bhattacharjee et al. [61]. Powering the switchable building glazing load from solar PV, has been validated by A Ghosh et al. [159], [188]. The IoT based smart communication in energy management of VRFB storage integrated bio-solar microgrid has been developed and field validated results are reported by A Bhattacharjee et al. [124]. Hence it can be inferred from the above-mentioned evidence that the results obtained from this proposed integrated smart Solar-VRFB– Building Glazing system will have high accuracy.

5.3 Realization of the proposed system

In this section, the realization of the proposed work is described. Section 5.3.1 describes the demonstration of the proposed IoT-based smart communication system. Section 5.3.2 discusses the design and implementation of the electrical interface of the proposed system.

5.3.1 IoT based smart communication scheme

The proposed energy management system has been monitored and controlled in real-time using the Raspberry-Pi communication platform with MODBUS over TCP/IP platform link. The main server has been set up for monitoring and control. As shown in **Figure 5.4 (a)**, smart energy management is achieved by establishing Internet of Things (IoT)-based intelligent control and communication among renewable energy sources such as solar PV sources, VRFB storage, building glazing loads, and the distribution grid through the utilization of energy meters. The energy meters display real-time data from the solar PV system, the grid, and the building glazing load. The MODBUS TCP/IP communication protocol connects these energy meters to the Ethernet switchboard. The information obtained from the Ethernet switchboard is then sent to the Raspberry-Pi processor, which uses real-time data to control the operation of the proposed smart energy management system. As shown in **Figure 5.4 (a)**, the two-way communication is carried out using the Message Queuing Telemetry Transport (MQTT) protocol. MQTT is a simple messaging communication protocol designed for low-bandwidth devices [124]. MQTT enables the sending of commands to control outputs and the reading and publishing of data from sensor nodes. As a result, communication between multiple devices becomes simple. It can send a command to control the output and read and publish data from the sensor. **Figure 5.4 (b)** illustrates the internal process flow of the IoT-based smart communication system. The mosquito broker uses MQTT to provide bidirectional communication between the Raspberry Pi Single Board Computer, laptop, and mobile devices that are part of the IoT-based smart communication system, as shown in **Figure 5.4 (b)**. Raspberry Pi Controller is the master controller that controls all the slave units comprising solar PV, VRFB storage, distribution grid and building glazing load. The communication between the master-slave unit is achieved through RS 485 Modbus or TCP/IP Modbus. A subscriber must send the broker a SUBSCRIBE message with the necessary topic to access the broker's data. A PUBLISH message is delivered from the publisher node to the broker when a publisher requests data for an existing subject. Persistent sessions, which are well suited for intermittent connectivity, are the sessions the broker maintains while the devices are turned on and off. This is a key advantage of MQTT over the HTTP server because it implies that if

devices go offline, the message is queued and updated automatically when the devices come back online.

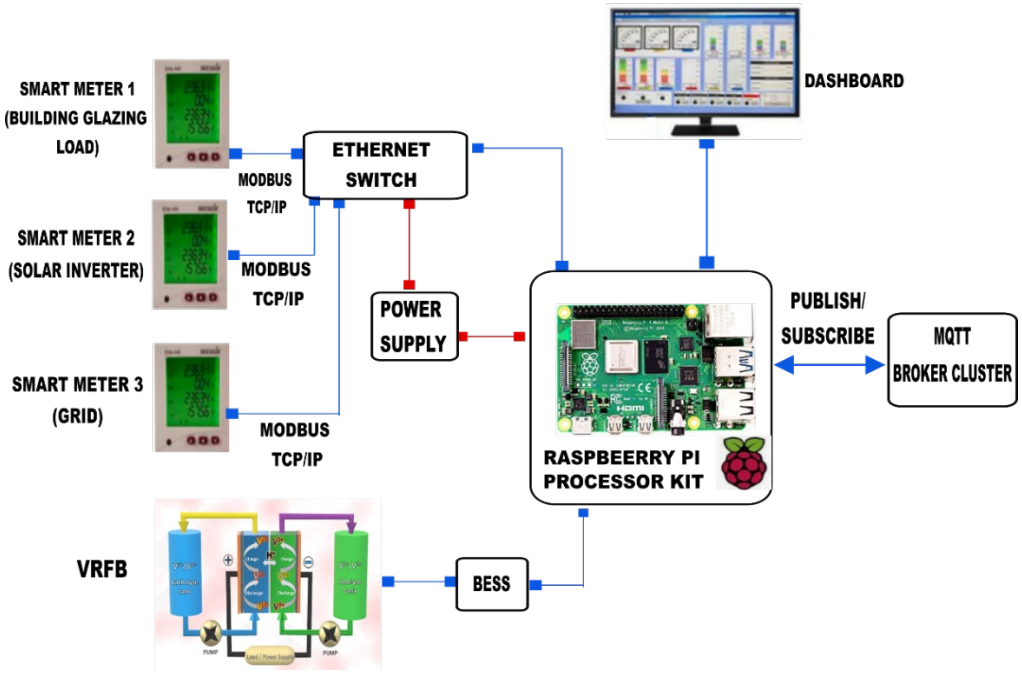

(a)

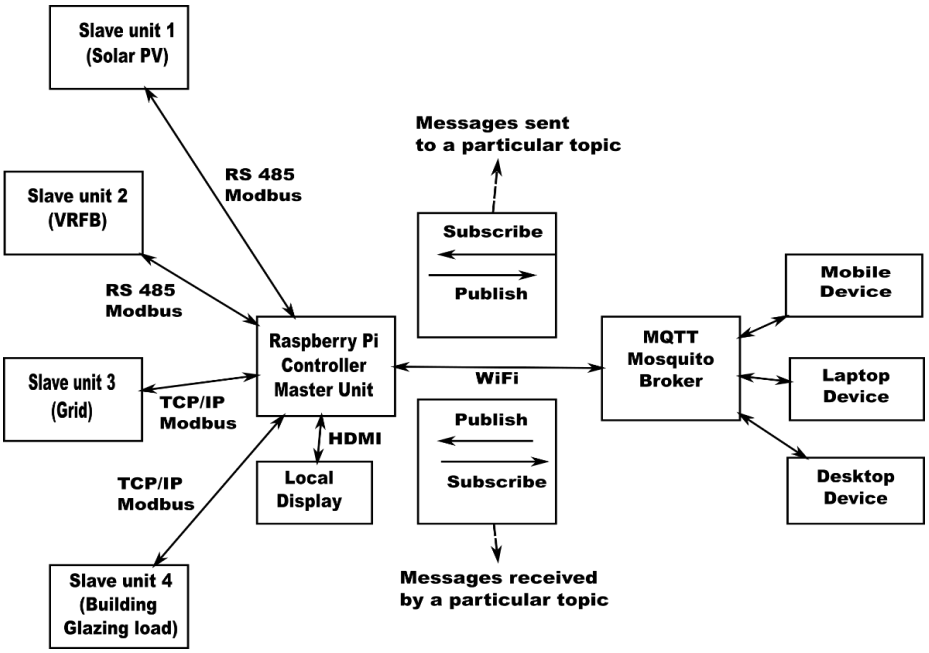

(b)

Figure 5.4: (a) Architecture of the proposed IoT-based smart communication system; (b) Internal process flow of the IoT-based smart communication system

The cost analysis of the proposed IoT-based smart communication system has been shown in **Table 5.1**.

Table 5.1: Cost analysis of IoT based smart communication system

IoT based smart communication system	**Cost (in INR)**
Raspberry-Pi 3 – Model B	3000
Full HD IPS Panel Monitor with HDMI, VGA	10000
D-Link DES-1008C 10/100 Mbps Switch Network switch	1500
HDMI Cable	500
Smart Meters - 3 (INR. 6000/- per Smart Meter)	18000
Total Cost	**33,000/-**

From the cost analysis of the proposed IoT based smart communication system, it can be observed that the utility of Raspberry Pi has reduced the total cost of the EMS system significantly.

5.3.2 Electrical interfacing system design

To ensure the efficient operation of the proposed system, the proper design of the electrical interfacing is essential. For this work, **Table 5.2** provides the system specifications of the major sub-systems, such as solar PV source, and VRFB storage. Based on the power requirement of 5W for activation of 1 m^2 area of glazing window glass as mentioned in section 5.2.2, in this work, for a 100 m^2 dimension of the window an EV charging station control room, the glazing load demands 500W, AC power supply.

Table 5.2: System level specification

Parameters	**Solar PV array**	**VRFB storage**
Voltage	$V_{mpp} \rightarrow 112.5$ V (DC)	$V_{stack} \rightarrow$ (20-32) V (DC)
Current	$I_{mpp} \rightarrow 17.8$ A	$I_{max\_stack} \rightarrow 60$ A
Power	$P_{rated} \rightarrow 2$ kW_p	$P_{rated} \rightarrow 1$ kW

*mpp – Maximum power point

Considering the constant HVAC demand requirement in the daytime, the glazing load demand is kept constant. Here, the installed solar PV array consists of 2 strings in parallel, with each string having 3 series solar PV modules of 340 W_p, thus forming a 2kW_p capacity. The solar PV capacity has been chosen as 2kW_p to satisfy the energy demand considering the intermittency and worst-case scenario, where the sudden cloud might reduce the power generation. For load shaving during transient scenarios, a 1 kW, 6 kWh VRFB storage considered in this work has the maximum allowable stack current of 60 A and the operating voltage range of 20V - 32V.

Table 5.3 displays the design parameters for the electrical interfacing system. The power electronic converter sub-systems have been designed based on the capacity of power generation, VRFB storage and building glazing load requirement. The input/output voltage, current, and switching frequency of the power electronic device used, power conversion efficiency, etc., have been calculated for the optimized design of the DC-AC and DC-DC stages. The power quality has also been considered by keeping the total harmonic distortion (THD) limit within 3%. The design parameters obtained for the electrical interfacing of the proposed system are crucial for the efficient performance of the different energy sources utilized in the proposed smart energy management approach.

Table 5.3: Design parameters for electrical interfacing of the proposed system

Parameters	**Grid-tied solar inverter (1-ph)**	**DC-DC bidirectional charge controller for VRFB**
Voltage	Rated input voltage → 110 V (DC) Rated output voltage → 230 V (AC)	110 V/32 V
Current	Rated input current → 12 A Rated output current → 8.7 A	18 A/60 A
Rated Power	2 kW	1.2 kW
Switching Frequency	100 kHz	100 kHz
Total Harmonic Distortion (THD)	~ 3%	~2.5%
Power Electronic Converter efficiency	97.4 %	98 %

5.4 Workflow of the proposed smart Solar - VRFB storage - Building glazing energy management

In this section, the workflow of the proposed approach is discussed. This section also details the priority scheduling of the different sources of energy involved in powering the building glazing load demand. **Figure 5.5** shows the flowchart of the proposed smart energy management approach for VRFB storage integrated EV charging stations with switchable building glazing load. The priority scheduling of solar PV power, VRFB storage and the distribution grid has been executed to power the switchable building glazing load. The MQTT protocol is used to transmit all these instructions and scheduling instructions to the main processor, which publishes the message and ensures effective communication across the IoT-based smart communication system. Depending on how much solar PV power is available during the day, it is given the highest priority at any time of the day [189]–[192]. In the first instance, the energy management algorithm utilized in the proposed system checks if the available solar PV power is adequate to satisfy the switchable building glazing load. When the algorithm condition check results are 'yes', the algorithm further checks whether VRFB SOC lies between 50% and 90%. If both conditions are satisfied, solar PV power is supplied to meet the switchable building glazing load, excess power is exported to the distribution grid, and MQTT publishes the message. Under the same scenario, if the VRFB SOC is less than 50%, solar PV power is supplied to power the switchable building glazing load and excess solar PV power is utilized to charge the VRFB storage until the VRFB SOC reaches 90%.

When the available solar PV power is less than the switchable building glazing load, then the algorithm further checks the SOC of VRFB storage. If VRFB SOC lies between 10% and 90%, the combination of solar PV power and VRFB storage is utilized to satisfy the switchable building glazing load demand. Then, MQTT publishes the message. When the available solar PV power is insufficient to manage the switchable building glazing load and VRFB storage is also unavailable, the algorithm checks for the availability of distribution grid and available solar PV power. Then the combination of the distribution grid power and available solar power is utilized to attain the required demand of switchable building glazing load demand. MQTT publishes the message. Under the worst-case scenario, when importing power from the distribution grid is not feasible due to frequent grid outage and solar power availability is also less due to cloudy weather, then available solar PV power and VRFB storage supply the required switchable building glazing load demand.

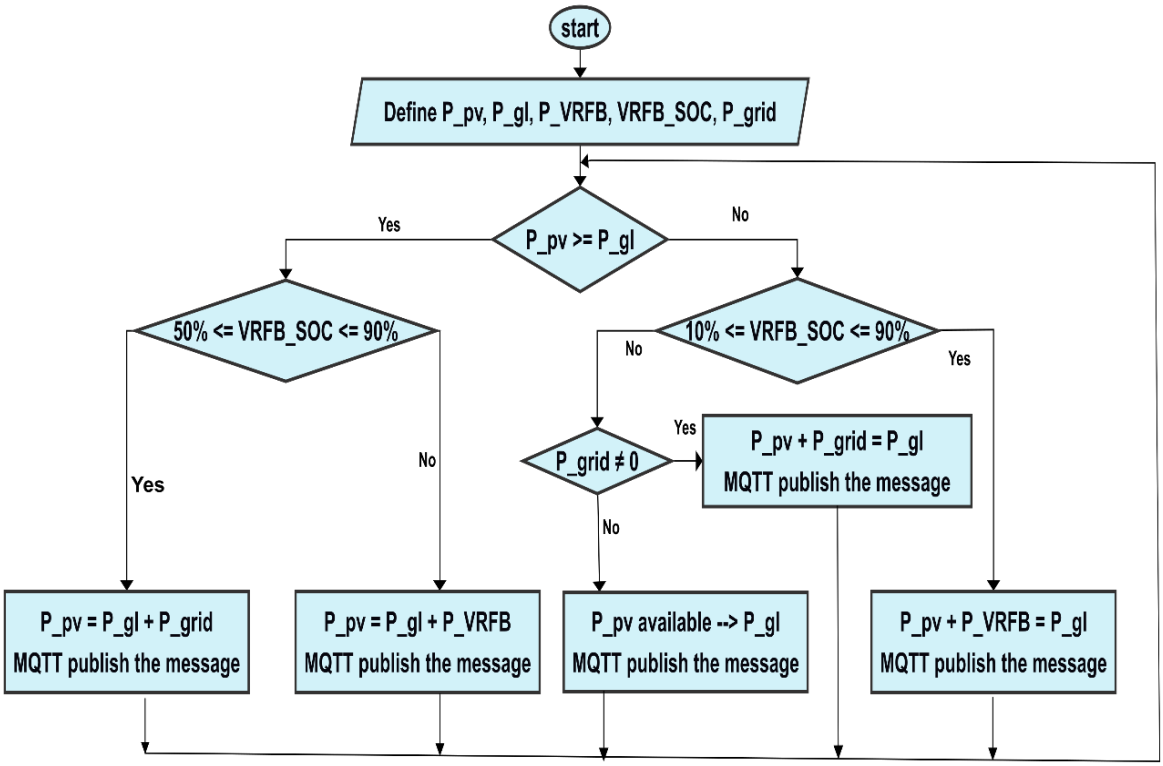

Figure 5.5: Flowchart of the proposed smart building glazing energy management approach

5.5 Results and discussion

The performance of the proposed smart energy management algorithm and IoT-based smart communication system has been validated by the practical solar PV-VRFB storage integrated EV charging station with switchable building glazing load demand. A practical load demand profile of 10 hrs duration (morning 6:00 A.M (06:00 hrs) to evening 4 P.M. (16:00 hrs)) has been chosen for validation of the proposed smart energy management algorithm. The switchable building glazing load demand is maintained at 500 W.

Therefore, to match the daily demand profile, the solar PV (2kW$_P$), VRFB storage (1 kW 6 hr) and distribution grid have been integrated to satisfy the switchable building glazing load demand. **Figures 5.6, 5.7, 5.8 and 5.9** show the results of four practical case studies for smart energy management under a sunny, cloudy, over-cloudy and worst-case scenario. The fourth case is considered the worst-case scenario because during those instances, the solar PV availability is low, and the grid undergoes frequent outages simultaneously, thus, making it challenging for the energy management algorithm to satisfy the building glazing load demand.

Solar PV source is the major contributor to achieving the building glazing load demand from the available power sources. As demonstrated in **Figures 5.6, 5.7, 5.8 and 5.9**, the negative magnitudes of the VRFB power represent the VRFB storage charging process. In contrast, the

positive magnitude of VRFB power represents the process of VRFB discharging. Furthermore, in the case of the distribution system, positive magnitudes of power represent the power imported from the distribution grid, and negative magnitudes of the power represent the power exported to the distribution grid during instances of surplus solar PV power output. The following are the results of the case studies obtained using the smart energy management approach in four different practical weather cases:

Case 1 (Sunny weather):

In the first case study, a sunny day with a clear sky is considered, and the smart energy management algorithm's results have been monitored from 06:00 hrs to 16:00 hrs, as shown in **Figure 5.6 (a)**. Since it is sunny weather, power generated from the solar module is completely utilized to satisfy the switchable building glazing load demand of 500 W. In addition to satisfying building glazing load demand, the remaining available excess solar PV power is supplied to charge the VRFB storage until VRFB SOC reaches 90% at 11:00 hrs, as shown in **Figure 5.6 (b)**. After satisfying the building glazing load demand and charging the VRFB storage, the available excess solar PV power is then exported to the distribution grid.

It can be seen in **Figure 5.6 (a)** from 10:00 hrs till 16:00 hrs that the highest peak power of 1000 W is exported to the distribution grid at 12:00 hrs when the solar insolation is at the maximum. It can be observed from **Figure 5.6 (b)** that VRFB SOC ranges from 50% to 90% during the sunny weather scenario. After 11:00 hrs, it can be observed that VRFB storage is fully charged and remains idle till 16:00 hrs. It can be inferred that the power stored in the VRFB storage effectively satisfies the building glazing load demand during night hours when the solar PV power source is unavailable. Thus, a smart energy management algorithm offers the scope for self-reliant and efficient allocation of resources to satisfy the power demand.

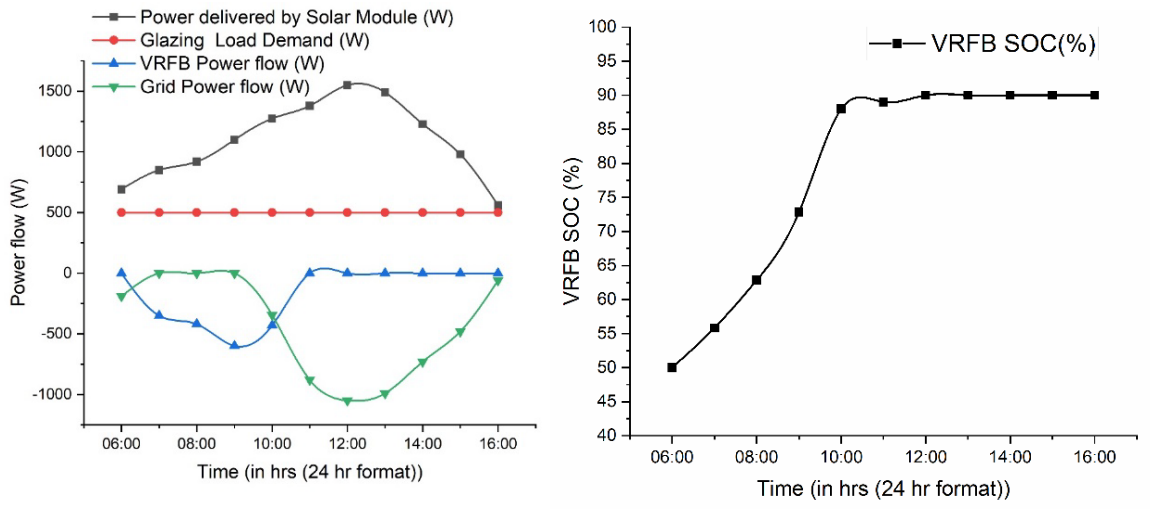

Figure 5.6: Sunny weather condition. (a) Power sharing among the energy source (s), storage, local grid to satisfy the building glazing load demand; (b) VRFB state of charge (SOC) over the time

Case 2 (Intermittent cloudy weather):

In this second case study, the performance of solar PV modules, VRFB storage and distribution grid performance is investigated under the sudden appearance of the cloud. The solar PV power fluctuates during the cloudy day because of the varying solar insolation profile, as shown in **Figure 5.7 (a)**. From 08:00 hrs to 09:30 hrs, VRFB storage supplies power to satisfy the building glazing load demand when the available solar PV power is less than the building glazing load demand. Similarly, the building glazing load demand is met by VRFB storage between 15:00 hrs and 16:00 hrs.

Excess power obtained from solar PV modules after satisfying the building glazing load demand and charging VRFB storage is exported to the distribution grid. During the overcast condition, at 12:00 hrs, a peak power of 400 W is exported to the grid, which is lower than the peak power exported to the grid during sunny conditions. VRFB SOC ranges between 47% and 68% during cloudy weather, as shown in **Figure 5.7 (b)**. VRFB storage has not achieved the maximum threshold charging limit of 90% during the overcast condition because of the regular discharge of power to fulfil the switchable building glazing load demand.

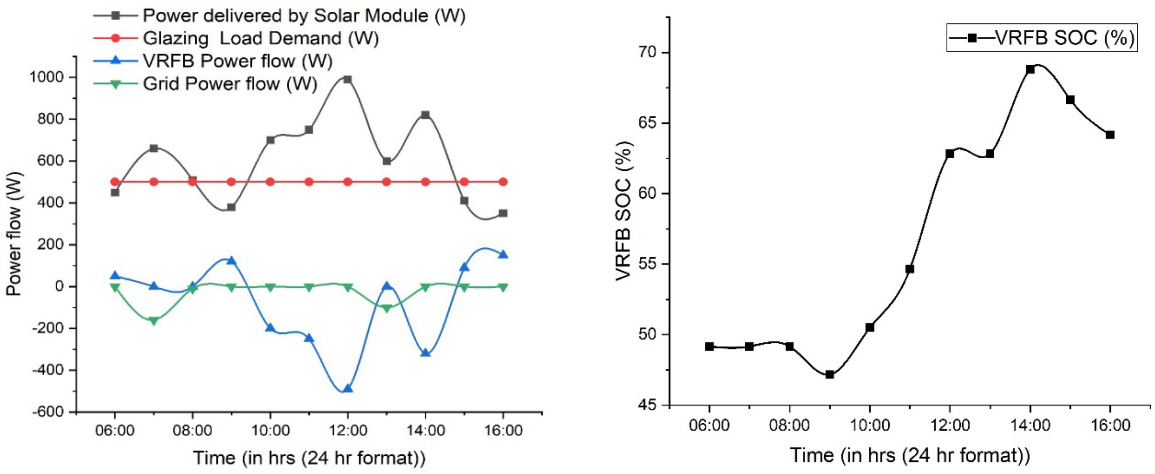

(a) **(b)**

Figure 5.7: Cloudy weather condition. (a) Power sharing among the energy source(s), storage, local grid to satisfy the building glazing load demand; (b) VRFB state of charge (SOC) over the time

Case 3 (Prolonged-cloudy weather):

During the prolonged-cloudy condition, solar PV power is inadequate to supply the building glazing load demand during the time duration (06:00 hrs to 09:00 hrs and 14:00 to 16:00 hrs) as shown in **Figure 5.8 (a)**. Therefore, during these instances, the power scheduling relied on the battery storage and the distribution grid to satisfy the building glazing load demand. In this case, VRFB SOC varies between 10% and 14%, as shown in **Figure 5.8 (b)**.

The range of VRFB SOC attained during the prolonged-cloudy weather scenario is of a lower magnitude when compared with sunny and cloudy weather conditions. VRFB storage is idle for the majority of the duration. From 11:00 to 13:00 hrs, charging of VRFB storage occurs due to the influx of solar PV power. At 09:00 hrs, the power generated by solar modules is 380 W. To attain the building glazing load demand of 500 W, the remaining 120 W is imported from the distribution grid.

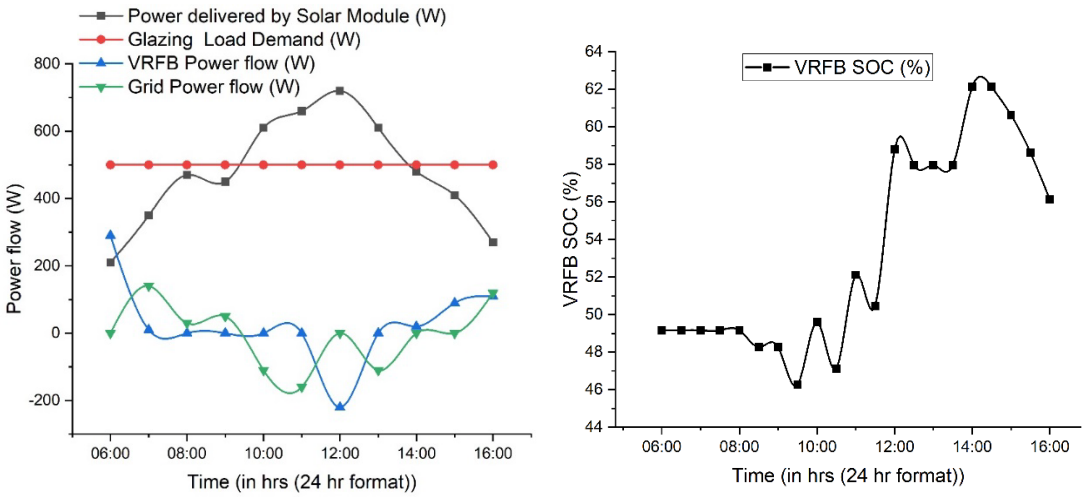

(a) **(b)**

Figure 5.8: Prolonged-cloudy condition. (a) Power sharing among the energy source(s), storage, local grid to satisfy the building glazing load demand; (b) VRFB state of charge (SOC) over the time

Case 4 (Worst Case scenario: both low solar availability and frequent grid outage):

In this case, the solar PV power availability is low and frequent grid outage persists. It is challenging to satisfy the building glazing load demand during this uncertain and volatile scenario. This worst-case scenario has been presented in **Figure 5.9 (a)**. Here, VRFB storage plays a vital role during power scheduling for demand management. When solar PV power is inadequate, the building glazing load demand is powered by VRFB storage. It is to be noted that the fast response of VRFB storage is helpful during instances of power deficit to satisfy the building glazing load demand. After satisfying the building glazing load demand, the surplus power from the solar PV module is further utilized to charge the VRFB storage. In this case, the VRFB SOC varies between 46% and 62% throughout the day, as shown in **Figure 5.9 (b)**. In this case, the power exported to the distribution grid is lower than in sunny and cloudy conditions. A peak power of 200 W is exported to the grid at 07:00 hrs. During this case, it can be inferred that the power scheduling involved utilizing all three power sources in different instances to fulfil the power requirement of a switchable building glazing system in an EV charging station.

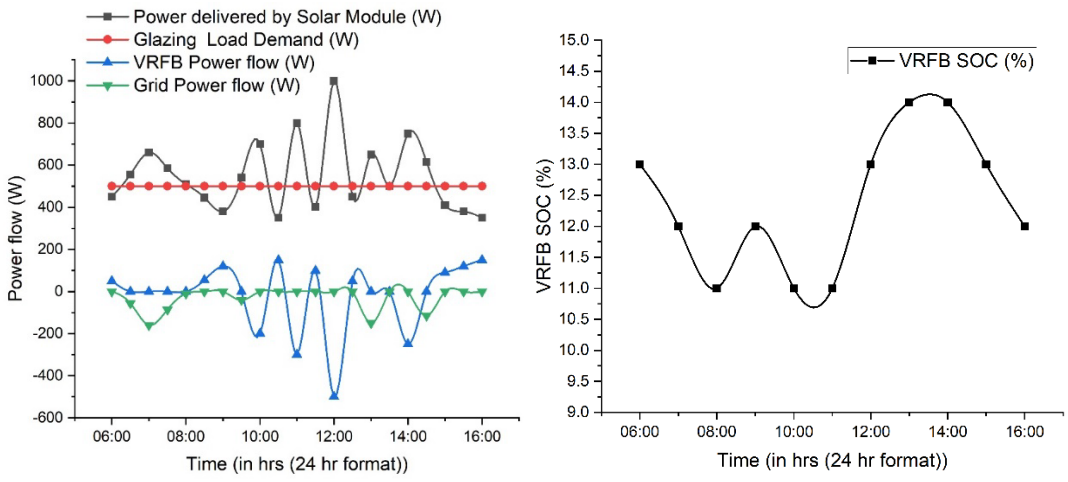

Figure 5.9: Worst case scenario weather condition. (a) Power sharing among the energy source(s), storage, local grid to satisfy the building glazing load demand; (b) VRFB state of charge (SOC) over the time

Further study has been carried out to establish the application of smart glazing window in maintaining the desired temperature inside the EV charging station control room. According to the Köppen climate classification, type A climatic zone is used to represent countries with tropical and sub-tropical climates, whose average temperature of the coldest month is greater than 18°C. The proposed system is meant to be useful for such countries as follows: South American countries such as Brazil, Venezuela and Columbia; African countries such as Nigeria and Democratic Republic of Congo; Asian countries including Southern part of India, South-east Asian countries such as Thailand, Vietnam and Cambodia. In addition to the above, further significant contribution of this work is towards the sustainable and green transportation infrastructure by integrating solar-VRFB storage with EV charging station.

5.6 Conclusion

In this chapter, a grid interactive solar PV-VRFB integrated switchable building glazing topology has been implemented for providing day-time passive HVAC facility in EV charging station control rooms for the first time. Further, in order to satisfy the building glazing load demand under real time dynamic environmental condition, an IoT based smart scheduling of solar PV, VRFB storage and the local distribution grid has been demonstrated. The performance of the proposed topology has been validated under four different transient scenarios; sunny, intermittent cloudy, prolonged cloudy and low solar irradiance with frequent grid outage. With the help of proposed smart power management algorithm, the SOC level of

VRFB storage has also been maintained within the safe limit of 10% - 90% including all the case studies, based on the scope of charge-discharge, solar PV availability, and building glazing load demand. This will further take care of the battery life and optimize utilization of storage in renewable power systems. The proposed solution is a generalized one and thus can be very useful for upscaled capacity as well.

Chapter 6

Conclusion

6.1 Conclusion

In this thesis, four major aspects of research and development work on Vanadium Redox Flow Battery (VRFB) have been addressed considering the necessity of efficient interfacing of VRFB storage with renewable energy sources and other power system applications. These includes,

- Development of dynamic equivalent model of VRFB storage system for estimating its capacity fade.
- Machine-Learning based prediction of VRFB storage system losses considering different charge-discharge conditions.
- Optimization of VRFB storage system losses considering the dynamic operating conditions.
- Development of a smart electrical interfacing system for long-life flow battery storage integrated Solar- EV charging stations with switchable Building Glazing.

The works done in this thesis are summarized as follows,

In chapter 1, the introduction and the motivation of the proposed work has been discussed. A detailed study on the modeling of VRFB storage has been analyzed and the significant advantages of VRFB over the other potential batteries like Li-ion have been addressed.

In chapter 2, a MATLAB/Simulink based electrical equivalent model of VRFB storage has been proposed with an objective of interfacing VRFB with renewable energy sources. The impact of practical parameters like flow rate, self-discharge, pump power loss and charge-discharge current profile has been considered for analyzing the VRFB storage system performance. A comprehensive dynamic model for estimating the capacity fade of VRFB storage system has been implemented. The dynamic behavior of vanadium ion concentration in stack and tank has been considered in this work during the estimation of capacity fading of VRFB storage. The dynamic behavior of electrolyte volume in stack and tanks has been considered during the modeling. The optimization of electrolyte rebalancing has been proposed

in this work to minimize the electrolyte volume loss during the operation. The proposed optimal scheduling of electrolyte rebalancing is significant for minimizing the capacity fading of VRFB storage in the long run. An optimal multi-objective flow management has been implemented for minimizing the capacity fade and voltage loss of the VRFB storage.

In Chapter 3, the prediction of the overall system power loss of Vanadium Redox Flow Battery (VRFB) using different machine learning (ML) algorithms has been demonstrated for the first time. Under different operating current levels and electrolyte flow rates, the internal resistance variation and pump power consumption of the practical 1kW 6kWh VRFB system dataset have been considered for prediction. The prediction accuracy of ML algorithms has been analyzed in detail based on the regression metrics such as correlation coefficient (R^2), mean absolute error (MAE), and root mean square error (RMSE). It is observed that the Ensemble learning (EL) based Adaptive Boost (AdaBoost) algorithm is superior in predicting VRFB system loss compared to that of linear regression (LR) and support vector regression (SVR) algorithms. The prediction results obtained in this work claim to be beneficial for designing optimised interfacing of VRFB storage with renewable energy sources and other power system applications.

In Chapter 4, a kW scale VRFB storage system power loss optimization based on Nonlinear programming, GA and PSO techniques has been compared. The global optimal solution obtained from PSO technique is better in comparison to optimization results obtained from Nonlinear programming approach and GA. The multi-variable optimization considering both the VRFB pump power loss and stack power loss simultaneously has been executed in this work. The electrolyte flow rate has been considered the control variable in optimizing the overall VRFB system power loss. Charge-discharge operations of VRFB with four sets of electrolyte flow rates at three different levels of stack terminal current have been taken to validate the proposed work.

In Chapter 5, Solar-VRFB storage integrated switchable glazing topology has been applied for providing daytime passive heating ventilation and air conditioning (HVAC) in EV charging station control rooms. The EV charging station has been accompanied by a solar PV source installed on its roof-top to promote green energy and sustainable transportation. Vanadium redox flow battery (VRFB) has been integrated with the system to ensure energy security as a long-life energy storage solution. To satisfy the building glazing load demand under real-time dynamic environmental conditions, an Internet of Things (IoT) based smart scheduling of solar

PV, VRFB storage and the local distribution grid has been demonstrated. The performance of the proposed system has been validated under four different transient scenarios; sunny, intermittent cloudy, prolonged cloudy and low solar irradiance with frequent grid outages. The proposed solution is a generalized one and thus can be very useful for scaled-up capacity. The results obtained in this work lead to further scaling up and implementation of VRFB storage towards sustainable development goal.

6.2 Limitations in each chapter and the possible avenues to overcome those challenges

- In this study, Chapter 2 introduces an approach for estimating the capacity fade of VRFB storage. However, the investigation into predicting the chemical aging of VRFB and determining the remaining useful life of the storage system remains unexplored. The integration of Artificial Intelligence (AI)/ Machine Learning (ML) techniques is a promising avenue to address these prediction challenges.
- Chapter 3 proposes ML based prediction model for VRFB storage system power loss based on machine learning. Notably, the exploration of deep learning methods for predicting system power loss may further improve accuracy of prediction.
- Chapter 4 focuses on optimizing the electrolyte flow rate of the VRFB system, showcasing techniques like PSO and GA. To enhance this optimization process, the potential application of additional bio-inspired optimization algorithms warrants exploration.
- In Chapter 5, although the study delves into integrating VRFB storage integration with renewable energy sources, but it leaves a scope of further research on the development and optimization of suitable power electronic converters to efficiently interface VRFB storage with renewable energy systems and other power system applications.

Summary

Specific Contributions of the work

The specific contributions of the work are given below,

Chapter 1: Introduction to the need for Vanadium Redox Flow Battery (VRFB) storage in renewable energy applications and its comparative performance analysis with reference to the other contemporary battery storage systems (Lead Acid, Li-ion, NaS, etc.). An extensive study and analysis of VRFB storage system modeling and interfacing of Vanadium Redox Flow Battery with renewable energy sources.

Chapter 2: Development of dynamic electrical equivalent modeling of VRFB storage system. A comprehensive capacity fade model of VRFB storage system proposed to estimate the aging of VRFB storage. Experimental validation of the model performance by a practical 1kW 6h VRFB system.

Chapter 3: The prediction of the overall system power loss of VRFB storage using machine learning (ML) algorithms such as linear regression (LR), support vector regression (SVR), and ensemble learning (EL) based Adaptive Boost (AdaBoost) algorithm has been demonstrated. The ML-based predictive models have been trained and validated by experimental dataset of a 1kW 6h VRFB storage system under different stack terminal currents and electrolyte flow rates.

Chapter 4: The optimization of a kW scale VRFB storage system power loss based on Nonlinear programming, Particle Swarm Optimization (PSO) and Genetic Algorithm (GA) has been compared. The proposed optimization techniques consider both the VRFB pump power loss and stack power loss simultaneously to determine the optimal electrolyte flow rate at which the VRFB system power loss becomes the minimum and hence VRFB storage system efficiency becomes the maximum.

Chapter 5: Solar-VRFB storage integrated switchable glazing topology has been applied for providing daytime passive heating ventilation and air conditioning (HVAC) in Electric Vehicle (EV) charging station control rooms. The Internet of Things (IoT) based smart scheduling of solar PV, VRFB storage and the local distribution grid has been demonstrated to satisfy the building glazing load demand. The performance of the proposed system has been validated under four different practical weather scenarios.

Chapter 6: Conclusion of the work has been discussed.

Future scope of work

Considering the VRFB storage at utility scale and power system applications, VRFB storage has the potential to be used in a variety of applications, including grid-scale energy storage, microgrids and electric vehicle charging etc. This thesis work can be further extended to,

- Besides the machine learning (ML) based prediction of VRFB system power loss demonstrated in this work, the ML based prediction of thermal behavior of VRFB, prediction of chemical aging of VRFB, remaining useful life of VRFB etc. need to be addressed to further improve the overall performance of VRFB system.
- In addition to the demonstrated optimization techniques for determining the optimal electrolyte flow rate of VRFB system such as PSO, GA; further implementation of more such bio-inspired optimization algorithms can be explored.

Considering the revolutionary growth of power electronics in the field of renewable energy applications, it is important to address the selection criteria and design of suitable power electronic converters for energy storage interfacing. In the existing literature so far, extensive study on the suitable power electronic converter design for VRFB storage integration with renewable energy sources has not been discussed in detail. Hence there is a scope for further research and development in selection of suitable and optimized power electronic converters for efficient interfacing of VRFB storage with renewable energy systems.

References

[1] T. M. I. Mahlia, T. J. Saktisahdan, A. Jannifar, M. H. Hasan, and H. S. C. Matseelar, "A review of available methods and development on energy storage; Technology update," *Renew. Sustain. Energy Rev.*, vol. 33, pp. 532–545, 2014, doi: 10.1016/j.rser.2014.01.068.

[2] Z. Huang, A. Mu, L. Wu, B. Yang, Y. Qian, and J. Wang, "Comprehensive Analysis of Critical Issues in All-Vanadium Redox Flow Battery," vol. 07, p. 36, 2022, doi: 10.1021/acssuschemeng.2c01372.

[3] M. Fichtner *et al.*, "Rechargeable Batteries of the Future—The State of the Art from a BATTERY 2030+ Perspective," *Adv. Energy Mater.*, vol. 12, no. 17, 2022, doi: 10.1002/aenm.202102904.

[4] H. Zhao, Q. Wu, S. Hu, H. Xu, and C. N. Rasmussen, "Review of energy storage system for wind power integration support," *Appl. Energy*, vol. 137, pp. 545–553, Jan. 2015, doi: 10.1016/J.APENERGY.2014.04.103.

[5] T. Ould Ely, D. Kamzabek, and D. Chakraborty, "Batteries Safety: Recent Progress and Current Challenges," *Front. Energy Res.*, vol. 7, no. September, 2019, doi: 10.3389/fenrg.2019.00071.

[6] A. Poullikkas, "A comparative overview of large-scale battery systems for electricity storage," *Renew. Sustain. Energy Rev.*, vol. 27, pp. 778–788, 2013, doi: 10.1016/j.rser.2013.07.017.

[7] C. Ling, "A review of the recent progress in battery informatics," *npj Comput. Mater.*, vol. 8, no. 1, pp. 1–22, 2022, doi: 10.1038/s41524-022-00713-x.

[8] J. Ma *et al.*, "The 2021 battery technology roadmap," *J. Phys. D. Appl. Phys.*, vol. 54, no. 18, 2021, doi: 10.1088/1361-6463/abd353.

[9] C. D. Parker, "Lead–acid battery energy-storage systems for electricity supply networks," *J. Power Sources*, vol. 100, no. 1–2, pp. 18–28, Nov. 2001, doi: 10.1016/S0378-7753(01)00880-1.

[10] S. Mahmud *et al.*, "Recent advances in lithium-ion battery materials for improved electrochemical performance: A review," *Results Eng.*, vol. 15, no. June, p. 100472,

2022, doi: 10.1016/j.rineng.2022.100472.

[11] A. Ritchie and W. Howard, “Recent developments and likely advances in lithium-ion batteries,” *J. Power Sources*, vol. 162, no. 2, pp. 809–812, Nov. 2006, doi: 10.1016/J.JPOWSOUR.2005.07.014.

[12] H. Ahmad, K. Tul, A. Butt, U. Nisar, F. Jan, and G. Ali, “Recent progress , challenges , and perspectives in the development of solid-state electrolytes for sodium batteries,” *J. Power Sources*, vol. 581, no. August, p. 233518, 2023, doi: 10.1016/j.jpowsour.2023.233518.

[13] Z. Wen, J. Cao, Z. Gu, X. Xu, F. Zhang, and Z. Lin, “Research on sodium sulfur battery for energy storage,” *Solid State Ionics*, vol. 179, no. 27–32, pp. 1697–1701, 2008, doi: 10.1016/j.ssi.2008.01.070.

[14] K. Liu *et al.*, “Transfer learning for battery smarter state estimation and ageing prognostics: Recent progress, challenges, and prospects,” *Adv. Appl. Energy*, vol. 9, no. October 2022, p. 100117, 2023, doi: 10.1016/j.adapen.2022.100117.

[15] P. Alotto, M. Guarnieri, and F. Moro, “Redox flow batteries for the storage of renewable energy: A review,” *Renew. Sustain. Energy Rev.*, vol. 29, pp. 325–335, 2014, doi: 10.1016/j.rser.2013.08.001.

[16] A. Parasuraman, T. M. Lim, C. Menictas, and M. Skyllas-Kazacos, “Review of material research and development for vanadium redox flow battery applications,” *Electrochim. Acta*, vol. 101, pp. 27–40, 2013, doi: 10.1016/j.electacta.2012.09.067.

[17] T. Khan, A. K. Garg, A. Gupta, A. K. Madan, and P. K. Jain, “Comprehensive review on latest advances on rechargeable batteries,” *J. Energy Storage*, vol. 57, no. October 2022, p. 106204, 2023, doi: 10.1016/j.est.2022.106204.

[18] Q. Xu, T. S. Zhao, and P. K. Leung, “Numerical investigations of flow field designs for vanadium redox flow batteries,” *Appl. Energy*, vol. 105, pp. 47–56, 2013, doi: 10.1016/j.apenergy.2012.12.041.

[19] H. Wang, S. A. Pourmousavi, W. L. Soong, X. Zhang, and N. Ertugrul, “Battery and energy management system for vanadium redox flow battery: A critical review and recommendations,” *J. Energy Storage*, vol. 58, no. December 2022, p. 106384, Feb.

2023, doi: 10.1016/j.est.2022.106384.

[20] M. Skyllas-Kazacos, M. H. Chakrabarti, S. A. Hajimolana, F. S. Mjalli, and M. Saleem, “Progress in Flow Battery Research and Development,” *J. Electrochem. Soc.*, vol. 158, no. 8, p. R55, 2011, doi: 10.1149/1.3599565.

[21] O. C. Esan, X. Shi, Z. Pan, X. Huo, L. An, and T. S. Zhao, “Modeling and Simulation of Flow Batteries,” *Adv. Energy Mater.*, vol. 2000758, pp. 1–42, 2020, doi: 10.1002/aenm.202000758.

[22] X. Z. Yuan *et al.*, “A review of all-vanadium redox flow battery durability: Degradation mechanisms and mitigation strategies,” *International Journal of Energy Research*, vol. 43, no. 13. John Wiley and Sons Ltd, pp. 6599–6638, Oct. 25, 2019. doi: 10.1002/er.4607.

[23] H. He, S. Tian, B. Tarroja, O. A. Ogunseitan, S. Samuelsen, and J. M. Schoenung, “Flow battery production: Materials selection and environmental impact,” *J. Clean. Prod.*, vol. 269, 2020, doi: 10.1016/j.jclepro.2020.121740.

[24] T. Shigematsu, “Redox flow battery for energy storage,” *SEI Tech. Rev.*, vol. 28, no. 73, pp. 4–13, 2011, doi: 10.1149/1.3492325.

[25] W. Wang, Q. Luo, B. Li, X. Wei, L. Li, and Z. Yang, “Recent progress in redox flow battery research and development,” *Adv. Funct. Mater.*, vol. 23, no. 8, pp. 970–986, 2013, doi: 10.1002/adfm.201200694.

[26] M. Ulaganathan, V. Aravindan, Q. Yan, S. Madhavi, M. Skyllas-Kazacos, and T. M. Lim, “Recent Advancements in All-Vanadium Redox Flow Batteries,” *Adv. Mater. Interfaces*, vol. 3, no. 1, pp. 1–22, 2016, doi: 10.1002/admi.201500309.

[27] Y. Shi *et al.*, “Recent development of membrane for vanadium redox flow battery applications: A review,” *Appl. Energy*, vol. 238, no. December 2018, pp. 202–224, 2019, doi: 10.1016/j.apenergy.2018.12.087.

[28] L. Gubler, “Membranes and separators for redox flow batteries,” *Curr. Opin. Electrochem.*, vol. 18, pp. 31–36, 2019, doi: 10.1016/j.coelec.2019.08.007.

[29] M. Skyllas-Kazacos and J. F. McCann, *Vanadium redox flow batteries (VRBs) for medium- and large-scale energy storage*, no. Iv. Elsevier Ltd., 2015. doi: 10.1016/B978-

1-78242-013-2.00010-8.

[30] Z. Huang and A. Mu, “Research and analysis of performance improvement of vanadium redox flow battery in microgrid: A technology review,” *Int. J. Energy Res.*, vol. 45, no. 10, pp. 14170–14193, 2021, doi: 10.1002/er.6716.

[31] J. E. Mengou, A. Trovo, C. Gambaro, and M. Guarnieri, “A vanadium redox flow battery bracing the pilot microgrid at Eni Renewable Energy and Environmental RDCenter,” in *Proceedings of the IEEE International Conference on Industrial Technology*, 2021, vol. 2021-March, pp. 298–303. doi: 10.1109/ICIT46573.2021.9453702.

[32] Q. Zheng, X. Li, Y. Cheng, G. Ning, F. Xing, and H. Zhang, “Development and perspective in vanadium flow battery modeling,” *Appl. Energy*, vol. 132, pp. 254–266, 2014, doi: 10.1016/j.apenergy.2014.06.077.

[33] Q. Xu and T. S. Zhao, “Determination of the mass-transport properties of vanadium ions through the porous electrodes of vanadium redox flow batteries,” *Phys. Chem. Chem. Phys.*, vol. 15, no. 26, pp. 10841–10848, 2013, doi: 10.1039/c3cp51944a.

[34] I. M. Bayanov and R. Vanhaelst, “The numerical simulation of vanadium RedOx flow batteries,” *J. Math. Chem.*, vol. 49, no. 9, pp. 2013–2031, 2011, doi: 10.1007/s10910-011-9872-x.

[35] N. Xu, X. Li, X. Zhao, J. B. Goodenough, and K. Huang, “A novel solid oxide redox flow battery for grid energy storage,” *Energy Environ. Sci.*, vol. 4, no. 12, pp. 4942–4946, 2011, doi: 10.1039/c1ee02489b.

[36] M. Vynnycky, “Analysis of a model for the operation of a vanadium redox battery,” *Energy*, vol. 36, no. 4, pp. 2242–2256, 2011, doi: 10.1016/j.energy.2010.03.060.

[37] D. You, H. Zhang, C. Sun, and X. Ma, “Simulation of the self-discharge process in vanadium redox flow battery,” *J. Power Sources*, vol. 196, no. 3, pp. 1578–1585, 2011, doi: 10.1016/j.jpowsour.2010.08.036.

[38] M. Vijayakumar *et al.*, “Towards understanding the poor thermal stability of V5+ electrolyte solution in Vanadium Redox Flow Batteries,” *J. Power Sources*, vol. 196, no. 7, pp. 3669–3672, 2011, doi: 10.1016/j.jpowsour.2010.11.126.

[39] M. Vijayakumar *et al.*, “Nuclear magnetic resonance studies on vanadium(IV)

electrolyte solutions for vanadium redox flow battery," *J. Power Sources*, vol. 195, no. 22, pp. 7709–7717, 2010, doi: 10.1016/j.jpowsour.2010.05.008.

[40] M. Vijayakumar, L. Li, Z. Nie, Z. Yang, and J. Hu, "Structure and stability of hexa-aqua V(III) cations in vanadium redox flow battery electrolytes," *Phys. Chem. Chem. Phys.*, vol. 14, no. 29, pp. 10233–10242, 2012, doi: 10.1039/c2cp40707h.

[41] L. F. Arenas, C. Ponce de León, and F. C. Walsh, "Redox flow batteries for energy storage: their promise, achievements and challenges," *Curr. Opin. Electrochem.*, vol. 16, pp. 117–126, 2019, doi: 10.1016/j.coelec.2019.05.007.

[42] X. Qiu, T. A. Nguyen, J. D. Guggenberger, M. L. Crow, and A. C. Elmore, "A field validated model of a vanadium redox flow battery for microgrids," *IEEE Trans. Smart Grid*, vol. 5, no. 4, pp. 1592–1601, 2014, doi: 10.1109/TSG.2014.2310212.

[43] G. Qiu, A. S. Joshi, C. R. Dennison, K. W. Knehr, E. C. Kumbur, and Y. Sun, "3-D pore-scale resolved model for coupled species/charge/fluid transport in a vanadium redox flow battery," *Electrochim. Acta*, vol. 64, pp. 46–64, 2012, doi: 10.1016/j.electacta.2011.12.065.

[44] M. Bartolozzi, "Development of redox flow batteries. A historical bibliography," *J. Power Sources*, vol. 27, no. 3, pp. 219–234, 1989, doi: 10.1016/0378-7753(89)80037-0.

[45] V. Ramadesigan, P. W. C. Northrop, S. De, S. Santhanagopalan, R. D. Braatz, and V. R. Subramanian, "Modeling and Simulation of Lithium-Ion Batteries from a Systems Engineering Perspective," *J. Electrochem. Soc.*, vol. 159, no. 3, pp. R31–R45, 2012, doi: 10.1149/2.018203jes.

[46] K. Darcovich, E. R. Henquin, B. Kenney, I. J. Davidson, N. Saldanha, and I. Beausoleil-Morrison, "Higher-capacity lithium ion battery chemistries for improved residential energy storage with micro-cogeneration," *Appl. Energy*, vol. 111, pp. 853–861, 2013, doi: 10.1016/j.apenergy.2013.03.088.

[47] M. Zhang, M. Moore, J. S. Watson, T. A. Zawodzinski, and R. M. Counce, "Capital Cost Sensitivity Analysis of an All-Vanadium Redox-Flow Battery," *J. Electrochem. Soc.*, vol. 159, no. 8, pp. A1183–A1188, 2012, doi: 10.1149/2.041208jes.

[48] V. Viswanathan *et al.*, "Cost and performance model for redox flow batteries," *J. Power Sources*, vol. 247, pp. 1040–1051, 2014, doi: 10.1016/j.jpowsour.2012.12.023.

[49] C. Blanc, "Modeling of a vanadium redox flow battery electricity storage system," *Lab. d'Electronique Ind.*, vol. PhD Thesis, p. 263, 2009, doi: 10.5075/epfl-thesis-4277.

[50] A. Bhattacharjee and H. Saha, "Design and experimental validation of a generalised electrical equivalent model of Vanadium Redox Flow Battery for interfacing with renewable energy sources," *J. Energy Storage*, vol. 13, pp. 220–232, 2017, doi: 10.1016/j.est.2017.07.016.

[51] Y. Zhang, J. Zhao, P. Wang, M. Skyllas-Kazacos, B. Xiong, and R. Badrinarayanan, "A comprehensive equivalent circuit model of all-vanadium redox flow battery for power system analysis," *J. Power Sources*, vol. 290, pp. 14–24, 2015, doi: 10.1016/j.jpowsour.2015.04.169.

[52] A. Van Der Ven, J. C. Thomas, Q. Xu, B. Swoboda, and D. Morgan, "Nondilute diffusion from first principles: Li diffusion in Lix TiS2," *Phys. Rev. B - Condens. Matter Mater. Phys.*, vol. 78, no. 10, pp. 1–12, 2008, doi: 10.1103/PhysRevB.78.104306.

[53] Q. H. Zeng, A. B. Yu, and G. Q. Lu, "Multiscale modeling and simulation of polymer nanocomposites," *Prog. Polym. Sci.*, vol. 33, no. 2, pp. 191–269, 2008, doi: 10.1016/j.progpolymsci.2007.09.002.

[54] J. Bhattacharya and A. Van Der Ven, "Phase stability and nondilute Li diffusion in spinel Li 1+xTi2O4," *Phys. Rev. B - Condens. Matter Mater. Phys.*, vol. 81, no. 10, pp. 27–30, 2010, doi: 10.1103/PhysRevB.81.104304.

[55] A. B. Bortz, M. H. Kalos, and J. L. Lebowitz, "[Bortz, 1975] KMC-BKL algorithm.pdf," *J. Comput. Phys.*, vol. 17, no. 1, pp. 10–18, 1975.

[56] A. Van der Ven and G. Ceder, "Lithium diffusion mechanisms in layered intercalation compounds," *J. Power Sources*, vol. 97–98, no. June 2000, pp. 529–531, 2001, doi: 10.1016/S0378-7753(01)00638-3.

[57] B. Battke, T. S. Schmidt, D. Grosspietsch, and V. H. Hoffmann, "A review and probabilistic model of lifecycle costs of stationary batteries in multiple applications," *Renew. Sustain. Energy Rev.*, vol. 25, pp. 240–250, 2013, doi:

10.1016/j.rser.2013.04.023.

[58] T. Ma, H. Yang, and L. Lu, “A feasibility study of a stand-alone hybrid solar-wind-battery system for a remote island,” *Appl. Energy*, vol. 121, pp. 149–158, 2014, doi: 10.1016/j.apenergy.2014.01.090.

[59] E. McKenna, M. McManus, S. Cooper, and M. Thomson, “Economic and environmental impact of lead-acid batteries in grid-connected domestic PV systems,” *Appl. Energy*, vol. 104, pp. 239–249, 2013, doi: 10.1016/j.apenergy.2012.11.016.

[60] B. Turker, S. Arroyo Klein, E. M. Hammer, B. Lenz, and L. Komsiyska, “Modeling a vanadium redox flow battery system for large scale applications,” *Energy Convers. Manag.*, vol. 66, pp. 26–32, 2013, doi: 10.1016/j.enconman.2012.09.009.

[61] A. Bhattacharjee, H. Samanta, N. Banerjee, and H. Saha, “Development and validation of a real time flow control integrated MPPT charger for solar PV applications of vanadium redox flow battery,” *Energy Convers. Manag.*, vol. 171, no. June, pp. 1449–1462, 2018, doi: 10.1016/j.enconman.2018.06.088.

[62] M. Karimi, H. Mokhlis, K. Naidu, S. Uddin, and A. H. A. Bakar, “Photovoltaic penetration issues and impacts in distribution network - A review,” *Renew. Sustain. Energy Rev.*, vol. 53, pp. 594–605, 2016, doi: 10.1016/j.rser.2015.08.042.

[63] H. Fathabadi, “Novel high efficiency DC/DC boost converter for using in photovoltaic systems,” *Sol. Energy*, vol. 125, pp. 22–31, 2016, doi: 10.1016/j.solener.2015.11.047.

[64] H. Fathabadi, “Novel photovoltaic based battery charger including novel high efficiency step-up DC/DC converter and novel high accurate fast maximum power point tracking controller,” *Energy Convers. Manag.*, vol. 110, pp. 200–211, 2016, doi: 10.1016/j.enconman.2015.12.025.

[65] J. López, S. I. Seleme, P. F. Donoso, L. M. F. Morais, P. C. Cortizo, and M. A. Severo, “Digital control strategy for a buck converter operating as a battery charger for stand-alone photovoltaic systems,” *Sol. Energy*, vol. 140, pp. 171–187, 2016, doi: 10.1016/j.solener.2016.11.005.

[66] L. Barote, M. Georgescu, and C. Marinescu, “Smart storage solution for wind systems,” *2009 IEEE Bucharest PowerTech Innov. Ideas Towar. Electr. Grid Futur.*, pp. 1–6,

2009, doi: 10.1109/PTC.2009.5281919.

[67] Y. R. Challapuram, G. M. Quintero, S. B. Bayne, A. S. Subburaj, and M. A. Harral, "Electrical Equivalent Model of Vanadium Redox Flow Battery," *IEEE Green Technol. Conf.*, vol. 2019-April, no. 2, pp. 4–7, 2019, doi: 10.1109/GreenTech.2019.8767145.

[68] R. Badrinarayanan, J. Zhao, K. J. Tseng, and M. Skyllas-Kazacos, "Extended dynamic model for ion diffusion in all-vanadium redox flow battery including the effects of temperature and bulk electrolyte transfer," *J. Power Sources*, vol. 270, pp. 576–586, 2014, doi: 10.1016/j.jpowsour.2014.07.128.

[69] M. R. Mohamed, H. Ahmad, M. N. A. Seman, S. Razali, and M. S. Najib, "Electrical circuit model of a vanadium redox flow battery using extended Kalman filter," *J. Power Sources*, vol. 239, pp. 284–293, 2013, doi: 10.1016/j.jpowsour.2013.03.127.

[70] B. Turker *et al.*, "Utilizing a vanadium redox flow battery to avoid wind power deviation penalties in an electricity market," *Energy Convers. Manag.*, vol. 76, pp. 1150–1157, 2013, doi: 10.1016/j.enconman.2013.09.014.

[71] B. W. Zhang, Y. Lei, B. F. Bai, and T. S. Zhao, "A two-dimensional model for the design of flow fields in vanadium redox flow batteries," *Int. J. Heat Mass Transf.*, vol. 135, pp. 460–469, 2019, doi: 10.1016/j.ijheatmasstransfer.2019.02.008.

[72] B. Xiong, J. Zhao, K. J. Tseng, M. Skyllas-Kazacos, T. M. Lim, and Y. Zhang, "Thermal hydraulic behavior and efficiency analysis of an all-vanadium redox flow battery," *J. Power Sources*, vol. 242, pp. 314–324, 2013, doi: 10.1016/j.jpowsour.2013.05.092.

[73] A. Bhattacharjee, A. Roy, N. Banerjee, S. Patra, and H. Saha, "Precision dynamic equivalent circuit model of a Vanadium Redox Flow Battery and determination of circuit parameters for its optimal performance in renewable energy applications," *J. Power Sources*, vol. 396, no. June, pp. 506–518, 2018, doi: 10.1016/j.jpowsour.2018.06.017.

[74] F. Baccino, M. Marinelli, P. Nørgård, and F. Silvestro, "Experimental testing procedures and dynamic model validation for vanadium redox flow battery storage system," *J. Power Sources*, vol. 254, pp. 277–286, 2014, doi: 10.1016/j.jpowsour.2013.12.078.

[75] B. Xiong *et al.*, "An Enhanced Equivalent Circuit Model of Vanadium Redox Flow Battery Energy Storage Systems Considering Thermal Effects," *IEEE Access*, vol. 7, pp.

162297–162308, 2019, doi: 10.1109/ACCESS.2019.2952212.

[76] C. Minke and T. Turek, “Materials, system designs and modelling approaches in techno-economic assessment of all-vanadium redox flow batteries – A review,” *J. Power Sources*, vol. 376, no. August 2017, pp. 66–81, 2018, doi: 10.1016/j.jpowsour.2017.11.058.

[77] J. Sheng, A. Mukhopadhyay, W. Wang, and H. Zhu, “Recent advances in the selective membrane for aqueous redox flow batteries,” *Mater. Today Nano*, vol. 7, p. 100044, 2019, doi: 10.1016/j.mtnano.2019.100044.

[78] Q. Wu, X. Zhang, Y. Lv, L. Lin, Y. Liu, and X. Zhou, “Bio-inspired multiscale-pore-network structured carbon felt with enhanced mass transfer and activity for vanadium redox flow batteries,” *J. Mater. Chem. A*, vol. 6, no. 41, pp. 20347–20355, Oct. 2018, doi: 10.1039/c8ta06445h.

[79] J. D. Milshtein, K. M. Tenny, J. L. Barton, J. Drake, R. M. Darling, and F. R. Brushett, “Quantifying Mass Transfer Rates in Redox Flow Batteries,” *J. Electrochem. Soc.*, vol. 164, no. 11, pp. E3265–E3275, 2017, doi: 10.1149/2.0201711jes.

[80] N. M. Delgado, R. Monteiro, M. Abdollahzadeh, P. Ribeirinha, A. Bentien, and A. Mendes, “2D-dynamic phenomenological modelling of vanadium redox flow batteries – Analysis of the mass transport related overpotentials,” *J. Power Sources*, vol. 480, p. 229142, Dec. 2020, doi: 10.1016/J.JPOWSOUR.2020.229142.

[81] N. Ra, A. Dutta, and A. Bhattacharjee, “Optimizing vanadium redox flow battery system power loss using particle swarm optimization technique under different operating conditions,” *Int. J. Energy Res.*, vol. 46, no. 12, pp. 17346–17361, Jul. 2022, doi: 10.1002/ER.8402.

[82] R. Xiong, B. Xiong, Q. Zhang, S. Shi, Y. Su, and D. Zhang, “Capacity Fading Model of Vanadium Redox Flow Battery Considering Water Molecules Migration,” *Int. J. Green Energy*, vol. 19, no. 15, pp. 1613–1622, 2022, doi: 10.1080/15435075.2021.2015599.

[83] M. Jafari, A. Sakti, and A. Botterud, “Optimization of Electrolyte Rebalancing in Vanadium Redox Flow Batteries,” *IEEE Trans. Energy Convers.*, vol. 37, no. 1, pp. 748–751, 2022, doi: 10.1109/TEC.2021.3136769.

[84] D. Kyu Kim, E. Jung Choi, H. Ho Song, and M. Soo Kim, "Experimental and numerical study on the water transport behavior through Nafion® 117 for polymer electrolyte membrane fuel cell," *J. Memb. Sci.*, vol. 497, pp. 194–208, 2016, doi: 10.1016/j.memsci.2015.09.053.

[85] A. Bhattarai *et al.*, "Novel approaches for solving the capacity fade problem during operation of a vanadium redox flow battery," *Batteries*, vol. 4, no. 4, pp. 1–9, 2018, doi: 10.3390/batteries4040048.

[86] B. Khaki and P. Das, "Voltage loss and capacity fade reduction in vanadium redox battery by electrolyte flow control," *Electrochim. Acta*, vol. 405, Feb. 2022, doi: 10.1016/j.electacta.2022.139842.

[87] N. Ra and A. Bhattacharjee, "An Extensive Study and Analysis of System Modeling and Interfacing of Vanadium Redox Flow Battery," *Energy Technol.*, vol. 9, no. 1, p. 2000708, Jan. 2021, doi: 10.1002/ENTE.202000708.

[88] M. Gencten and Y. Sahin, "A critical review on progress of the electrode materials of vanadium redox flow battery," *Int. J. Energy Res.*, vol. 44, no. 10, pp. 7903–7923, 2020, doi: 10.1002/er.5487.

[89] J. Hu, H. He, Z. Wei, and Y. Li, "Disturbance-Immune and Aging-Robust Internal Short Circuit Diagnostic for Lithium-Ion Battery," *IEEE Trans. Ind. Electron.*, vol. 0046, no. c, 2021, doi: 10.1109/TIE.2021.3063968.

[90] J. Hu, X. Bian, Z. Wei, J. Li, and H. He, "Residual Statistics-Based Current Sensor Fault Diagnosis for Smart Battery Management," *IEEE J. Emerg. Sel. Top. Power Electron.*, vol. 10, no. 2, pp. 2435–2444, 2021, doi: 10.1109/JESTPE.2021.3131696.

[91] Z. Wei, J. Zhao, H. He, G. Ding, H. Cui, and L. Liu, "Future smart battery and management: Advanced sensing from external to embedded multi-dimensional measurement," *J. Power Sources*, vol. 489, p. 229462, Mar. 2021, doi: 10.1016/J.JPOWSOUR.2021.229462.

[92] N. Roznyatovskaya, J. Noack, K. Pinkwart, and J. Tübke, "Aspects of electron transfer processes in vanadium redox-flow batteries," *Curr. Opin. Electrochem.*, vol. 19, no. Ii, pp. 42–48, 2020, doi: 10.1016/j.coelec.2019.10.003.

[93] A. Kumar, A. R. Singh, Y. Deng, X. He, P. Kumar, and R. C. Bansal, "Integrated assessment of a sustainable microgrid for a remote village in hilly region," *Energy Convers. Manag.*, vol. 180, no. May 2018, pp. 442–472, 2019, doi: 10.1016/j.enconman.2018.10.084.

[94] T. Sarkar, A. Bhattacharjee, H. Samanta, K. Bhattacharya, and H. Saha, "Optimal design and implementation of solar PV-wind-biogas-VRFB storage integrated smart hybrid microgrid for ensuring zero loss of power supply probability," *Energy Convers. Manag.*, vol. 191, no. April, pp. 102–118, 2019, doi: 10.1016/j.enconman.2019.04.025.

[95] L. Barelli, G. Bidini, P. A. Ottaviano, and D. Pelosi, "Vanadium redox flow batteries application to electric buses propulsion: Performance analysis of hybrid energy storage system," *J. Energy Storage*, vol. 24, no. May, p. 100770, 2019, doi: 10.1016/j.est.2019.100770.

[96] Z. Huang and A. Mu, "Numerical research on a novel flow field design for vanadium redox flow batteries in microgrid," *Int. J. Energy Res.*, vol. 45, no. 10, pp. 14579–14591, 2021, doi: 10.1002/er.6710.

[97] N. Ra and A. Bhattacharjee, "Optimized Electrical Interface for a Vanadium Redox Flow Battery (VRFB) Storage System," *Microelectron. Signal Process.*, pp. 29–48, 2021, doi: 10.1201/9781003168225-3.

[98] M. Pugach, S. Parsegov, E. Gryazina, and A. Bischi, "Output feedback control of electrolyte flow rate for Vanadium Redox Flow Batteries," *J. Power Sources*, vol. 455, Apr. 2020, doi: 10.1016/j.jpowsour.2020.227916.

[99] M. Lu, W. Yang, Y. Deng, and Q. Xu, "An optimal electrolyte addition strategy for improving performance of a vanadium redox flow battery," *Int. J. Energy Res.*, vol. 44, no. 4, pp. 2604–2616, 2020, doi: 10.1002/er.4988.

[100] A. Tang, J. Bao, and M. Skyllas-Kazacos, "Studies on pressure losses and flow rate optimization in vanadium redox flow battery," *J. Power Sources*, vol. 248, pp. 154–162, 2014, doi: 10.1016/j.jpowsour.2013.09.071.

[101] J. Bao, V. Murugesan, C. J. Kamp, Y. Shao, L. Yan, and W. Wang, "Machine Learning Coupled Multi-Scale Modeling for Redox Flow Batteries," *Adv. Theory Simulations*, vol. 3, no. 2, pp. 1–13, 2020, doi: 10.1002/adts.201900167.

[102] D. Roman, S. Saxena, V. Robu, M. Pecht, and D. Flynn, “Machine learning pipeline for battery state-of-health estimation,” *Nat. Mach. Intell.*, vol. 3, no. 5, pp. 447–456, 2021, doi: 10.1038/s42256-021-00312-3.

[103] Z. Fei, F. Yang, K. L. Tsui, L. Li, and Z. Zhang, “Early prediction of battery lifetime via a machine learning based framework,” *Energy*, vol. 225, p. 120205, 2021, doi: 10.1016/j.energy.2021.120205.

[104] M.-F. Ng, J. Zhao, Q. Yan, G. J. Conduit, and Z. W. Seh, “Predicting the state of charge and health of batteries using data-driven machine learning,” *Nat. Mach. Intell.*, vol. 2, no. 3, pp. 161–170, 2020, doi: 10.1038/s42256-020-0156-7.

[105] A. Dineva, B. Csomós, S. Kocsis Sz., and I. Vajda, “Investigation of the performance of direct forecasting strategy using machine learning in State-of-Charge prediction of Li-ion batteries exposed to dynamic loads,” *J. Energy Storage*, vol. 36, p. 102351, 2021, doi: 10.1016/j.est.2021.102351.

[106] Z. Xu, J. Wang, Q. Fan, P. D. Lund, and J. Hong, “Improving the state of charge estimation of reused lithium-ion batteries by abating hysteresis using machine learning technique,” *J. Energy Storage*, vol. 32, no. 2, p. 101678, 2020, doi: 10.1016/j.est.2020.101678.

[107] J. K. Thomas, H. R. Crasta, K. Kausthubha, C. Gowda, and A. Rao, “Battery monitoring system using machine learning,” *J. Energy Storage*, vol. 40, no. December 2020, p. 102741, 2021, doi: 10.1016/j.est.2021.102741.

[108] A. Hossein, S. Dehaghani, R. Soleimani, and A. H. Mohammadi, “Screening of important parameters in optimal design of compressed air energy storage system using an ensemble learning method,” *J. Energy Storage*, vol. 48, p. 104023, 2022, doi: 10.1016/j.est.2022.104023.

[109] N. K. Kandasamy, R. Badrinarayanan, V. R. K. Kanamarlapudi, K. J. Tseng, and B. H. Soong, “Performance analysis of machine-learning approaches for modeling the charging/discharging profiles of stationary battery systems with non-uniform cell aging,” *Batteries*, vol. 3, no. 2, pp. 1–15, 2017, doi: 10.3390/batteries3020018.

[110] H. F. Shen, X. J. Zhu, M. Shao, and H. F. Cao, “Neural network predictive control for vanadium redox flow battery,” *J. Appl. Math.*, vol. 2013, 2013, doi:

10.1155/2013/538237.

[111] M. Fernández-Delgado, M. S. Sirsat, E. Cernadas, S. Alawadi, S. Barro, and M. Febrero-Bande, “An extensive experimental survey of regression methods,” *Neural Networks*, vol. 111, pp. 11–34, 2019, doi: 10.1016/j.neunet.2018.12.010.

[112] C. C. Chang and C. J. Lin, “LIBSVM: A Library for support vector machines,” *ACM Trans. Intell. Syst. Technol.*, vol. 2, no. 3, 2011, doi: 10.1145/1961189.1961199.

[113] R. E. Schapire, “Explaining adaboost,” *Empir. Inference Festschrift Honor Vladimir N. Vapnik*, pp. 37–52, 2013, doi: 10.1007/978-3-642-41136-6_5.

[114] F. Pedregosa FABIANPEDREGOSA *et al.*, “Scikit-learn: Machine Learning in Python Gaël Varoquaux Bertrand Thirion Vincent Dubourg Alexandre Passos PEDREGOSA, VAROQUAUX, GRAMFORT ET AL. Matthieu Perrot,” *J. Mach. Learn. Res.*, vol. 12, pp. 2825–2830, 2011, Accessed: Apr. 19, 2022. [Online]. Available: http://scikit-learn.sourceforge.net.

[115] M. A. Zöller and M. F. Huber, “Benchmark and Survey of Automated Machine Learning Frameworks,” *J. Artif. Intell. Res.*, vol. 70, pp. 409–472, 2021, doi: 10.1613/JAIR.1.11854.

[116] D. M. Belete and M. D. Huchaiah, “Grid search in hyperparameter optimization of machine learning models for prediction of HIV/AIDS test results,” *Int. J. Comput. Appl.*, no. September, 2021, doi: 10.1080/1206212X.2021.1974663.

[117] P. Probst and B. Bischl, “Tunability: Importance of Hyperparameters of Machine Learning Algorithms,” *J. Mach. Learn. Res.*, vol. 20, pp. 1–32, 2019, Accessed: Apr. 19, 2022. [Online]. Available: http://jmlr.org/papers/v20/18-444.html.

[118] “Global Roadmap for Accelerated SDG7 Action in Support of the 2030 Agenda for Sustainable Development and the Paris Agreement on Climate Change,” *High-Level Dialogue on Energy*, vol. New York, 2021, Accessed: Mar. 29, 2022. [Online]. Available: https://www.un.org/en/conferences/energy2021/RESOURCES

[119] K. Lourenssen, J. Williams, F. Ahmadpour, R. Clemmer, and S. Tasnim, “Vanadium redox flow batteries: A comprehensive review,” *J. Energy Storage*, vol. 25, no. July, 2019, doi: 10.1016/j.est.2019.100844.

[120] S. Jung, B. Choi, S. Park, D. W. Lee, Y. B. Kim, and S. Kim, "Computational study of effects of contact resistance on a large-scale vanadium redox flow battery stack," *Int. J. Energy Res.*, vol. 43, no. 6, pp. 2343–2360, 2019, doi: 10.1002/er.4453.

[121] D. Jeong and S. Jung, "Numerical analysis of cycling performance of vanadium redox flow battery," *Int. J. Energy Res.*, vol. 44, no. 7, pp. 5209–5222, 2020, doi: 10.1002/er.5261.

[122] N. Ra and A. Bhattacharjee, "An Extensive Study and Analysis of System Modeling and Interfacing of Vanadium Redox Flow Battery," *Energy Technol.*, vol. 9, no. 1, 2021, doi: 10.1002/ente.202000708.

[123] T. Zou, X. Shi, and L. Yu, "Study on energy loss of 35 kW all vanadium redox flow battery energy storage system under closed-loop flow strategy," *J. Power Sources*, vol. 490, p. 229514, Apr. 2021, doi: 10.1016/j.jpowsour.2021.229514.

[124] H. Samanta, A. Bhattacharjee, M. Pramanik, A. Das, K. Das Bhattacharya, and H. Saha, "Internet of things based smart energy management in a vanadium redox flow battery storage integrated bio-solar microgrid," *J. Energy Storage*, vol. 32, Dec. 2020, doi: 10.1016/j.est.2020.101967.

[125] A. Bhattacharjee, H. Samanta, A. Ghosh, T. K. Mallick, S. Sengupta, and H. Saha, "Optimized Integration of Hybrid Renewable Sources with Long-Life Battery Energy Storage in Microgrids for Peak Power Shaving and Demand Side Management under Different Tariff Scenario," *Energy Technol.*, vol. 9, no. 9, pp. 1–10, 2021, doi: 10.1002/ente.202100199.

[126] J. Li *et al.*, "Optimal control strategy for large-scale VRB energy storage auxiliary power system in peak shaving," *Int. J. Electr. Power Energy Syst.*, vol. 120, p. 106007, Sep. 2020, doi: 10.1016/J.IJEPES.2020.106007.

[127] A. Lucas and S. Chondrogiannis, "Smart grid energy storage controller for frequency regulation and peak shaving, using a vanadium redox flow battery," *Int. J. Electr. Power Energy Syst.*, vol. 80, pp. 26–36, 2016, doi: 10.1016/j.ijepes.2016.01.025.

[128] J. M. Lujano-Rojas, G. Zubi, R. Dufo-López, J. L. Bernal-Agustín, and J. P. S. Catalão, "Novel probabilistic optimization model for lead-acid and vanadium redox flow batteries under real-time pricing programs," *Int. J. Electr. Power Energy Syst.*, vol. 97,

pp. 72–84, Apr. 2018, doi: 10.1016/J.IJEPES.2017.10.037.

[129] T. Kerdphol, K. Fuji, Y. Mitani, M. Watanabe, and Y. Qudaih, “Optimization of a battery energy storage system using particle swarm optimization for stand-alone microgrids,” *Int. J. Electr. Power Energy Syst.*, vol. 81, pp. 32–39, Oct. 2016, doi: 10.1016/J.IJEPES.2016.02.006.

[130] T. Kerdphol, Y. Qudaih, and Y. Mitani, “Optimum battery energy storage system using PSO considering dynamic demand response for microgrids,” *Int. J. Electr. Power Energy Syst.*, vol. 83, pp. 58–66, 2016, doi: 10.1016/j.ijepes.2016.03.064.

[131] S. J. Yoon, S. Kim, and D. K. Kim, “Optimization of local porosity in the electrode as an advanced channel for all-vanadium redox flow battery,” *Energy*, vol. 172, pp. 26–35, Apr. 2019, doi: 10.1016/J.ENERGY.2019.01.101.

[132] F. Chen, H. Gao, H. Chen, and C. Yan, “Evaluation of thermal behaviors for the multi-stack vanadium flow battery module,” *J. Energy Storage*, vol. 27, no. November 2019, p. 101081, 2020, doi: 10.1016/j.est.2019.101081.

[133] R. Badrinarayanan, K. J. Tseng, B. H. Soong, and Z. Wei, “Modelling and control of vanadium redox flow battery for profile based charging applications,” *Energy*, vol. 141, pp. 1479–1488, 2017, doi: 10.1016/j.energy.2017.11.082.

[134] Y. Yan, M. Skyllas-Kazacos, and J. Bao, “Effects of battery design, environmental temperature and electrolyte flowrate on thermal behaviour of a vanadium redox flow battery in different applications,” *J. Energy Storage*, vol. 11, pp. 104–118, 2017, doi: 10.1016/j.est.2017.01.007.

[135] A. Bhattacharjee and H. Saha, “Development of an efficient thermal management system for Vanadium Redox Flow Battery under different charge-discharge conditions,” *Appl. Energy*, vol. 230, no. August, pp. 1182–1192, 2018, doi: 10.1016/j.apenergy.2018.09.056.

[136] X. Ma, H. Zhang, C. Sun, Y. Zou, and T. Zhang, “An optimal strategy of electrolyte flow rate for vanadium redox flow battery,” *J. Power Sources*, vol. 203, pp. 153–158, 2012, doi: 10.1016/j.jpowsour.2011.11.036.

[137] D. K. Kim, S. J. Yoon, J. Lee, and S. Kim, “Parametric study and flow rate optimization

of all-vanadium redox flow batteries," *Appl. Energy*, vol. 228, no. July, pp. 891–901, 2018, doi: 10.1016/j.apenergy.2018.06.094.

[138] S. König, M. R. Suriyah, and T. Leibfried, "Volumetric electrolyte flow rate control in vanadium redox flow batteries using a variable flow factor," *2015 6th Int. Renew. Energy Congr. IREC 2015*, 2015, doi: 10.1109/IREC.2015.7110861.

[139] V. K. Yu and D. Chen, "Peak power prediction of a vanadium redox flow battery," *J. Power Sources*, vol. 268, pp. 261–268, Dec. 2014, doi: 10.1016/j.jpowsour.2014.06.053.

[140] M. Guarnieri, A. Trovò, and F. Picano, "Enhancing the efficiency of kW-class vanadium redox flow batteries by flow factor modulation: An experimental method," *Appl. Energy*, vol. 262, no. January, 2020, doi: 10.1016/j.apenergy.2020.114532.

[141] R. Gundlapalli and S. Jayanti, "Effect of channel dimensions of serpentine flow fields on the performance of a vanadium redox flow battery," *J. Energy Storage*, vol. 23, no. November 2018, pp. 148–158, 2019, doi: 10.1016/j.est.2019.03.014.

[142] T. Jirabovornwisut, S. Kheawhom, Y. S. Chen, and A. Arpornwichanop, "Optimal operational strategy for a vanadium redox flow battery," *Comput. Chem. Eng.*, vol. 136, p. 106805, 2020, doi: 10.1016/j.compchemeng.2020.106805.

[143] R. C. Eberhart and Y. Shi, "Particle swarm optimization: Developments, applications and resources," *Proc. IEEE Conf. Evol. Comput. ICEC*, vol. 1, no. February, pp. 81–86, 2001, doi: 10.1109/cec.2001.934374.

[144] M. P. Song and G. C. Gu, "Research on particle swarm optimization: A review," *Proc. 2004 Int. Conf. Mach. Learn. Cybern.*, vol. 4, no. August, pp. 2236–2241, 2004, doi: 10.1109/icmlc.2004.1382171.

[145] Y. Zhang, S. Wang, and G. Ji, "A Comprehensive Survey on Particle Swarm Optimization Algorithm and Its Applications," *Math. Probl. Eng.*, vol. 2015, 2015, doi: 10.1155/2015/931256.

[146] J. Kennedy and R. Eberhart, "Particle swarm optimization," *Proc. ICNN'95 - Int. Conf. Neural Networks*, vol. 4, pp. 1942–1948, 1995, doi: 10.1109/ICNN.1995.488968.

[147] B. Xiong, Z. Wang, Y. Li, K. Qin, J. Chen, and J. Mu, "An Optimal Operational Strategy for Vanadium Redox Flow Battery Based on Particle Swarm Optimization," *2019 IEEE*

PES Innov. Smart Grid Technol. Asia, ISGT 2019, pp. 2639–2643, 2019, doi: 10.1109/ISGT-Asia.2019.8881378.

[148] B. Wang, D. Xuan, X. Zhao, J. Chen, and C. Lu, "Dynamic battery equalization scheme of multi-cell lithium-ion battery pack based on PSO and VUFLC," *Int. J. Electr. Power Energy Syst.*, vol. 136, Mar. 2022, doi: 10.1016/j.ijepes.2021.107760.

[149] M. Razghandi, A. Dehghan, and R. Yousefzadeh, "Application of particle swarm optimization and genetic algorithm for optimization of a southern Iranian oilfield," *J. Pet. Explor. Prod.*, vol. 11, no. 4, pp. 1781–1796, 2021, doi: 10.1007/s13202-021-01120-6.

[150] N. Jatana and B. Suri, "Particle Swarm and Genetic Algorithm applied to mutation testing for test data generation : A comparative evaluation," *J. King Saud Univ. - Comput. Inf. Sci.*, vol. 32, no. 4, pp. 514–521, 2020, doi: 10.1016/j.jksuci.2019.05.004.

[151] N. Rikatsih, M. Anshori, W. F. Mahmudy, and Syafrial, "Performance Comparison of Genetic Algorithm and Particle Swarm Optimization in Solving Product Storage Optimization," in *Proceedings of 2019 4th International Conference on Sustainable Information Engineering and Technology, SIET 2019*, 2019, pp. 16–21. doi: 10.1109/SIET48054.2019.8986089.

[152] C. A. Souza *et al.*, "Annals of Nuclear Energy Comparison of computational performance of GA and PSO optimization techniques when designing similar systems – Typical PWR core case," *Ann. Nucl. Energy*, vol. 38, no. 6, pp. 1339–1346, 2011, doi: 10.1016/j.anucene.2011.02.002.

[153] W. F. Lamb *et al.*, "A review of trends and drivers of greenhouse gas emissions by sector from 1990 to 2018," *Environ. Res. Lett.*, vol. 16, no. 7, p. 073005, Jun. 2021, doi: 10.1088/1748-9326/ABEE4E.

[154] J. L. Aguilar-Santana, H. Jarimi, M. Velasco-Carrasco, and S. Riffat, "Review on window-glazing technologies and future prospects," *International Journal of Low-Carbon Technologies*, vol. 15, no. 1. pp. 112–120, 2019. doi: 10.1093/ijlct/ctz032.

[155] F. Favoino, F. Fiorito, A. Cannavale, G. Ranzi, and M. Overend, "Optimal control and performance of photovoltachromic switchable glazing for building integration in temperate climates," *Appl. Energy*, vol. 178, pp. 943–961, Sep. 2016, doi:

10.1016/J.APENERGY.2016.06.107.

[156] R. Singh, I. J. Lazarus, and V. V. N. Kishore, “Uncertainty and sensitivity analyses of energy and visual performances of office building with external venetian blind shading in hot-dry climate,” *Appl. Energy*, vol. 184, pp. 155–170, Dec. 2016, doi: 10.1016/J.APENERGY.2016.10.007.

[157] D. Bastien and A. K. Athienitis, “Methodology for selecting fenestration systems in heating dominated climates,” *Appl. Energy*, vol. 154, pp. 1004–1019, Sep. 2015, doi: 10.1016/J.APENERGY.2015.05.083.

[158] A. Ghosh, S. Sundaram, and T. K. Mallick, “Investigation of thermal and electrical performances of a combined semi-transparent PV-vacuum glazing,” *Appl. Energy*, vol. 228, no. April, pp. 1591–1600, 2018, doi: 10.1016/j.apenergy.2018.07.040.

[159] A. Ghosh and B. Norton, “Advances in switchable and highly insulating autonomous (self-powered) glazing systems for adaptive low energy buildings,” *Renew. Energy*, vol. 126, pp. 1003–1031, Oct. 2018, doi: 10.1016/J.RENENE.2018.04.038.

[160] S. Nundy, A. Mesloub, B. M. Alsolami, and A. Ghosh, “Electrically actuated visible and near-infrared regulating switchable smart window for energy positive building: A review,” *J. Clean. Prod.*, vol. 301, p. 126854, 2021, doi: 10.1016/j.jclepro.2021.126854.

[161] A. Ebrahimpour and M. Maerefat, “Application of advanced glazing and overhangs in residential buildings,” *Energy Convers. Manag.*, vol. 52, no. 1, pp. 212–219, 2011, doi: 10.1016/J.ENCONMAN.2010.06.061.

[162] A. Stegou-Sagia, K. Antonopoulos, C. Angelopoulou, and G. Kotsiovelos, “The impact of glazing on energy consumption and comfort,” *Energy Convers. Manag.*, vol. 48, no. 11, pp. 2844–2852, Nov. 2007, doi: 10.1016/J.ENCONMAN.2007.07.005.

[163] C. Buratti and E. Moretti, “Glazing systems with silica aerogel for energy savings in buildings,” *Appl. Energy*, vol. 98, pp. 396–403, Oct. 2012, doi: 10.1016/J.APENERGY.2012.03.062.

[164] A. Ghosh, “Potential of building integrated and attached/applied photovoltaic (BIPV/BAPV) for adaptive less energy-hungry building’s skin: A comprehensive review,” *J. Clean. Prod.*, vol. 276, p. 123343, 2020, doi: 10.1016/j.jclepro.2020.123343.

[165] G. Rajendran, C. A. Vaithilingam, N. Misron, K. Naidu, and M. R. Ahmed, “A comprehensive review on system architecture and international standards for electric vehicle charging stations,” *J. Energy Storage*, vol. 42, p. 103099, Oct. 2021, doi: 10.1016/J.EST.2021.103099.

[166] R. P. Narasipuram and S. Mopidevi, “A technological overview & design considerations for developing electric vehicle charging stations,” *J. Energy Storage*, vol. 43, p. 103225, Nov. 2021, doi: 10.1016/J.EST.2021.103225.

[167] M. Pugach, V. Vyshinsky, and A. Bischi, “Energy efficiency analysis for a kilo-watt class vanadium redox flow battery system,” *Appl. Energy*, vol. 253, Nov. 2019, doi: 10.1016/j.apenergy.2019.113533.

[168] M. Arbabzadeh, J. X. Johnson, R. De Kleine, and G. A. Keoleian, “Vanadium redox flow batteries to reach greenhouse gas emissions targets in an off-grid configuration,” *Appl. Energy*, vol. 146, pp. 397–408, 2015, doi: 10.1016/j.apenergy.2015.02.005.

[169] A. Trovò and M. Guarnieri, “Standby thermal management system for a kW-class vanadium redox flow battery,” *Energy Convers. Manag.*, vol. 226, Dec. 2020, doi: 10.1016/J.ENCONMAN.2020.113510.

[170] J. W. Ni, M. J. Li, T. Ma, W. Wei, and Z. Li, “The configuration optimized design method based on real-time efficiency for the application of vanadium redox flow battery in microgrid,” *Energy Convers. Manag.*, vol. 267, no. June, p. 115899, Sep. 2022, doi: 10.1016/J.ENCONMAN.2022.115899.

[171] G. Hu *et al.*, “A gradient bi-functional graphene-based modified electrode for vanadium redox flow batteries,” *Energy Storage Mater.*, vol. 13, pp. 66–71, 2018, doi: 10.1016/j.ensm.2017.12.026.

[172] C. Zhang, T. S. Zhao, Q. Xu, L. An, and G. Zhao, “Effects of operating temperature on the performance of vanadium redox flow batteries,” *Appl. Energy*, vol. 155, pp. 349–353, Oct. 2015, doi: 10.1016/J.APENERGY.2015.06.002.

[173] A. Trovò *et al.*, “Standby thermal model of a vanadium redox flow battery stack with crossover and shunt-current effects,” *Appl. Energy*, vol. 240, no. April, pp. 893–906, 2019, doi: 10.1016/j.apenergy.2019.02.067.

[174] Y. Liu, L. Yu, L. Liu, and J. Xi, “Tailoring the vanadium/proton ratio of electrolytes to boost efficiency and stability of vanadium flow batteries over a wide temperature range,” *Appl. Energy*, vol. 301, p. 117454, Nov. 2021, doi: 10.1016/J.APENERGY.2021.117454.

[175] Z. Wei, J. Zhao, and B. Xiong, “Dynamic electro-thermal modeling of all-vanadium redox flow battery with forced cooling strategies,” *Appl. Energy*, vol. 135, pp. 1–10, Dec. 2014, doi: 10.1016/J.APENERGY.2014.08.062.

[176] X. Zhang, Y. Li, M. Skyllas-Kazacos, and J. Bao, “Optimal Sizing of Vanadium Redox Flow Battery Systems for Residential Applications Based on Battery Electrochemical Characteristics,” *Energies 2016, Vol. 9, Page 857*, vol. 9, no. 10, p. 857, Oct. 2016, doi: 10.3390/EN9100857.

[177] M. Mondal, | Kamal, K. Mandal, and A. Datta, “Solar PV driven hybrid gravity power module—Vanadium redox flow battery energy storage for an energy efficient multi-storied building,” *Int. J. Energy Res.*, Aug. 2022, doi: 10.1002/ER.8460.

[178] N. Hanus, A. Newkirk, and H. Stratton, “Organizational and psychological measures for data center energy efficiency: barriers and mitigation strategies,” *Energy Effic.*, vol. 16, no. 1, pp. 1–18, 2023, doi: 10.1007/s12053-022-10078-1.

[179] V. Földváry Ličina *et al.*, “Development of the ASHRAE Global Thermal Comfort Database II,” *Build. Environ.*, vol. 142, no. June, pp. 502–512, 2018, doi: 10.1016/j.buildenv.2018.06.022.

[180] F. D. Moya, J. L. Torres-Moreno, and J. D. Álvarez, “Optimal model for energy management strategy in smart building with energy storage systems and electric vehicles,” *Energies*, vol. 13, no. 14, 2020, doi: 10.3390/en13143605.

[181] D. Mazzeo, “Solar and wind assisted heat pump to meet the building air conditioning and electric energy demand in the presence of an electric vehicle charging station and battery storage,” *J. Clean. Prod.*, vol. 213, pp. 1228–1250, 2019, doi: 10.1016/j.jclepro.2018.12.212.

[182] G. Bianco, F. Delfino, G. Ferro, M. Robba, and M. Rossi, “A hierarchical Building Management System for temperature’s optimal control and electric vehicles’ integration,” *Energy Convers. Manag. X*, vol. 17, no. June 2022, p. 100339, 2023, doi:

10.1016/j.ecmx.2022.100339.

[183] A. Ghosh, B. Norton, and A. Duffy, “Measured thermal & daylight performance of an evacuated glazing using an outdoor test cell,” *Appl. Energy*, vol. 177, pp. 196–203, Sep. 2016, doi: 10.1016/J.APENERGY.2016.05.118.

[184] A. Ghosh, B. Norton, and A. Duffy, “Measured overall heat transfer coefficient of a suspended particle device switchable glazing,” *Appl. Energy*, vol. 159, pp. 362–369, Dec. 2015, doi: 10.1016/J.APENERGY.2015.09.019.

[185] X. Liu and Y. Wu, “Experimental characterisation of a smart glazing with tuneable transparency, light scattering ability and electricity generation function,” *Appl. Energy*, vol. 303, p. 117521, Dec. 2021, doi: 10.1016/J.APENERGY.2021.117521.

[186] M. Krarti, “Design optimization of smart glazing optical properties for office spaces,” *Appl. Energy*, vol. 308, p. 118411, Feb. 2022, doi: 10.1016/J.APENERGY.2021.118411.

[187] Y. Tao, X. Fang, H. Zhang, G. Zhang, J. Tu, and L. Shi, “Impacts of thermo-optical properties on the seasonal operation of thermochromic smart window,” *Energy Convers. Manag.*, vol. 252, Jan. 2022, doi: 10.1016/J.ENCONMAN.2021.115058.

[188] A. Ghosh and B. Norton, “Optimization of PV powered SPD switchable glazing to minimise probability of loss of power supply,” *Renew. Energy*, vol. 131, pp. 993–1001, 2019, doi: 10.1016/j.renene.2018.07.115.

[189] G. Habash, D. Chapotchkine, P. Fisher, A. Rancourt, R. Habash, and W. Norris, “Sustainable Design of a Nearly Zero Energy Building Facilitated by a Smart Microgrid,” *J. Renew. Energy*, vol. 2014, pp. 1–11, 2014, doi: 10.1155/2014/725850.

[190] M. Sechilariu, B. Wang, and F. Locment, “Building integrated photovoltaic system with energy storage and smart grid communication,” *IEEE Trans. Ind. Electron.*, vol. 60, no. 4, pp. 1607–1618, 2013, doi: 10.1109/TIE.2012.2222852.

[191] M. Sechilariu, B. Wang, and F. Locment, “Building-integrated microgrid: Advanced local energy management for forthcoming smart power grid communication,” *Energy Build.*, vol. 59, pp. 236–243, 2013, doi: 10.1016/J.ENBUILD.2012.12.039.

[192] M. Sechilariu, F. Locment, and B. Wang, “Photovoltaic electricity for sustainable

building. Efficiency and energy cost reduction for isolated DC microgrid," *Energies*, vol. 8, no. 8, pp. 7945–7967, 2015, doi: 10.3390/en8087945.

List of Publications

International Journals:

1) **Nawin Ra**, Ankur Bhattacharjee*, "An Extensive Study and analysis of System Modeling and Interfacing of Vanadium Redox Flow Battery", *Energy Technology, Wiley, Vol 9, Issue 1, Jan.* 2021. doi:10.1002/ente.202000708 (**SCI, IF: 4.149**).
2) **Nawin Ra**, Ankur Bhattacharjee*, "Prediction of vanadium redox flow battery storage system power loss under different operating conditions: Machine learning based approach", *International Journal of Energy Research, Wiley, 2022; 1- 13.* doi:10.1002/er.8757 (**SCI, IF: 4.672**).
3) **Nawin Ra**, Arjun Dutta, Ankur Bhattacharjee*, "Optimizing vanadium redox flow battery system power loss using particle swarm optimization technique under different operating conditions", *International Journal of Energy Research, Wiley, 2022; 46(12): 17346- 17361*. doi: 10.1002/er.8402 (**SCI, IF: 4.672**).
4) **Nawin Ra**, Aritra Ghosh, Ankur Bhattacharjee*, "IoT-based smart energy management for solar – vanadium redox flow battery powered switchable building glazing satisfying the HVAC system of EV charging stations", *Energy Conversion and Management, Elsevier, 2023; 281: 116851* (**SCI, IF: 11.533**).
5) **Nawin Ra**, Ankur Bhattacharjee*, "Modeling and estimation of capacity fade in vanadium redox flow battery", *Journal of Energy Storage, Elsevier* (**SCI**) ***(Under Review)***.

**Corresponding Author*

Book chapters:

1) **Nawin Ra**, Ankur Bhattacharjee, "Optimized Electrical Interface for Vanadium Redox Flow Battery (VRFB) Storage System: Modeling, Development and Implementation", *CRC press, Taylor & Francis Publication, 2020.* doi*:* 10.1201/9781003168225.
2) **Nawin Ra,** Hiranmay Saha, Ankur Bhattacharjee, "Vanadium Redox Flow Batteries: Electrode Materials", *CRC press, Taylor & Francis Publication, 2021* ***(Accepted).***

International Conferences:

1) **Nawin Ra**, Ankur Bhattacharjee, "Optimized Integration of VRFB Storage with Grid-tied Solar PV Power System to mitigate Voltage Instability due to High PV Penetration", in *37th Virtual European Photovoltaic Solar Energy Conference and Exhibition (V-EUPVSEC), Lisbon, 2020.*

2) **Nawin Ra**, Ankur Bhattacharjee, "Vanadium Redox Flow Battery System Power Loss Optimization: Genetic Algorithm based Approach**",** *2nd IEEE International Conference on Power Electronics and Energy (ICPEE 2023), IEEE Bhubaneshwar Subsection, Jan 3-5, 2023,* **Secured IEEE Best Paper award. Eligible for publication in "IEEE transactions on Industry Applications Society".**
3) **Nawin Ra**, Sahil Varman, Joseph Antony, Ankur Bhattacharjee, "Prediction of optical performance of solar PV under the impact of natural dust accumulation: Machine Learning approach", *IEEE IAS Global Conference on Renewable Energy and Hydrogen Technologies (GlobConHT)*, *Mar 11-13, 2023, Maldives National University.* **Eligible for publication in "IEEE transactions on Industry Applications Society".**

Biography of Nawin Ra (Ph.D. Candidate)

Nawin Ra received his B.E (Electrical and Electronics Engineering) degree in 2017 from Anna University, Chennai, India. He received his M. Tech (Green Energy Technology) degree in 2019 from Pondicherry (Central) University, India. He is currently pursuing his Ph.D. degree under the supervision of Dr. Ankur Bhattacharjee at the Department of Electrical and Electronics Engineering, Birla Institute of Technology and Science (BITS)-Pilani, Hyderabad Campus from January 2020. His current research is focused on the optimized integration of Vanadium Redox Flow Batteries with Renewable Energy Sources. He has published 4 reputed International Journals (SCI), 2 Book Chapters, and 3 International Conference papers in the area of Energy Storage and Renewable Energy. He received IEEE Best paper award at 2023 IEEE International Conference on Power Electronics and Energy (ICPEE 2023), conducted by KIIT, Bhubaneswar, IEEE Kolkata section. His research interests include Energy Systems, Flow Batteries, Solar Photovoltaics, Energy Management, Power Electronic Converters, Electric Vehicles, Machine learning, and Optimization.

Biography of Dr. Ankur Bhattacharjee (Supervisor)

Dr. Ankur Bhattacharjee did his Ph.D in Renewable Energy from Indian Institute of Engineering Science and Technology, Shibpur in 2018. Presently he is working as Assistant Professor in the Department of Electrical and Electronics Engineering at BITS-Pilani, Hyderabad Campus, India. He has over 8 years of teaching and research experience in different areas of Electrical Engineering and Renewable Energy. He has published 18 reputed International Journals (SCI), 22 International Conferences, 6 Book chapters and a Book in the area of Renewable Energy. He has filed 3 patents and 1 of them has been granted in March 2023. Dr. Bhattacharjee has 5 ongoing research projects in the field of renewable energy, battery storage and EV charging station, as PI and Co-PI, sponsored by different Indian Govt. (DST, DBT etc.) agencies and Pvt. Industries. He has been recently awarded the DST Young Scientist and Technologist (SYST), in Oct, 2022. His current research areas are Solar PV, Battery Energy Storage Systems, Energy Management, Smart Microgrids, Power Electronic Converters, Machine Learning and Electric Vehicles.